Master's thesis

Angular selective electron detection using microchannel plates for a possible background reduction at the KATRIN experiment

Patrick Oelpmann

August 23, 2021

Institut für Kernphysik
AG Weinheimer
Westfälische Wilhelms-Universität Münster

Referee	Prof. Dr. Christian Weinheimer
second referee	Prof. Dr. Anton Andronic

Declaration of Academic Integrity [1]

I hereby confirm that this thesis on "Angular selective electron detection using microchannel plates for a possible background reduction at the KATRIN experiment" is solely my own work and that I have used no sources or aids other than the ones stated. All passages in my thesis for which other sources, including electronic media, have been used, be it direct quotes or content references, have been acknowledged as such and the sources cited.

23.08.2021 Patrick Oelpmann

(date and signature of student)

I agree to have my thesis checked in order to rule out potential similarities with other works and to have my thesis stored in a database for this purpose

23.08.2021 Patrick Oelpmann

(date and signature of student)

[1] Taken from https://www.uni-muenster.de/imperia/md/content/math_nat_fakultaet/pruefungsamt/pruefungsamt_neu/allgemein/plagiatserkl__rung_englisch.docx.

Contents

1 Introduction

Since the neutrino was predicted by *W. Pauli* in the year 1930 [1] a large scientific community is interested in detecting and describing it. It is not only the most common massive particle in the universe but also the Standard Model particle with the smallest known interaction cross section with matter until now. The neutrino was first predicted because of the continuous energy spectrum of electrons in the beta decay that could only be described by a three body decay. The first discovery of neutrinos was successfully made by *C. Cowan* and *F. Reines* with the Poltergeist experiment in 1956 for which *F. Reines* won the Nobel Price in Physics of the year 1995 [2][3]. This experiment used electron antineutrinos from a nearby nuclear reactor interacting with protons producing neutrons and positrons that are making characteristic signals. Several additional experiments like the Homestake experiment [4] that used solar neutrinos were also able to prove the existence of neutrinos. But one could see that there were not as many electron neutrinos detected for the neutrino experiments done with solar neutrinos as one has calculated for the Sun leading to the solar neutrino problem. Because of charge conservation the neutrino is uncharged and because of spin conservation in the beta decay the neutrino must have spin 1/2. Whether neutrinos are massive particles remained unclear until the measurement of the solar neutrino flux in the Sudbury Neutrino Observatory (SNO) experiment and at the KAMIOKANDE experiment. The solar neutrino flux can be predicted correctly, when the transformation of electron neutrinos to muon and tau neutrinos is considered [5][6][7][8]. This can be mathematically described by neutrino oscillations for which the Nobel prize is given to *T. Kajita* and *A.B. McDonald* in 2015 [9]. Neutrinos can only oscillate between each other when they have non-zero masses and are consisting of neutrino mass eigenstates. Then the oscillation is dependent on the squared mass differences of the mass eigenstates, which implies that at least two of the three known neutrino mass eigenstates are non-zero.

However, the oscillation experiments are not sensitive to the absolute masses but only to the squared mass differences. This circumstance lead to different thoughts about how to measure the absolute mass of the neutrino. There are several approaches:

- The cosmic microwave background and other cosmological measurements give model-dependent upper limits on the sum of the neutrino masses.
- The neutrinoless double beta decay gives the squared coherent sum of the neutrino masses for the case that neutrinos are Majorana particles instead of Dirac particles.

- The most direct and the only model-independent approach is the kinematic analysis of beta decay or electron capture spectra, e.g. of tritium or ^{163}Ho, where the squared sum of the neutrino mass eigenstates is investigated.

All the approaches are model dependent except for the last one. The kinematics of the tritium beta decay is the basis of the model independent direct measurement of the neutrino mass analysis in the **KA**rlsruhe **TRI**tium **N**eutrino experiment (KATRIN) to which this thesis contributes.
The KATRIN experiment is located at the Karlsruher Institute of Technology. It aims to reach a sensitivity of 200 meV after a measurement time of 1000 days [10] and was able to set a new upper limit on the mass of electron neutrinos of $m_{\overline{\nu}_e} < 0.8\,\mathrm{eV}$ (90 % C.L.) [11].
It uses tritium that decays in a weak interaction process to obtain electrons that provide information about the electron antineutrino mass:

$$^{3}\mathrm{H} \rightarrow {}^{3}\mathrm{He}^{+} + e^{-} + \overline{\nu}_e \tag{1}$$

The endpoint and the shape of the endpoint region of the electron energy spectrum directly depends on the neutrino mass. So what is measured with highest priority is this last region shortly below the highest end of the spectrum. Due to a very low amount of electrons having almost all the kinetic energy of the decay an ultra high luminosity is needed as well as an excellent energy resolution and a very low background. The aimed for upper limit of the background rate is 10 mcps but until now this is about a factor of 22 too large and thus limits the sensitivity on the neutrino mass [11].
Many sources of background were already identified and efficiently reduced. The work in this Master thesis concentrates on a method to increase the sensitivity of the KATRIN experiment by further lowering the background. This is done by the utilization of the different angular distributions of the signal electrons and the specific type of the main background electrons in the KATRIN experiment.

2 Neutrinos

In this chapter a brief introduction of neutrinos is given with its history and remarkable properties before describing the KATRIN experiment as this is the first step to understand the motivation of neutrino mass experiments.

2.1 Postulation and experimental prove

After the discovery of the alpha decay with its very distinct decay energy because of its two body decay nature there was also another type of decay observed called the beta decay. Instead of alpha particles there are emitted electrons but with a broad continuous energy range. This continuous spectrum could only be described by a three body decay. Therefore Pauli postulated a new particle in 1930, the neutrino [1], making the reaction possible where a neutron decays into a proton, an electron and an electron antineutrino:

$$n \to p + e^- + \bar{\nu}_e. \tag{2}$$

It was clear that because of charge conservation the neutrino has to be neutral and because of spin conservation the neutrino spin is 1/2 and is therefore a fermion. But what was not known for a long time is whether it had a rest mass and whether it would be possible at all to detect it. It was thought to have a very low cross section because of its neutrality and leptonic character so that the electromagnetic force as well as the strong interaction has no influence on the particle. Conclusively the neutrino is only affected by the negligible gravitational force and the short ranged weak interaction.
The first ones to detect the neutrino were *C. Cowan* and *F. Reines* with the Poltergeist experiment in 1956 for which *F. Reines* won in 1995 the Nobel Prize in Physics [3][2]. They considered the inverse beta decay process when an electron antineutrino interacts with a proton producing a neutron and a positron:

$$\bar{\nu}_e + p \to n + e^+. \tag{3}$$

The positron and the electron form a meta-stable state, the so called positronium. After its collapse both constituents will annihilate and in most cases emit two photons back to back with an energy of 511 keV, which is the rest mass of the electrons and the positron, respectively. Further, the emitted neutron is caught by a nearby atom after being moderated by the surrounding water due to elastic scattering. This process results in an additional time-delayed signal with a characteristic energy. Conclusively,

there needs to be a specific time difference between these two signals when having the same origin being the electron antineutrino reaction with the proton. This time difference is the time taken by the moderation subtracted with the time of the annihilation of the electron with a positron.
The experiment was done with two big tanks of 100 L each being 11 m away from a nuclear reactor which delivered an anti neutrino flux of $5 \cdot 10^{13} \frac{1}{\mathrm{s \cdot cm^2}}$. The tank was filled with water to moderate the neutrons and with ^{113}Cd due to its high absorption ability for thermal neutrons. The detection of the photons emitted by the annihilation and the absorption of the neutrons was done by scintillators in combination with photomultiplier tubes placed around the tank.

This experiment indeed was able to measure this coincident reaction and thereby proved the existence of neutrinos. Furthermore it gave a first value for the cross section of neutrinos with $\sigma = 6.3 \cdot 10^{-44}\,\mathrm{cm}^2$ [3].

Solar neutrino problem Later on in the 1960s a first experiment to measure the flux of solar neutrinos to the earth was performed. This is the famous Homestake experiment [4].
Therefore a mine 1478 m deep under the ground was chosen to minimize cosmic radiation. The detection principle was to use 615 t of tetra-chloroethylene in a big tank where the solar neutrinos can interact with the chlorine producing argon and an electron:

$$\nu_e + {}^{37}\mathrm{Cl} \rightarrow {}^{37}\mathrm{Ar} + \mathrm{e}^-. \tag{4}$$

A substance with chlorine is used because of the low threshold of 0.814 MeV for the interaction process described in the reaction 4.Therefore it is sensitive to solar neutrinos from different fusion processes as visible in figure 2.1. One has to mention that the Homestake experiment is exclusively able to detect electron neutrinos. This is because when the reaction described in 4 would take place with muon or tau neutrinos a muon or a tauon would be produced. Those have much higher masses than the electron ($m_e = 0.511\,\mathrm{MeV}$) with $m_\mu = 106\,\mathrm{MeV}$ and $m_\tau = 1777\,\mathrm{MeV}$ and thus this process is forbidden because of too low neutrino energies from the sun that produces neutrinos of up to 26.73 MeV [12].

However, when comparing the amount of neutrinos detected in the experiment with the expectations by the standard solar model a discrepancy was seen: There was a lack of neutrinos of about 2/3. Additionally more experiments like the GALLEX experiment could verify that this lack of neutrinos is not just a misunderstanding of the data

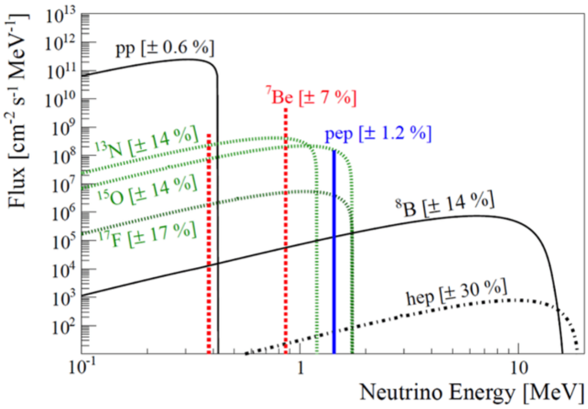

Figure 2.1: Energy spectrum of neutrinos from different solar fusion processes. Taken from [13].

or of the Sun [14].
To explain this behavior oscillation between different flavors of the neutrinos were proposed. A fundamental condition for oscillation is that neutrinos need to have non-zero masses, so this process would be a clear indication for physics beyond the standard model, where neutrinos are supposed to be massless.
To investigate this hypothesis several new experiments were done, like the Sudbury Neutrino Observatory experiment (SNO), which is not only sensitive to electron neutrinos but due to neutral current interaction also sensitive to muon and tau neutrinos. It has a threshold for detection of about 6 MeV, so, for the detection predominantly the weak ^{8}B branch in the p-p chain is used.
The SNO experiment uses a tank filled with heavy water surrounded by photomultiplier tubes. The heavy water tank itself is surrounded by normal water as a shielding for radiation.
The detection of particles in this experiment is based on the Cherenkov radiation. When a charged particle is traveling faster than the speed of light in a medium then it emits Cherenkov radiation which can be used for detection of particles but also for determining the direction of the origin of the incident particle and the type of particles. There are three interaction channels that have to be considered:

- **charged current interaction**
  The electron neutrinos can react with the neutron to a proton and an electron. This again can only happen for electron neutrinos because the muon and tau neutrino have much to high masses and therefore a muon or tauon can not be

generated in this process. The electron gets most of the energy of the neutrino and can be detected as Cherenkov radiation by the photomultiplier tubes.

$$\nu_e + \mathrm{n} \rightarrow \mathrm{p} + \mathrm{e}^- \tag{5}$$

- **neutral current interaction**
  Every neutrino flavor can dissipate the deuteron to a single proton and a single neutron. The neutron can then be caught by a nearby deuteron where it emits a photon with 6 MeV or it can interact with a proton of the normal water in the surrounding material where it emits a photon of about 2.2 MeV. These high energetic photons can then Compton-scatter on electrons leading to Cherenkov radiation that can be registered by the photomultiplier tubes.

$$\nu_x + {}^2\mathrm{H} \rightarrow \nu_x + \mathrm{p} + \mathrm{n}. \tag{6}$$

- **elastic scattering with an electron**
  There is the possibility for elastic scattering directly at the electron in the atomic shell. This can happen for every neutrino flavor with the exchange of the neutral Z boson but the electron neutrino has the additional interaction channel via the exchange of a W boson. The electron will get part of the energy of the neutrino and will emit Cherenkov radiation that can be detected by the photomultiplier tubes.

$$\nu_x + \mathrm{e}^- \rightarrow \nu_x + \mathrm{e}^-. \tag{7}$$

The SNO experiment could not find a lack of neutrinos from the Sun because it is sensitive to all 3 neutrino flavors [6]. Thus, it discovered the neutrino mixing.

2.2 Neutrino oscillations

In the Standard Model of particle physics the neutrinos are massless weakly interacting fermions.

The new findings of SNO and others induced the need of a mathematical description of neutrino oscillations, i.e. the transformation of one neutrino flavor into another.

This is only possible when there are non-zero mass differences between the mass eigenstates as seen in equation 16.

It turns out that in a weak interaction process a neutrino is created with a known

flavor ν_α but then propagates as a set of mass eigenstates ν_j.
This can be described with the following equation:

$$|\nu_\alpha\rangle = \sum_{j=1}^{N=3} U_{\alpha j} |\nu_j\rangle \tag{8}$$

where α describes the flavor of the neutrino, j the mass eigenstate and $U_{\alpha j}$ the PMNS matrix, named after *B. Pontecorvo, Z. Maki, M.Nakagawa and S. Sakata* [15], which is a unitary mixing matrix connecting the set of eigenstates. The PMNS matrix can be explicitly written as

$$U = \begin{pmatrix} U_{\mathrm{e}1} & U_{\mathrm{e}2} & U_{\mathrm{e}3} \\ U_{\mu 1} & U_{\mu 2} & U_{\mu 2} \\ U_{\tau 1} & U_{\tau 2} & U_{\tau 3} \end{pmatrix} \tag{9}$$

$$= \begin{pmatrix} 1 & 0 & 0 \\ 0 & \mathrm{c}_{23} & \mathrm{s}_{23} \\ 0 & -\mathrm{s}_{23} & \mathrm{c}_{23} \end{pmatrix} \begin{pmatrix} \mathrm{c}_{13} & 0 & \mathrm{s}_{13}\mathrm{e}^{-\mathrm{i}\delta} \\ 0 & 1 & 0 \\ -\mathrm{s}_{13}\mathrm{e}^{\mathrm{i}\delta} & 0 & \mathrm{c}_{13} \end{pmatrix} \begin{pmatrix} \mathrm{c}_{12} & \mathrm{s}_{12} & 0 \\ -\mathrm{s}_{12} & \mathrm{c}_{12} & 0 \\ 0 & 0 & 1 \end{pmatrix} \begin{pmatrix} \mathrm{e}^{\frac{\mathrm{i}\alpha_1}{2}} & 0 & 0 \\ 0 & \mathrm{e}^{\frac{\mathrm{i}\alpha_2}{2}} & 0 \\ 0 & 0 & 1 \end{pmatrix}, \tag{10}$$

where $c_{ij} = \cos(\theta_{ij})$, $s_{ij} = \sin(\theta_{ij})$, θ_{ij} is the mixing angle of the neutrino mass eigenstates, δ is a possible phase making CP violation possible and α_i accounts for the case of not having Dirac neutrinos but Majorana neutrinos. For the case of Dirac neutrinos the parameters α_i are vanishing. The difference between Dirac and Majorana particles is that Majorana particles are their own antiparticles.
As already mentioned the neutrino flavors are propagating immediately after their production as mass eigenstates so the flavors are not constant in time. This means that the flavor is not an eigenstate of the time evolution parameter in contrast to the mass eigenstates. That is why, by applying the Schrödinger equation, the mass eigenstates can be described by plane waves with t being the time after the production of the neutrino, E_j and $\vec{p_j}$ the energy and the momentum of the neutrino in the mass eigenstate j and $\vec{x}$ the distance from the origin:

$$|\nu_j(t)\rangle = |\nu_j(0)\rangle \cdot e^{-i(E_j t - \vec{p_j}\vec{x})/\hbar}. \tag{11}$$

For highly relativistic neutrinos there is the approximation for the momentum p with $m^2c^2 << E^2$:

$$p = \frac{1}{c}\sqrt{E^2 - m^2c^2} \approx \frac{1}{c}\left(E - \frac{m^2c^4}{2E}\right) \tag{12}$$

and with $t = x/c$ follows

$$|\nu_j(x)\rangle = |\nu_j(0)\rangle \cdot e^{-i\frac{m_j^2 c^4}{2E}\frac{x}{\hbar c}}. \tag{13}$$

The probability for a neutrino flavor α to change its flavor to β is then described by:

$$\begin{aligned} P_{\alpha\to\beta}(L) &= |\langle \nu_\beta(L)|\nu_\alpha(0)\rangle|^2 &(14)\\ &= \left|\sum_i U^*_{\alpha i} U_{\beta i} e^{-i\frac{m_i^2 L}{2E}}\right|^2 &(15)\end{aligned}$$

This can be written in another form splitting up the imaginary and the real part:

$$\begin{aligned} P_{\alpha\to\beta}(L) = \delta_{\alpha\beta} &- 4\sum_{i>j} \mathrm{Re}\left(U^*_{\alpha i} U_{\beta i} U_{\alpha j} U^*_{\beta j}\right) \sin^2\left(\frac{\Delta m_{ij}^2 L}{4E}\right) \\ &+ 2\sum_{i>j} \mathrm{Im}\left(U^*_{\alpha i} U_{\beta i} U_{\alpha j} U^*_{\beta j}\right) \sin\left(\frac{\Delta m_{ij}^2 L}{2E}\right). \end{aligned} \tag{16}$$

Hereby $\Delta m_{ij}^2 = m_i^2 - m_j^2$ is describing the difference of the squared masses of the mass eigenstates of i and j. One can see that the oscillation between the flavors depends on the difference between the quadratic masses of the mass eigenstates.

The first experiment that was really able to prove neutrino oscillation by investigating different flying distances of the neutrinos and therefore different phases in neutrino oscillations was the Super-KAMIOKANDE experiment [8]. It detects neutrinos that are produced by hadronic showers in the atmosphere.
The Super-KAMIOKANDE experiment is placed in the Kamioka mine 1000 m deep under earth to reduce cosmic radiation. It has a big water tank with 50,000 tons of ultra pure water and is surrounded by 11,200 photomultiplier tubes. The detection principle is based on the elastic scattering of neutrinos with electrons as described in 2.1 but also on the charged current interaction described in 2.1. Due to the higher energies of the atmospheric neutrinos in the multi GeV range in comparison to solar neutrinos being in the multi MeV range, the charged current interaction has an additional channel, which is

$$\nu_\mu + \mathrm{n} \to \mathrm{p} + \mu^- \tag{17}$$

because the muon neutrino has a rest mass of $m_\mu = 106\,\mathrm{MeV}$. Consequently there are high energetic electrons and muon that are traveling faster than the speed of light in the water leading to Cherenkov radiation which can be measured.

The measured neutrino flux revealed a strong dependence on the angle to the earth. This can be attributed to the following explanation: Due to different flying distances of the neutrinos that arrive from different directions the phase in neutrino oscillation causes a strongly different distribution of neutrino flavors especially when having initially muon neutrinos. In figure 2.2 only muon neutrinos are considered that cause muons to emit Cherenkov radiation with multiple GeV. This is done because muon neutrinos are changing their flavor much faster than electron neutrinos due to their different composition of mass eigenstates. Further because of the large energy of the neutrinos the oscillation period that, according to 15, depends on $1/E$ is well observable within distances in the diameter of the earth. By fitting the model of neutrino oscillation to the observed number of events one can extract mass differences of the neutrino mass eigenstates.

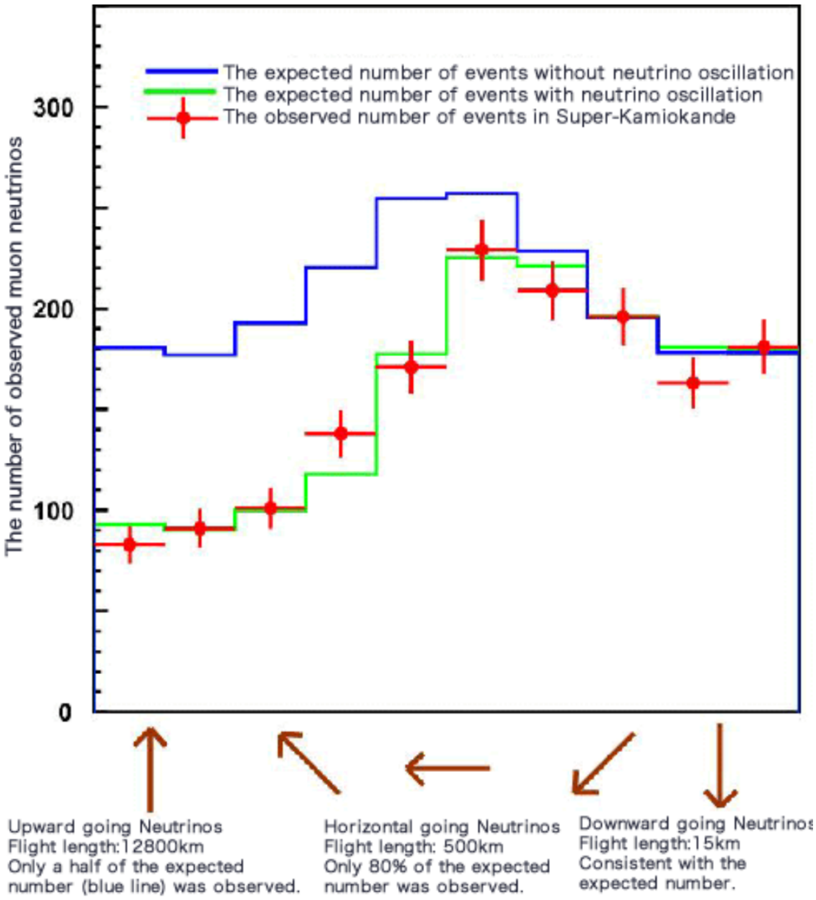

Figure 2.2: Data of the Super-KAMIOKANDE experiment. One can see that there is a significant deviation between the expectations without neutrino oscillations to the obtained data. However the data can be well described with a model of neutrino oscillations. Taken from [16].

2.3 Methods to determine neutrino mass

As mentioned in the introduction there are basically three types of measurements for determining the neutrino masses. These are on the one hand model dependent investigations of neutrinoless double beta decays and on the other hand model independent investigations of the kinematics of electrons in a single beta decay. Additionally there is the possibility to examine the neutrino masses with highly model dependent cosmological methods but this will not be discussed further within this thesis.

Neutrinoless double beta decay Investigations of the nuclear double beta decay:

$$(Z, A) \rightarrow (Z+2, A) + 2e^-(+2\nu_e) \tag{18}$$

of special isotopes, may allow for neutrino mass measurements and determining the mass hierarchy of the mass eigenstates. For these kinds of experiments isotopes are used that are stable under single beta decay but can undergo double beta decay as one can see in figure 2.3 where the ^{76}Ge can only decay via a double beta as the single beta decay would not lead to a lower mass excess.

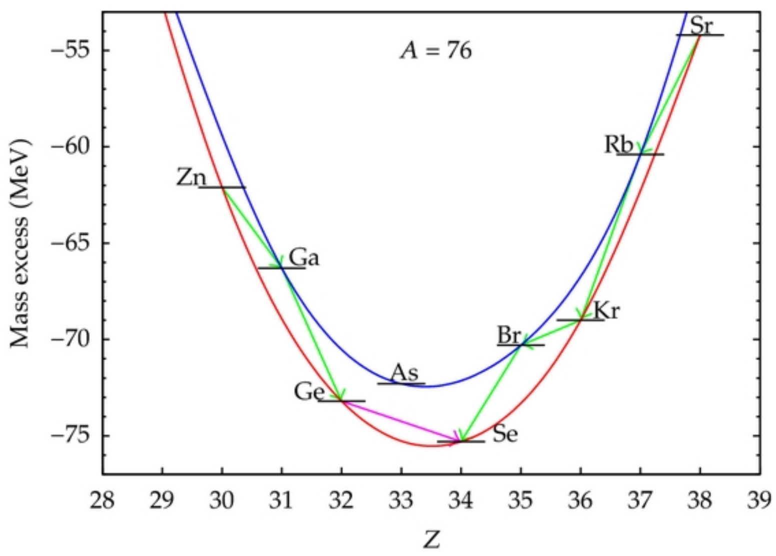

Figure 2.3: Beta decays for isobars with atomic number A=76. One can see that for Ge a single beta decay would not lead to a lowered mass excess and thus only the double beta decay can happen. Taken from [17].

For this purpose, the energy spectrum of the two emitted electrons is measured in coincidence. Thereby one obtains a continuous beta spectrum for the normal case in which two neutrinos are emitted. In the case of a neutrinoless double beta decay there would be a very sharp line exactly at the endpoint energy of the decay for the sum of both electrons because then it is not a three body decay anymore but the electrons have to carry off the entire energy of the decay. This is illustrated in figure 2.4.

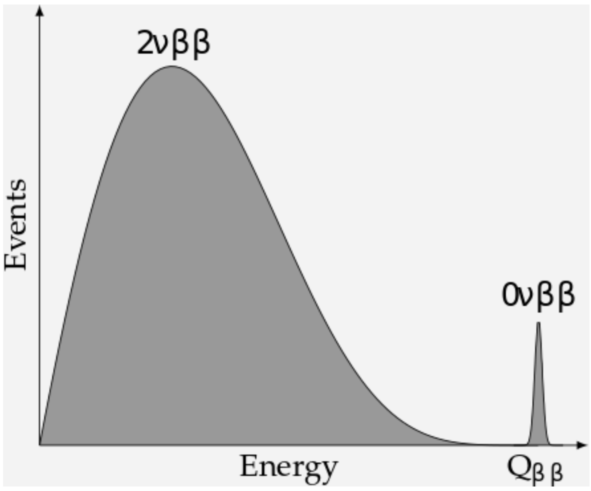

Figure 2.4: Energy spectrum of double beta decays. The small peak at the right side of the plot represents the neutrinoless double beta decay if neutrinos are Majorana particles. Taken from [18].

The latter mentioned process is only possible when neutrinos are Majorana particles instead of Dirac particles. In contrast to Dirac particles the Majorana particles have the same properties as their antiparticles. This would be necessary to observe the neutrinoless double beta decay, because in this decay an electron antineutrino is emitted twice, so they can only annihilate if they are their own antiparticles.
This type of measurement is used for example at the GERDA experiment that uses the isotope ^{76}Ge simultaneously as source and as detector material. This experiment is background free as it has in its region of interest no background counts. However, it has not observed any neutrinoless double beta decay, it provides the most stringent lower limit for it to $T^{0\nu}_{1/2} > 1.8 \cdot 10^{26}\,\mathrm{yr}$ (90 % C.L) [19].
This lower limit on the half-life of the decay can be translated to an upper limit of the neutrino mass with the formula:

$$\left(T^{0\nu}_{1/2}\right)^{-1} = G^{0\nu}\left(Q, Z\right)\left|M^{0\nu}\right|^2 \left(\frac{\langle m_{\beta\beta}\rangle}{m_e}\right)^2 \tag{19}$$

where $G^{0\nu}\left(Q, Z\right)$ is the phase space integral dependent on the Q-value and the atomic mass Z. $M^{0\nu}$ represents the nuclear matrix element.

Conclusively, an upper limit of $m_{\beta\beta} < (0.079 \text{ to } 0.180)\,\text{eV}$ (90 % C.L.) can be determined dependent on the nuclear matrix element $M^{0\nu}$ that is deviating between different models [19].

Direct measurement using kinematics of weak decay Another possibility to determine the mass of neutrinos is to analyze the kinetic energy of the electrons in the beta decay. The idea is to investigate the endpoint region of the beta decay where the shape of the energy spectrum contains information about the neutrino mass. Different neutrino masses lead to a different shape of the spectrum near the endpoint as visualized in figure 2.5.

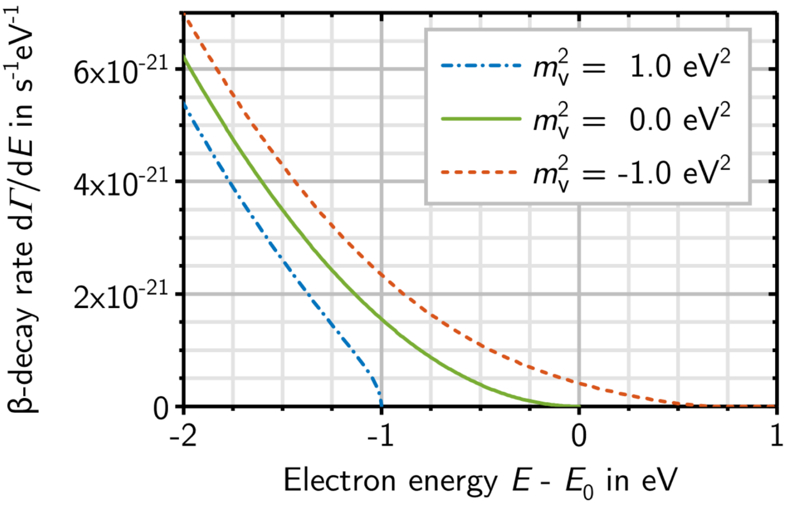

Figure 2.5: Spectral shapes of electron energies in a beta decay near the endpoint energy for different squared neutrino masses m_ν^2. Taken from [20].

The former experiments using this kinetic energy approach were the Mainz and Troisk experiments which were able to set a lower limit of $m_{\nu_e} < 2\,\text{eV}$ (90 C.L.) [21][22]. To further increase the sensitivity, larger dimensions of the experiment are required, which is implemented in the KATRIN experiment. The KATRIN experiment is further described in the following section.

3 The KATRIN Experiment

The KATRIN experiment aims to measure the absolute neutrino mass scale with a sensitivity of 200 meV in a model independent way by the precise measurement of the integral beta decay spectrum of tritium [10]. For achieving this goal very low intrinsic background in combination with a high resolution energy filtering of electrons is needed.

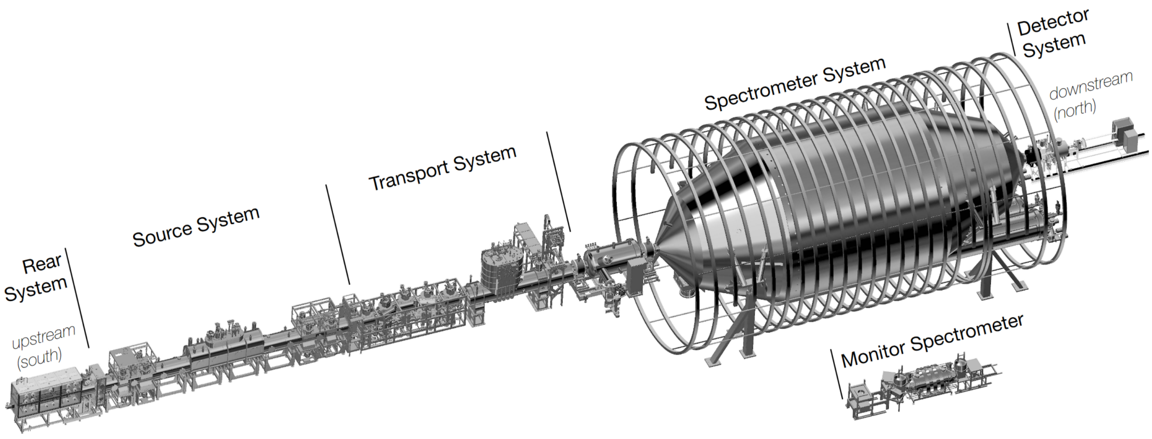

Figure 3.1: Beamline of the KATRIN experiment. Taken from [23].

In this chapter the KATRIN experiment is described at first in general and then its different parts will be explained separately. In the end of the chapter in section 3.2 the most relevant background processes are presented.

As visible in figure 3.2 only the very last tail of the beta decay spectrum is influenced by the neutrino mass which is also described by equation 20 for the kinetic energy spectrum in the beta decay [10]:

$$\frac{dN}{dE} = C \cdot F(Z,E) \cdot p \cdot (E + m_e c^2) \cdot (E_0 - E) \cdot \sqrt{(E_0 - E)^2 - m_\nu^2} \cdot \Theta(E_0 - E - m_\nu) \tag{20}$$

with

$$C = \frac{G_F^2}{2\pi^3} \cos^2 \theta_C |M|^2.$$

Hereby $F(Z,E)$ is the Fermi function, p the momentum of the electron, E the kinetic energy of the electron, E_0 the maximal electron energy for $m_\nu = 0$ (endpoint energy), m_e the rest mass of electrons and m_ν the rest mass of the neutrino. Furthermore Θ is the Heaviside step function, G_F denotes the Fermi coupling constant, θ_C the Cabibbo

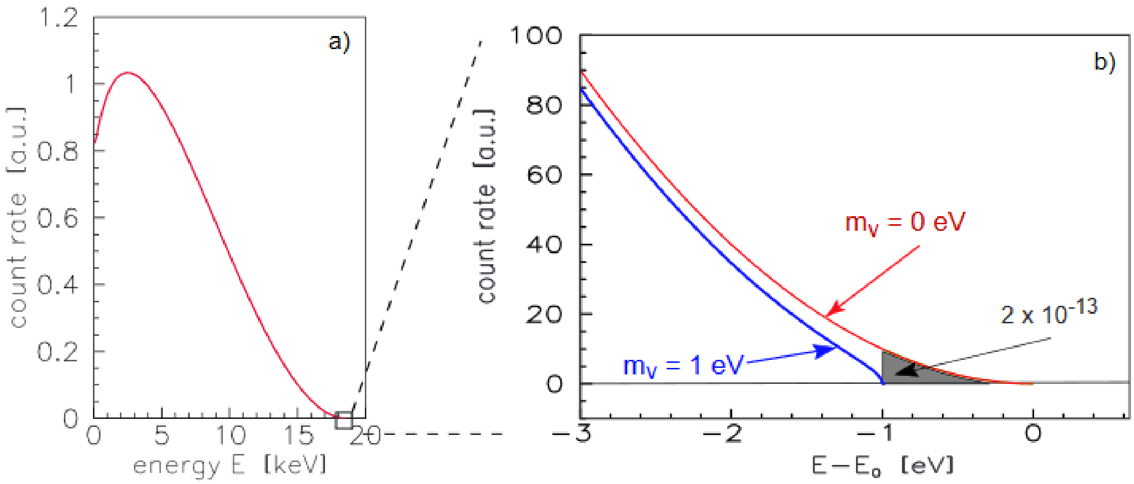

Figure 3.2: Electron energy spectrum for electrons originating from a tritium beta decay. The left plot describes the whole spectrum whereas the right one is taking a more detailed look into the endpoint region. The right plots shows the spectrum once for neutrinos with a rest mass of $m_\nu = 1\,\mathrm{eV}$ (blue) and once for a rest mass of $m_\nu = 0\,\mathrm{eV}$ (red). Only a fraction of $2 \cdot 10^{-13}$ electrons from the tritium beta decay have an energy of 1 eV below the endpoint. Figure taken from [24].

angle and M is the nuclear matrix element.
With regard to this equation it is clear that the count rate is rapidly rising from the endpoint energy to lower energies with $dN/dE \propto (E_0 - E)^2$. This means that the fraction of decays in the endpoint region scales with $(1/E_0)^3$ [10]. Conclusively, for getting the highest amount of electrons in the endpoint region, either the endpoint region should be as low as possible but nevertheless also the activity of the beta electron source should be as high as possible. For this purpose several isotopes have been evaluated as visible in table 1. Although tritium is molecular and not atomar, leading to rotational and vibrational states caused by the nuclear recoil, its structure is compared to the other evaluated isotopes very simple and can be physically well described. In combination with the high specific activity and a relatively low endpoint energy it is the most reasonable isotope for the KATRIN experiment.
The structure of the decaying isotope is important as one knows that the impact of neutrinos on the electron energy in the beta decay is very small and therefore even little deviations caused by the final state distribution of the atoms have to be considered. This is getting more and more elaborate for atoms with higher atomic numbers [20].

The use of tritium for this experiment is the reason why it is placed in Karlsruhe, because there is the "Tritium Laboratory Karlsruhe" which is allowed to handle a

Table 1: This table compares different isotopes of interest for direct neutrino mass experiment. The most important parameters are the column "Last eV" describing the ratio of electrons in the last eV in front of the endpoint of the beta decay spectrum and the source mass describing the mass of the isotope that is required to produce 1 event per day in the last eV of the spectrum. Despite the fact of not having the largest share of electrons in the endpoint region the high activity of tritum makes it a reasonable isotope for neutrino mass searches. Q_A is the atomic mass difference. Table taken from [25].

Isotope	Spin-Parity	Half-life y	Specific Activity Bq/g	Q_A eV	Branching ratio	Last eV	Source Mass g
$^3H_2$	$1/2^+ \rightarrow 1/2^+$	12.3	3.6×10^{14}	18591	0.57	2.9×10^{-13}	2.0×10^{-7}
^{115}In	$9/2^+ \rightarrow 3/2^+$	4.4×10^{14}	0.26	147	1.2×10^{-6}	5.0×10^{-7}	7.5×10^7
^{135}Cs	$7/2^+ \rightarrow 11/2^-$	1.5×10^6	6.8×10^7	440	$(0.04 - 16) \times 10^{-6}$	2.2×10^{-8}	0.4 - 217
^{187}Re	$5/2^+ \rightarrow 1/2^-$	4.3×10^{10}	1.6×10^3	2470	1.0	1.2×10^{-10}	57
^{163}Ho	$7/2^- \rightarrow 5/2^-$	4750	1.8×10^{10}	2858		$\sim 10^{-12}$	$\sim 1.0 \times 10^{-5}$

quantity of 40 g of tritium. This means that it has the highest availability of tritium in Europe, which is necessary to produce sufficient statistics.

To give a quick overview over the KATRIN beamline at first it is described superficially before in section 3.1 it is described in more detail.
The electrons that will be analyzed are produced in the beta decay of molecular tritium that is circulated through the 10 m long beam tube of the Windowless Gaseous Tritium Source (WGTS).
From there the beta electrons are guided by strong magnetic fields into the direction of the detector. At first the electrons are guided through the transport section where all the tritium is pumped out and only the electrons can pass. This filtering is feasible because of the different electric charge and the much fewer mass of the electron in comparison to tritium.
The next step is the spectrometer section containing the Pre-Spectrometer and the Main Spectrometer where the electrons are filtered by their longitudinal kinetic energy.
The last section is the detector section where only the electrons are counted that overcame the retarding potential of the spectrometers.
By applying different retarding potentials at the spectrometers one can measure the integrated spectrum of the beta decay in the endpoint region with the sensitivity to the neutrino mass of about 200 meV.

3.1 Experimental Setup

In this section the setup of the KATRIN experiment is described with its properties and functions ordered from source to detector.

3.1.1 Source and transport section

The Windowless Gaseous Tritium Source (WGTS) contains permanently an amount of about 40 μg tritium in it [26], producing approximately $9.5 \cdot 10^{10}$ beta decay electrons per second [11]. Therefore molecular gaseous tritium is injected in the middle of the 10 m long WGTS and diffuses to both ends. It has to be windowless, otherwise the electrons would not be able to get to the detector. However this also has the drawback that the tritium can not easily be stored but has to be pumped out very efficiently. Otherwise also the tritium would get into the spectrometer section and would increase the background. This pumping out of tritium is done by two pumping sections which will be described in the following paragraph. The WGTS is kept at a low temperature of 30 K with high stability of $\pm$30 mK to reduce Doppler broadening evoked by fast moving molecules [27]. Because of impurities of the tritium gas by hydrogen and deuterium molecules there is also done a measurement of the composition of these different molecules because it affects the count rate at the detector. This monitoring of the composition is done by Raman spectroscopy via a laser that is coupled into the tritium column. Measurements of the absorption of wavelengths allow the determination of the composition of atoms or molecules in this source [28].

The Differential Pumping Section (DPS) is in the beamline behind the source and has to filter out the tritium because otherwise it would contaminate the spectrometer and increase the background at the detector. While the electrons are guided by the magnetic field of several Tesla, the tritium molecules and ions are pumped out. The differential pumping section is illustrated in figure 3.3. It consists of a trapezoidal chicane where the direct line of sight is blocked and every other line in the trapezoid is tilted to 20°. Due to the blocking of the line of sight through the beamline the neutral tritium as well as the heavy ions can not be guided properly by the magnetic fields in contrast to the electrons and will at some point collide with the inner wall of the beamline. When this happens the neutral tritium as well as the heavy ions can be pumped out by the turbo molecular pumps at each side. With this procedure the neutral tritium flow can be reduced by about 5 orders of magnitude [29].
The pumped out tritium is cleaned and re-injected in the WGTS.

The Cryogenic Pumping Section (CPS) in principle looks very similar to the previous one but this section is cooled down to about 4 K and has an argon frost layer at the inner surface of the beamline. As a result, particles other than electrons that have made it to this point collide with the inner walls of the beamline due to the lack of or poor magnetic guidance. The argon frost layer has the effect that tritium sticks a very long time due to cryogenic adsorption onto the argon frost layer and will not get into the spectrometer section. Thereby the tritium flow is once more reduced by about 9 orders of magnitude. So, in combination, a suppression of 14 orders of magnitude is achieved and the effect of the residual tritium is negligible for the results in neutrino mass analysis, as it only increases the background by less than 1 mcps [24].
The argon frost layer has to be removed after 60 days because of saturation with tritium and by this it marks the natural end of each beta electron scanning period. The removing of tritium is done by heating up the beamline to 100 K and closing the valve to the spectrometer section to avoid that tritium reaches the spectrometers [30][31].

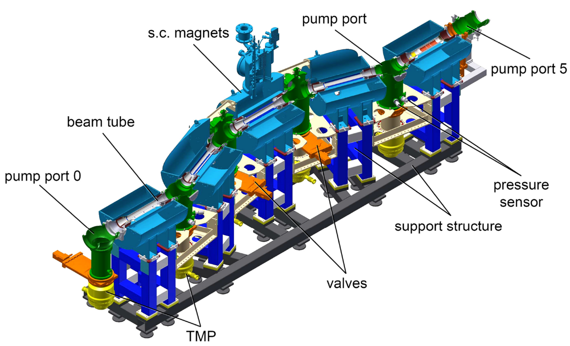

(a) Differential Pumping Section (DPS)

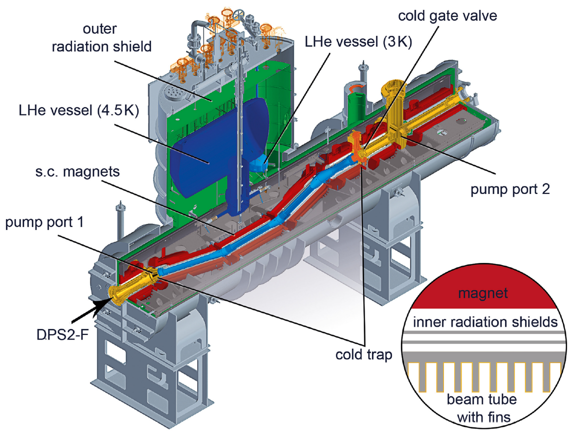

(b) Cryogenic Pumping Section (DPS)

Figure 3.3: Scheme of the pumping sections in the transport section. Within the DPS the direct line of sight is blocked by having a trapezoidal chicane. Thereby the electrons are magnetically guided to not hit the inner walls of the beamline whereas tritium molecules and ions are pumped out at each side via turbo molecular pumps to reduce tritium by 5 orders of magnitude. The cryogenic pumping section (CPS) looks very similar but works with cryogenic temperatures of about 4 K and an argon frost layer. Due to the argon frost layer the tritium molecules are adsorbed and by this another 9 orders of magnitude suppression is achieved. Pictures taken from [32].

3.1.2 Spectrometer section

To reach an energy resolution in the sub-eV range at the KATRIN experiment there is used the principle of **M**agnetic **A**diabatic **C**ollimation with an **E**lectrostatic filter

(MAC-E Filter). With the dimensions and magnetic fields in nominal settings at the KATRIN experiment in principle an energy resolution of 0.93 eV is possible for electrons with an energy of 18.6 keV.
The spectrometer section consists of a Pre-Spectrometer and a Main Spectrometer. The Pre-Spectrometer can be used to roughly pre-filter electrons for longitudinal energy before the main spectrometer filters very precisely with a nominal resolution of 0.93 eV.

The electric and magnetic fields of the KATRIN experiment are visualized in figure 3.4. Here one can see that in the spectrometer entrance and exit there is a very high magnetic field and a very weak negative electric potential. Considering the path to the

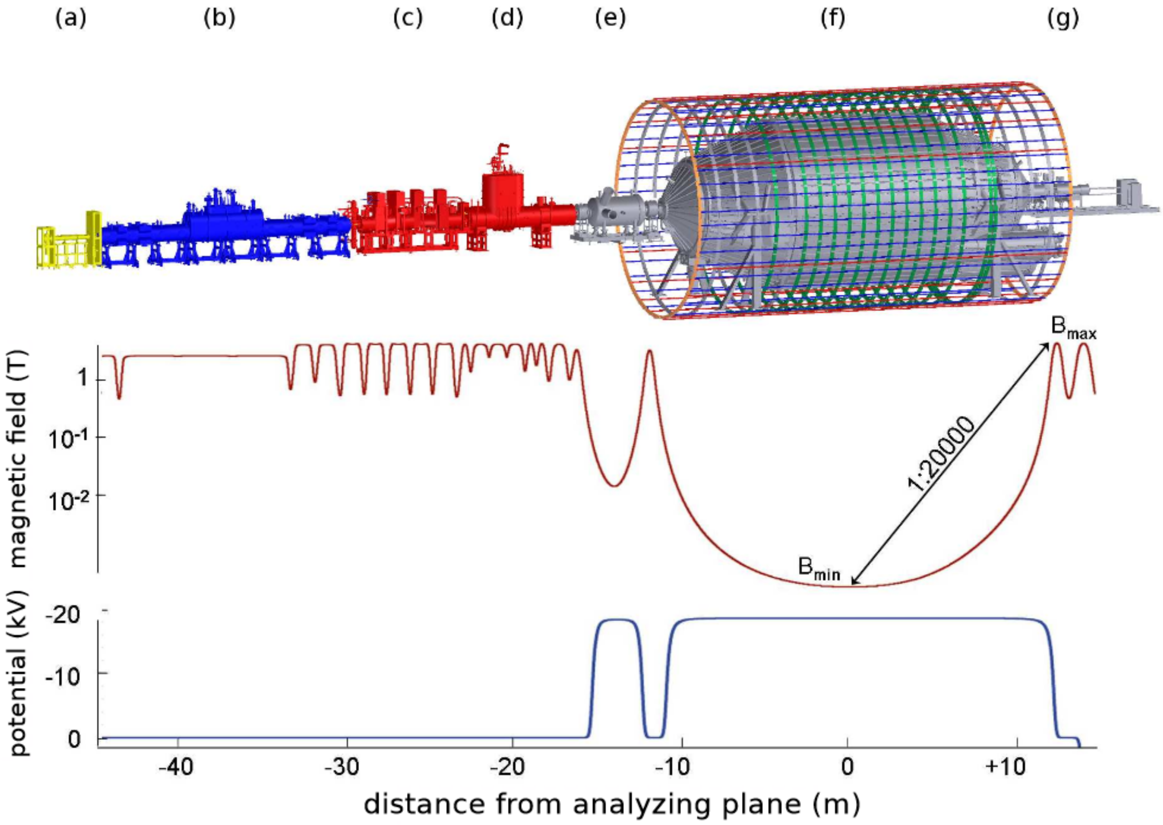

Figure 3.4: Visualization of the electric and magnetic fields at the KATRIN experiment in dependence on the distance from the analysing plane. The sections of the experimental setup are the Rear Wall (yellow), the Windowless Gaseous Tritium Source (blue), the transport section (red) containing the Differential Pumping Section (c) and the Cryogenic Pumping Section (d), spectrometer and detector section (grey) consisting of the Pre-Spectrometer (e), the Main Spectrometer (f) and the detector (g). Taken from [33].

middle of the spectrometer the magnetic field is strongly lowered to B_{min} whereas the

electric field is strongly increased to a maximum negative potential in the analyzing plane. The electric potential is generated by on the one hand the vessel which is set to a potential of about -18.4 keV and on the other hand there is installed an inner electrode system made by wires in little distance to the inner surface of the spectrometer. This inner electrode system has a potential of about -200 V lower than the vessel potential for preventing that low energetic electrons originating from the vessel can enter the spectrometer volume and increase the background.
The filtering is based on the electric potential. To overcome this potential electrons must have at least a longitudinal energy component of $E_{\|} = e \cdot U_{retard}$.
The angular distribution of electrons in the beta decay is isotropic so the energy does not only have a longitudinal but also a transverse component. That means by only using an electrostatic filter most of the electrons in the region near the endpoint will not be analyzed correctly because the electrostatic filter only analyzes the longitudinal energy.
To also take the electrons into account that are emitted with a non-zero angle to the z-axis, defined by the beamline axis, the transverse energy has to be transformed into longitudinal energy. This is done by the adiabatic guidance of the electrons which is the key feature to be able to use a large angular starting distribution of electrons in combination with high energy resolution.
Adiabatically means in this case, that the variation of the magnetic fields within one cyclotron period of the electrons is small so that the orbital momentum μ stays constant.

The transverse energy component $E_{\perp}$ proportionally decreases when the magnetic field B decreases

$$\mu = \frac{E_{\perp}}{B} = \text{const.} \tag{21}$$

So an electron that starts with a large transverse energy component $E_{\perp}$ at the WGTS in a strong magnetic field of B_{start} will undergo the adiabatic transformation to the analysis plane field B_{ana} according to

$$E_{\perp f} = E_{\perp i} \cdot \frac{B_f}{B_i}, \tag{22}$$

where B_i denotes the initial magnetic field and B_f the final magnetic field. Its transverse energy component decreases proportionally to the magnetic field ratio, for nominal KATRIN settings with a factor of $B_{\text{start}}/B_{\text{ana}} = 2.52\,\text{T}/0.3\,\text{mT} = 1/8400$.

However the maximal magnetic field is not at the WGTS but at the pinch magnet due to the usage of the magnetic mirror effect which will be described in the end of the

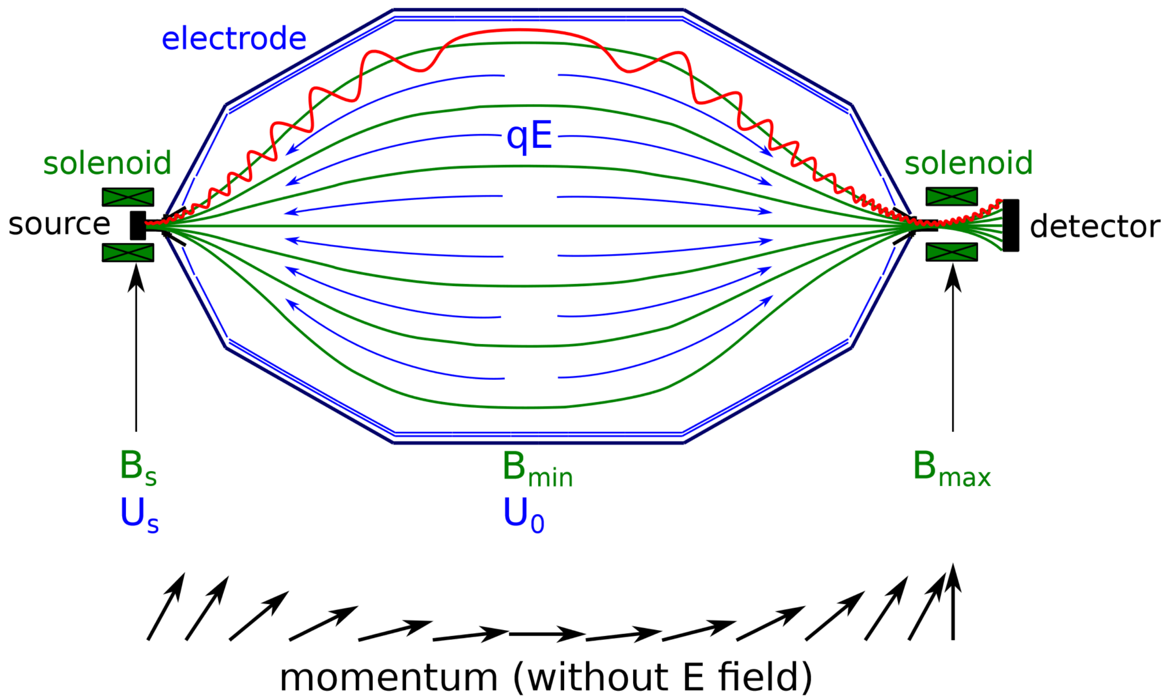

Figure 3.5: Working principle of the MAC-E filter. On both ends of the MAC-E filter there are solenoids with high magnetic fields of several Tesla and by moving to the middle of the vessel the magnetic field drops down several orders of magnitude. Thereby the transverse energy component of the electron is transformed into longitudinal energy. Additionally, a negative electric potential is applied which is highest in the analysis plane being in the lowest magnetic field. To be counted at the detector the electrons have to overcome the electric potential. Picture taken from [33].

current section. This higher magnetic field has the effect that the transverse kinetic energy is lowered even stronger with the factor of $B_{\text{max}}/B_{\text{ana}} = 6\,\text{T}/0.3\,\text{mT} = 1/20000$ for nominal settings.

The maximum remaining transverse energy in the analysis plane defines the energy resolution ΔE which the MAC-E filter is able to reach. It can be calculated when considering the case that the whole kinetic energy is stored in transverse kinetic energy:

$$\Delta E = 18.6\text{keV} \cdot \frac{B_{ana}}{B_{max}} = 0.93, \tag{23}$$

when the nominal values for the maximum magnetic field of 6 T at the pinch magnet and the minimum magnetic field of 0.3 mT in the analyzing plane are inserted.

The transmission function can be derived by some general considerations. The electrons have a total kinetic energy that splits up into two separate parts, the longitudinal energy $E_{\|}$ and the transverse energy $E_{\perp}$

$$E = E_{\|} + E_{\perp}. \tag{24}$$

However, the electrostatic filter only filters concerning the longitudinal kinetic energy $E_{\|}$. So for transmission the following condition must be fulfilled:

$$\begin{aligned} E_{\|} &= E - E_{\perp} > e \cdot U_{retard} \\ \Rightarrow E &- E_{\perp,i} \cdot \frac{B_f}{B_i} > e \cdot U_{retard}. \end{aligned} \tag{25}$$

The components of the kinetic energy can be written in dependence on the actual angle θ to the z-axis because of the dependence $E = \frac{1}{2}mv^2$ where $v_{\perp} = v \cdot \sin(\theta)$ and $v_{\|} = v \cdot \cos(\theta)$

$$\begin{aligned} E_{\|} &= E \cdot \cos^2(\theta) \\ E_{\perp} &= E \cdot \sin^2(\theta). \end{aligned}$$

Here, one has to mention that a relativistic correction is not needed because of the low kinetic energy in comparison to the rest mass of the electron leading to a maximum Lorentz factor of $\gamma = 1.04 \approx 1$.
Formula 25 can be rewritten as

$$E - E\sin^2(\theta_{start}) \cdot \frac{B_f}{B_i} > e \cdot U_{retard}. \tag{26}$$

Considering this inequality one can obtain a maximum starting angle of the electrons:

$$\theta_{start,max} \leq \arcsin\left(\sqrt{\frac{E_i - e \cdot U_{retard}}{E_i}\frac{B_i}{B_f}}\right). \tag{27}$$

This limits the angular acceptance Ω of the MAC-E filter. For an isotropic source like the electrons emitted from tritium beta decay the angular acceptance is

$$\Omega = \int_{\phi_0}^{\phi_1}\int_{\theta_0}^{\theta_1} \sin(\theta)\mathrm{d}\phi\mathrm{d}\theta. \tag{28}$$

In this setup there is axial symmetry around the z-axis so the integration over ϕ gives a factor 2π and θ_0 can be set to zero making the angular acceptance Ω only dependent on the maximum starting angle $\theta_1 = \theta_{start,max}$

$$\Omega = 2\pi[1 - cos(\theta_{start,max})]. \tag{29}$$

The transmission T through the MAC-E filter is then described by the ratio between the surface at the unitary sphere around an angle of θ (because the tritium decays isotropically so equally distributed in every direction) and the surface of the full direction to the detector which is 2π:

$$T = \frac{\Omega}{2\pi} = 1 - \cos(\theta_{start,max}). \tag{30}$$

By applying the relation $\cos\left(\arcsin\left(\sqrt{x}\right)\right) = \sqrt{1-x}$ one obtains the transmission function for the case of having the highest magnetic field at the WGTS:

$$T(E_0, U_{retard}) = \begin{cases} 0, & \text{for } E_0 < e \cdot U_{retard} \\ 1 - \sqrt{1 - \frac{E_0 - e \cdot U_{retard}}{E_0} \cdot \frac{B_{\text{start}}}{B_{ana}}} & \text{for } e \cdot U_{retard} < E_0 \leq e \cdot U_{retard} + \Delta E \\ 1, & \text{for } e \cdot U_{retard} + \Delta E \leq E_0 \end{cases} \tag{31}$$

In fact the highest magnetic field does not occur at the WGTS but at the pinch magnet at the spectrometer. Thus the transmission function has to take this into account as thereby the magnetic mirror effect occurs. This means the maximal starting angle has to be correct to

$$\theta_{start} \leq \arcsin\left(\sqrt{\frac{B_{start}}{B_{max}}}\right), \tag{32}$$

so that the transmission probability is limited to $T_{max} = 1 - \sqrt{1 - \frac{B_{start}}{B_{max}}}$. This is done to prevent having electrons with a very large angle to the z-axis because they are taking part on more scattering processes inside the WGTS due to a longer traveling distance

through the source leading to an energy loss of those electrons.
Overall this leads to the transmission function for KATRIN:

$$T(E_0, U_{retard}) = \begin{cases} 0, & \text{for } E_0 < e \cdot U_{retard} \\ 1 - \sqrt{1 - \frac{E_0 - e \cdot U_{retard}}{E_0} \cdot \frac{B_{\text{start}}}{B_{ana}}} & \text{for } e \cdot U_{retard} < E_0 \leq e \cdot U_{retard} + \Delta E \\ 1 - \sqrt{1 - \frac{B_{start}}{B_{max}}}, & \text{for } e \cdot U_{retard} + \Delta E \leq E_0 \end{cases} \tag{33}$$

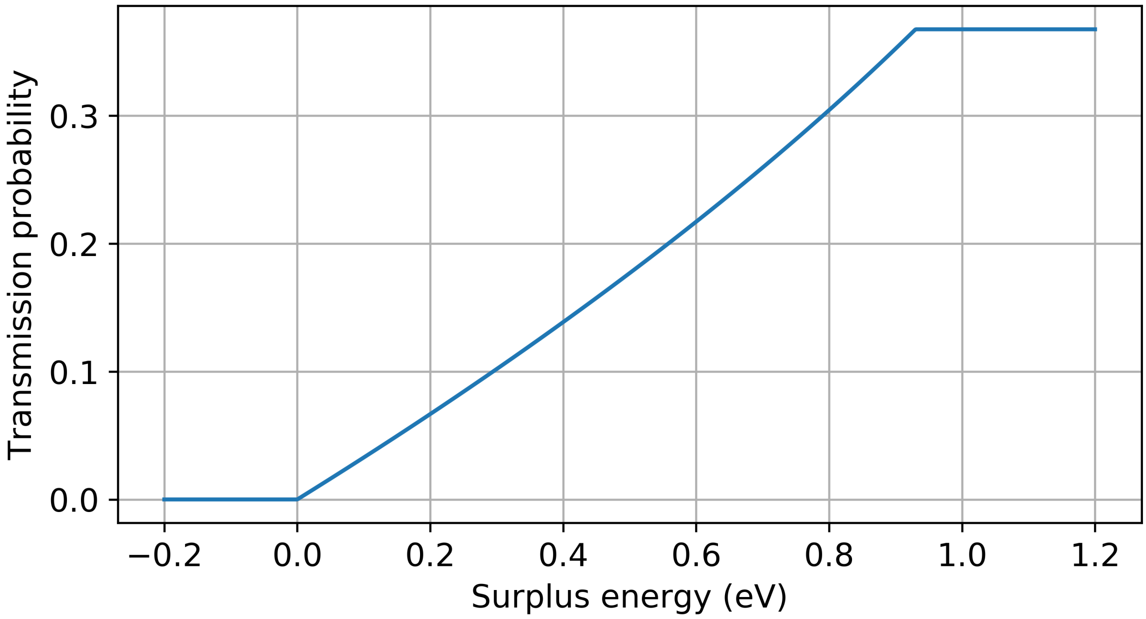

Figure 3.6: Transmission function for beta decay electrons to pass the main spectrometer for the KATRIN design values. The surplus energy is the energy above the retarding potential. Due to not having the maximum magnetic fields at the WGTS the maximum transmission probabiltiy is limited to about 37 % for surplus energies of at least 0.93 eV.

3.1.3 Detector

The focal plane detector (FPD) is a silicon PIN-diode which is separated in 148 pixel that are equivalent in area. It is optimized to have a very low intrinsic background, an energy resolution of (1.52 ± 0.01) keV FWHM and a high efficiency of 95%. Thus, the detector resolution does not allow direct measurements of the electron energy, but the analysis of the energy is already done by the spectrometers like explained in section 3.1.2. Consequently, in principle the detector only has the task to count every electron coming in. However, the energy resolution is useful to distinguish between signal and electronic noise.

Figure 3.7: Backside of the pixelized Focal Plane Detector. Taken from [34].

Moreover in front of the FPD there is a post acceleration electrode on which a negative potential of up to -10 kV can be applied. This is implemented to give an extra energy to the electrons so that the signal to noise ratio is larger because the electronic noise is exponentially decreasing for Si-PIN diodes to higher channel numbers [35]. In addition the detector provides spatial resolution because of the pixelized detector as one magnetic field line always guides electrons with the same starting conditions to the same pixel of the detector. With this principle one can make investigations for example to measure the alignment of the setup or to search for inhomogeneities and to minimize them. Also, it is possible to obtain pixel-wise or multi-pixel-wise neutrino mass analyses and more accurately account for systematic uncertainties.

3.2 Background

The components of the KATRIN experiment were manufactured using materials that have a very low intrinsic radioactivity but there are still processes that are producing background events. The KATRIN experiment aims for a sensitivity of 0.2 eV that can be reached, if the background does not exceed 10 mcps. However, the background rate was about 22 times higher in the second neutrino mass measurement campaign which shows the need for investigation and counteraction [11].

Electrons with very low kinetic energy originating from the vessel side can not enter the flux tube volume because the inner electrode system of the spectrometers are on a potential that is about 200 V more negative than the vessel potential. Thus, those electrons would be reflected. Furthermore the magnetic shielding prevents the low energetic electrons from outside the flux tube to get to the detector.
However, there are still processes leading to background. The two most important of

them will be described here in more detail.

3.2.1 Radon Background

To achieve a vacuum of less than 10^{-11} mbar there are installed non-evaporable getter pumps (NEG) in high quantity (60 kg). However the NEGs are emanating several radioactive radon isotopes that have different time scales to decay. Those are ^{219}Rn, ^{220}Rn and ^{222}Rn. ^{219}Rn has the smallest radioactive half-life of $t_{1/2} = 3.96\,s$ followed by ^{220}Rn with a radioactive half-life of $t_{1/2} = 55.6\,s$ and ^{222}Rn with the longest radioactive half-life of $t_{1/2} = 3.82\,d$. Considering that the average pump out time for the main spectrometer is $t_{MS} = 360\,s$ the ^{222}Rn isotope can be neglected as it will be pumped out very efficiently before decaying. Furthermore it could be seen that the impact of ^{220}Rn is at least 2 orders of magnitude lower then the impact of ^{219}Rn [36][37]. Consequently, concerning the NEGs only the ^{219}Rn is influencing the background. Due to its neutrality it will not be affected by the electromagnetic shielding and can reach the flux tube where it can decay via an alpha decay to ^{215}Po which will remain in an excited state. By several processes illustrated in figure 3.8 it can emit up to 20 electrons [37]. The majority of these electrons are highly energetic and mostly trapped because

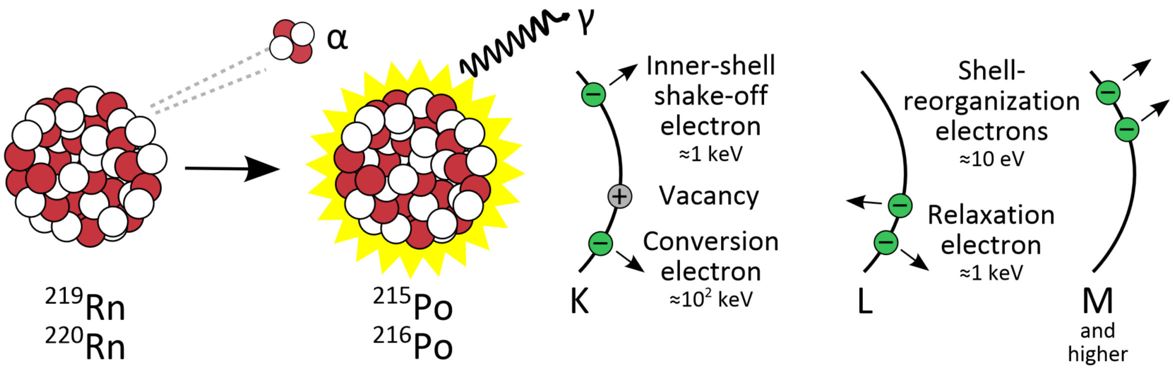

Figure 3.8: Decay processes of ^{219}Rn and ^{220}Rn. One radon atom can produce up to 20 electrons by various processes. Picture taken from [37].

of the strong changes in the magnetic field. Thereby the transverse energy rises and the longitudinal momentum decreases to zero and changes its sign every time they are entering a volume with high magnetic fields. This happens in the entrance and the exit of the spectrometer like illustrated in figure 3.9.

However these electrons can ionize residual gas molecules and thereby generate low energy electrons that can reach the detector and will produce background events.

As a countermeasure against this background there are installed liquid nitrogen cooled

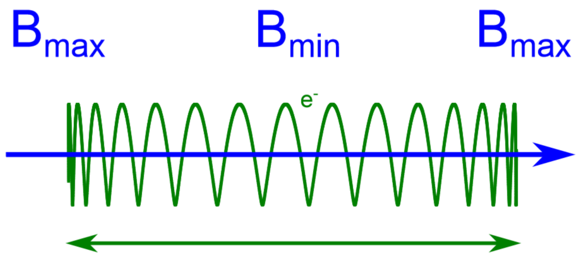

Figure 3.9: Scheme for magnetic reflection. An electron originating in a low magnetic field with high transverse energy component will be magnetically reflected at high magnetic fields being at the left and at the right side of the figure. Picture taken from [38].

baffles in front of the NEGs where the radon isotopes will stick at. This has the effect that the radon does not get into the flux tube but can decay outside of it so that the electrons originating from it do not contribute to the background.

3.2.2 Rydberg Background

There is also another kind of background electrons that have very low kinetic energy and arise in the spectrometer volume. Due to the electric potential in the spectrometer volume the signal electrons are strongly reduced in kinetic energy so that they are comparable to the low kinetic energy background which makes it hard to distinguish between each other. After several investigations of this background source it turned out that it is volume dependent. ^{222}Rn is suspected to be the source of this phenomenon [39].

Traces of it are present in the ambient air and thus it got into contact with the inner surface of the spectrometer while maintaining and installing the inner electrode system. For comprehension of the following explanation the decay chain of ^{222}Rn is described in figure 3.10. Bound on the surface of the inner spectrometer wall the ^{222}Rn will then decay in multiple steps with low radioactive half-life to ^{210}Pb with a radioactive half-life of 22.2 years. In between there were three alpha decays which have a non-negligible recoil energy with slightly above 100 keV each that can cause implantation of the daughter isotopes into sub-layers of the inner surface of the spectrometer [40]. ^{210}Pb has a rather long radioactive half-life compared to the measuring time of KATRIN so it will never be negligible in the period of the KATRIN measurement time. Sometimes a ^{210}Pb atom will decay via a beta decay to ^{210}Bi followed by a beta decay to ^{210}Po. Beta decays outside of the flux tube are not crucial as the electrons will not be guided to the detector but reflected by the electromagnetic shielding.

The only crucial step is the decay to ^{206}Pb via an alpha decay. An alpha decay gives

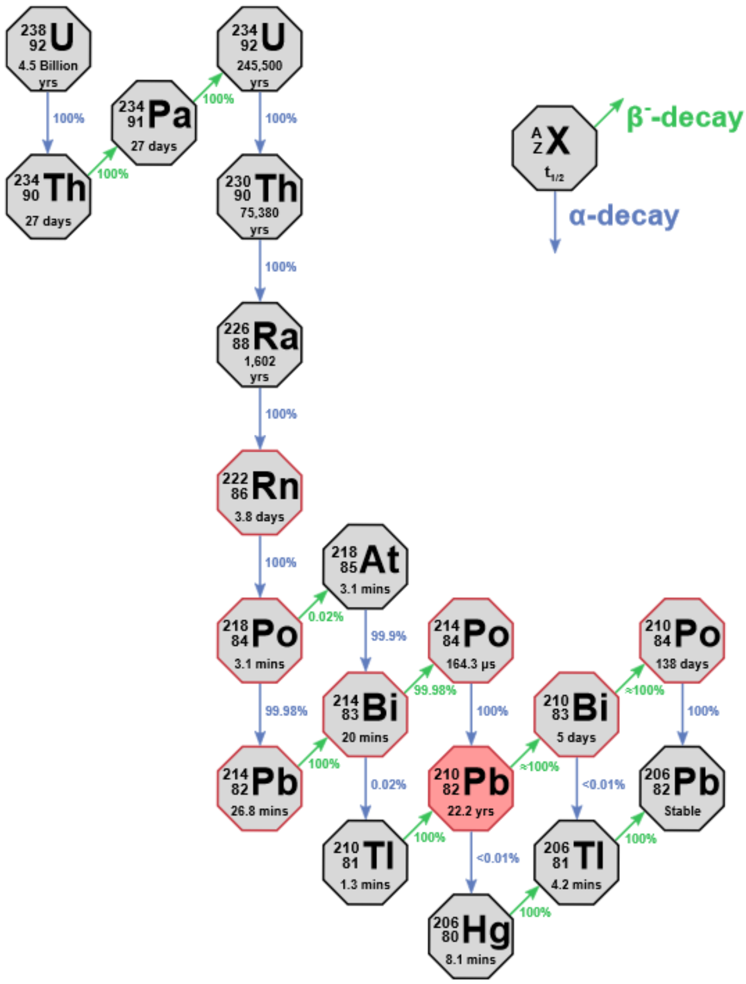

Figure 3.10: Decay chain of the radon isotope ^{222}Rn that is important for the Rydberg background process [37].

once more a non-negligible amount of recoil energy that can sputter off atoms from the inner surface of the spectrometer. Some of those sputtered off atoms, mostly hydrogen atoms, will remain in a very highly excited state but still neutral. Thus they can enter the flux tube volume undisturbed by the electromagnetic shielding. In the flux tube volume they can even be ionized by thermal radiation [40]. Those highly excited atoms are called Rydberg atoms and the de-excitation through thermal radiation leads to electrons with very low kinetic energy of typically $E_{kin} = k_B T \approx 25\,\mathrm{meV}$ [41]. Electrons generated by this process will be counted at the detector and can not be distinguished from the signal electrons because the kinetic energy is too similar.
To reduce the Rydberg background currently the shifted analysis plane mode is applied which bases on its volume dependency. In addition to that there are several new approaches that are described in the following section.

4 Background suppression

As described in the previous section there are processes at the KATRIN experiment that are producing a non-negligible amount of background electrons. This leads to a larger statistical uncertainty, which is by far the dominant source of uncertainties which can be seen in figure 2. That is why there are done some improvements at the

Table 2: Breakdown of uncertainties of the neutrino-mass-squared best fit of the KATRIN experiment in the second neutrino mass analysis campaign. Taken from [11].

Effect	68.2 % CL uncertainty on m_ν^2 (eV^2)
Statistical	0.29
Non-Poissonian background	0.11
Source-potential variations	0.09
Scan-step-duration-dependent background	0.07
qU-dependent background	0.06
Magnetic fields	0.04
Molecular final-state distribution	0.02
Column density $\times$ inelastic scat. cross-section	0.01
Activity fluctuations	0.01
Energy-loss function	< 0.01
Detector efficiency	< 0.01
Theoretical corrections	< 0.01
High voltage stability and reproducibility	< 0.01
Total uncertainty	0.34

KATRIN experiment and the most important ones will be briefly explained here.

Shifted Analyzing Plane (SAP) As mentioned in the section before the background induced by the de-excitation of Rydberg atoms depends on the volume between the analyzing plane and the detector.A measure against it is to reduce this volume. This can be done either by using a smaller flux tube by increasing the minimal magnetic field or the analyzing plane can be shifted towards the detector. The first approach would decrease the energy resolution as it is dependent on the ratio between the highest and the lowest magnetic field. The second variant, namely the Shifted Analyzing Plane, exchanged the original magnetic field setting at the KATRIN experiment and is now the standard setting for neutrino mass measurements [42]. The flux tube and the analyzing plane of the SAP setting as well as of the former nominal setting can be seen in figure 4.1.

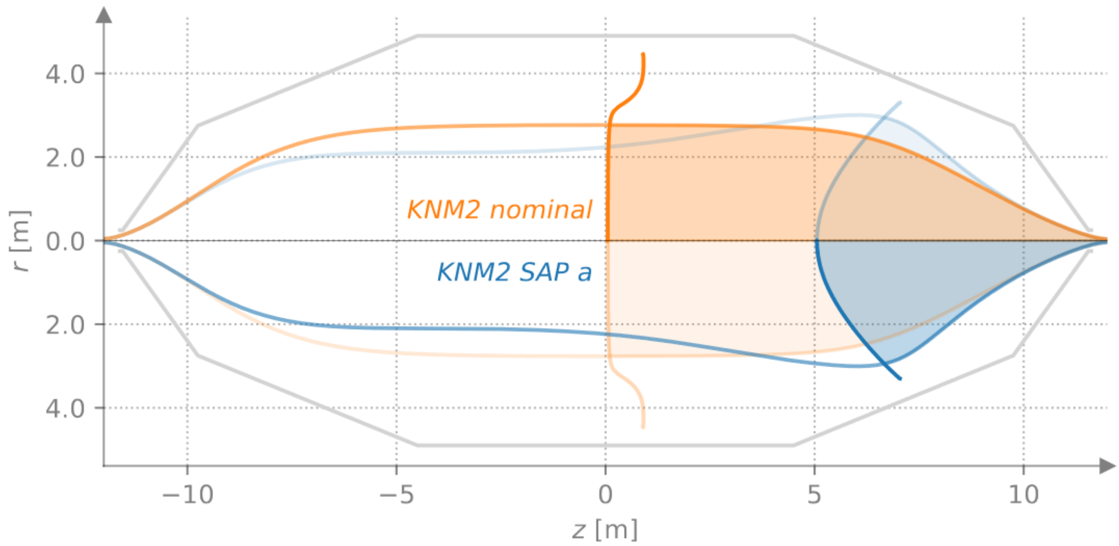

Figure 4.1: Simulation of the nominal setting with the analyzing plane in the center of the spectrometer compared to the SAP setting. The colored lines reaching from the entrance to the exit of the detector are describing the outer rim of the magnetic flux tube whereas the more vertical lines are describing the position of the minimal electric potentials along the magnetic field lines and thus the analysing plane. The blue colored lines are belonging to the SAP mode and the orange colored lines are belonging to the nominal mode. Taken from [42].

Liquid Nitrogen Cooled Baffles Due to the emanation of different radon isotopes from the NEGs there are installed liquid nitrogen cooled baffles between the inner volume of the spectrometer and the NEGs. These have the effect, that the radon isotopes will stick at the cooled baffles and decay there so that the electrons originating from it can not enter the flux tube and will therefore not contribute to the detected counts. For further information see section 3.2.1.

Time of Flight Techniques (not realized) For background in general there came up the idea of using a time focusing time of flight technique. The idea is that by using a time varying potential the electrons will arrive different in time dependent on the initial starting energy [43]. Thereby one will not only get an integral spectrum but a quasi differential one. This would increase the sensitivity in two ways. The first is because of the lower background as one can filter out electrons that are not in the expected energy region and the second is that one can hold the retarding potential constant but will still get information about the energy of the electrons by analyzing the time of the arrival. To realize this concept a third spectrometer would be required in the size of the Main Spectrometer which is very expensive, time consuming and would be a major

effort to install.
Another thought is to install a quantum electron tagger between the Pre-Spectrometer and the Main Spectrometer. It should have the task to produce a start signal when an electron is flying next to it but thereby it does not stop the electron completely. In this way a start signal would be obtained and with the signal at the detector one can calculate the time difference indicating the energy of the electron. So one does not only get an integral spectrum but also a differential one which would increase the sensitivity [44]. Furthermore by making coincidence measurements the background could be highly reduced.

UV Irradiation (not realized) There is an idea to actively de-excite Rydberg-atoms or transform them to isotopes with shorter half-life. That might be feasible with UV-irradiation of certain wavelength. There is active research on this topic within the KATRIN collaboration [45].

The idea that the master thesis will focus on is the use of the different angular distribution of the Rydberg background compared to the signal electrons, which will be presented in the following section.

4.1 Angular distribution of background by Rydberg atoms

As the Rydberg background arises by the de-excitation of Rydberg atoms through thermal radiation it is known that the energy of the electrons in the creation process have a typical energy of $E_{kin} = k_B \cdot T \approx 25\,\text{meV}$ [41]. By considering that the transverse energy is only generated when the electron is not emitted in direction of the magnetic field the typical transverse energy is due to three degrees of freedom, where two of them are contributing to transverse energy $E_{\perp,Ry} \approx \frac{2}{3} \cdot 25\,\text{meV}$ since the emission of electrons happens isotropically.
The resolution of the spectrometer is described by the ratio between the maximum magnetic field and the lowest magnetic field in the analysis plane. For current settings this is $E_{\perp,Sig} = 2.8\,\text{eV}$. So there are two orders of magnitude between them which corresponds to a very different angular distribution as visible at figure 4.2.

There one can see that the background induced by Rydberg atoms has a very narrow angular distribution with angles of up to about $\alpha_{\text{Rydberg}} \approx 10°$ whereas the signal electrons have an angular distribution depending from the maximum magnetic field at the pinch magnet. The overlapping area between signal and background by Rydberg atoms is very small. The idea is now to use these angular differences for the distinguishing between them. When it is possible to cut away angles from $0\,°$ to about $10\,°$ very

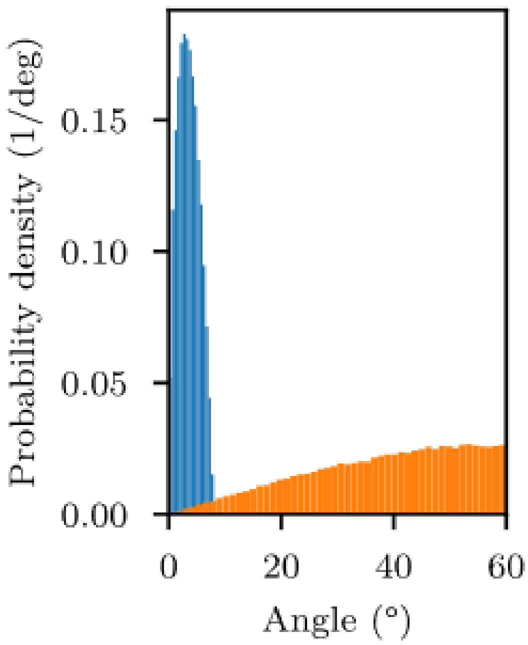

Figure 4.2: Angular distribution of Rydberg background (blue) and signal electrons (orange) for the design values of KATRIN in a 4.5 T field. Taken from [43].

efficiently then most of the Rydberg background would be vanished by still keeping most of the signal electrons which is very important for a low statistics experiment like the KATRIN experiment.
Therefore several ideas came up which will be presented in the following.

4.2 A passive Transverse Energy Filter

The idea came up to use a two layered grid made of wires behind each others in the beamline in front of the detector as sketched in figure 4.3 [41]. This grid should filter out electrons with a very small transverse energy because those electrons have small cyclotron radii and thus will mostly not have the chance to get along the wires. In contrast the electrons with larger transverse energies have a bigger chance to not be blocked and therefore to pass the filter. There are several parameters for optimization which are the distance between the two layers, the thickness of the wires and the gap between the wires. Furthermore the amount of layers behind each other can be used as a parameter but it turned out that with the best configuration about 95% of the Rydberg background could be theoretically reduced but also the signal electrons would be reduced by 75% [41]. Conclusively this would not increase the sensitivity because the statistics will get much lower which is very unfortunate for a low count rate experiment like the KATRIN experiment.

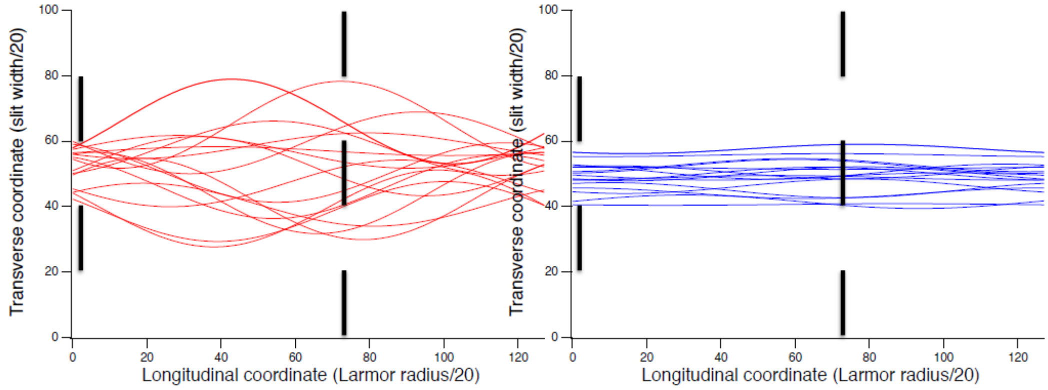

Figure 4.3: Idea of the passive transverse energy filter by R. G. H. Robertson. The colored lines are describing the trajectory for signal electrons (red) and Rydberg electrons (blue) through the passive transverse energy filter. The idea is that it filters out electrons with a small angular distribution (corresponding to Rydberg electrons) very efficiently whereas signal electrons have a higher probability to pass. Taken from [41]

But the idea of using a passive transverse energy filter lead to more thoughts about how to be able to use the different angular distributions of electrons so that Prof. Dr. Weinheimer came up with the idea to not use a passive angular electron filtering but an active angular filtering. In contrast to the previous filtering approach not the electrons that were able to pass the filter should be counted but the electrons that have been interacting with the filter should be registered. Therefore an activation of the filter is needed. The next chapter will follow this idea in more detail.

4.3 Angular selective electron detection with a microchannel plate detector

As it turned out a passive angular filter does not work for improving the sensitivity at the KATRIN experiment but an active filter could be worth the investigation. The idea behind it is that activation in this case means that a signal will be amplified in dependence of its transverse energy before reaching the detector. This means that electrons with small cyclotron radii which corresponds to low transverse energies (Rydberg background) should not be amplified whereas electrons with large cyclotron radii (corresponding to high transverse energies in comparison to Rydberg background) are amplified before reaching the detector. When amplification takes place then it means that an incident electron leads to an avalanche of low energetic electrons. With the usage of a post acceleration electrode all of these low energetic electrons will get a significant amount of kinetic energy. This makes it possible to distinguish between the case of low amplification for Rydberg electrons and high amplification for signal

electrons by applying a certain threshold that has to be overcome.
The idea is to use a microchannel plate detector for this which will be introduced in the next section.

4.3.1 Microchannel plate detector

A microchannel plate detector (MCP) is a type of a detector that can be used for positive and negative charged as well as for neutral particles and for photons which have a sufficient energy to emit secondary electrons at the channel walls.
The MCP consists of several millions of parallel channels with a channel diameter in the micrometer region and a channel length of several tens of micrometer to millimeter. In combination this is defining the aspect ratio $a = \frac{\text{lenght}}{\text{diameter}}$. In addition there is set a bias angle of the channels of a few degree to prevent electrons from flying through the channel without interaction and to prevent ion feedback that can damage the MCP. Another important parameter expressing the efficiency of electron detection is the open area ratio describing the ratio between the active area of the MCP detector and the whole area of the MCP detector, which is in the range of about 60%.

The working principle of an MCP is that it consists of channels where each channel works itself similar to a photo multiplier tube. That means an incoming particle hits the inside of the channel wall and will emit secondary electrons from the surface of the inner walls. Between the front side and the back side of the MCP there is applied a voltage of typically about 1 kV. This has the effect that the emitted secondary electrons are accelerated towards the back side of the MCP and will hit the other side of the inner channel wall. This process happens several times in a row, leading to an exponentially increasing output until a possible saturation is reached. This is illustrated in figure 4.4.

Concerning this a low aspect ratio in combination with long channels leads to more amplification because of the higher probability for the electrons to hit the walls several times and therefore for producing secondary electrons.
In the end one single MCP will generate a gain of 10^3 to 10^4.
In most cases not only a single MCP detector is used but a combination of multiple MCPs in a row.
One distinguishes between the most common forms:

- single MCP, only consisting of one MCP
- MCP in chevron stack, consisting of two MCPs in a row where the second one is rotated to 180° with respect to the other one. The scheme of it is shown in figure 4.5

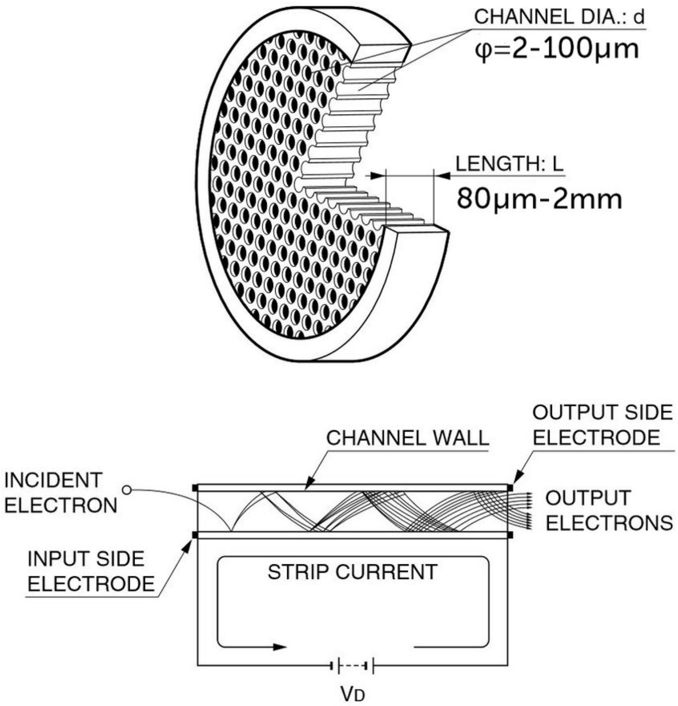

Figure 4.4: Working principle of an MCP. The MCP consists of many channels next to each other. Each channel is working similar to a single photo multiplier tube. An incoming particle or photon that hits a channel wall causes an avalanche of secondary electrons which will be registeres at the anode. For further information see section 4.3.1. Figure taken from [46]

- MCP in z-stack, consisting of three MCP in a row. In principle like a single MCP that is mounted behind an MCP in chevron stack where the single MCP has the same orientation of the channel like the first MCP

The more MCPs are arranged in a row, the higher the number of output electrons. The output electrons then arrive at the back side of the MCP where an anode is installed. The secondary electrons will hit the Anode and by this will generate a voltage drop which can be measured for example with an oscilloscope. Due to the strong intrinsic amplification the electronic noise is strongly suppressed and the signals are very distinct.

As described incoming electrons are only amplified and thus detected when initially hitting the inner surface of the channels. Furthermore amplification should best work for electrons with a relatively large angle to the orientation of the channels because then the probability for electrons to hit the channel walls directly at the entrance or at least

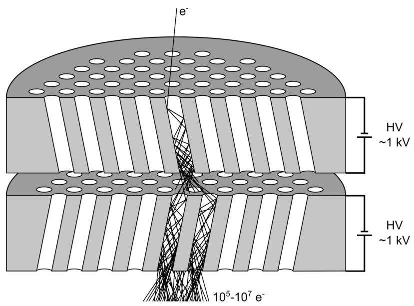

Figure 4.5: This shown an MCP in chevron stack meaning that there are two plates of MCPs rotated by 180° with little space between so that the secondary electrons from the first MCP can get into multiple channels in the second MCP. Hence, the secondary electrons will be amplified even stronger. Figure taken from [47].

in the front part is increased.[2] Angle-selective electron detection is based on this. When electrons are flying parallel to the channel orientation then the amplification should be highly suppressed because the exponential increase does not have large distance to evolve in the first MCP. The maximum reduction for an MCP in chevron stack would happen if the electron first hits the channel wall in the second MCP of the chevron stack configuration. This can not be prevented due to the fact that the second MCP is rotated by 180°. The process of exponential increase of secondary electrons in a chevron stack MCP can be seen in figure 4.5
So the idea for measurements is that the effect of lower amplification in combination with setting a threshold should lead to lower count rates for electrons flying parallel to the channels. Concerning the KATRIN experiment this would mean a reduction of the detection of Rydberg background leading to a better sensitivity. This effect will be investigated for the terms of this master thesis.

[2]However the angle of the electrons must not be too large with respect to the orientation of the channels because too large angles can cause that the electrons will not emit further secondary electrons but will be absorbed by the channel walls.

5 The Münster Test Setup

In this section the test setup is presented on which the investigations of the angular-selective electron detection effect are carried out. It is equipped with a photoelectron source (eGun), a magnetically guiding beamline and an MCP detector and was described in detail in [48].

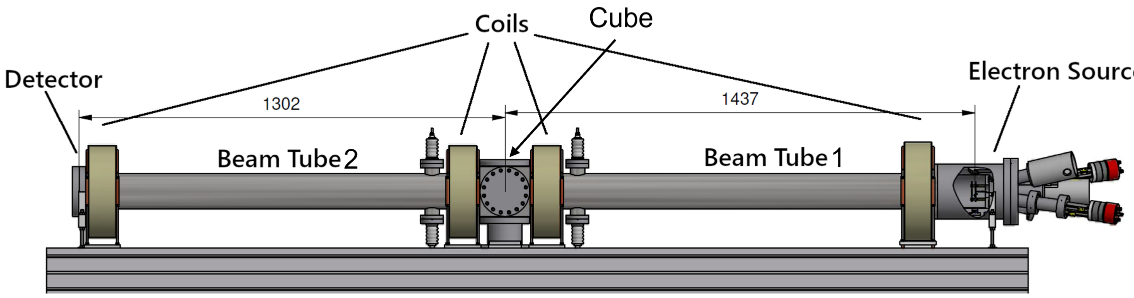

Figure 5.1: Scheme of the Münster test setup. The electrons are produced at the eGun on the right side and are guided by magnetic fields until they reach the MCP detector on the left side. Taken and edited from [48].

5.1 Dual MAC-E filter test setup

The Münster test setup is built to investigate ideas for the suppression of background in the KATRIN experiment and is about 3 meter long.
According to figure 5.1 on the right side there is the electron source which is a mono-energetic and angular selective single electron gun as described in more detail in section 5.2. Its electrons are guided via magnetic fields through several vacuum components which are the beam tubes (BT) and the cube. In the end of the beamline the electrons will be registered by the detector on the left side of the test setup. The detector is a microchannel plate detector which will also be explained in more detail in section 5.3. The coils for the magnetic setup are divided into air coils and beam tube coils (BTC) which are powered by power supplies of Delta Electronics (SM 15-200 D and SM 30-100 D). The first number of the model description for the power supplies denotes the maximum voltage and the second number the maximum current. The BTCs consist of 532.5 windings of lacquered copper wires with a diameter of 2 mm that are directly wound around the BT with an outer radius of 54 mm. These generate a basic magnetic field for the guidance of the electrons. Due to the fact that the copper wire is spiraling around the BTs there is a little component of the magnetic field in the entrance and

the output of the BT in radial direction giving an angle α with respect to the z-axis, defined by the beam line axis. This angle can be determined to

$$\begin{aligned}\alpha &= \arctan\left(\frac{2\,\mathrm{mm}}{2\cdot 54\,\mathrm{mm}}\right) \\ &= 1.06\,^\circ\end{aligned} \tag{34}$$

A continuous current of 25 A can be applied to the BTCs without damaging them. Additionally, there are air coils where transitions are between the BTs and other components. These are tape coils consisting of aluminum oxide and are 80 mm long with 382 windings. It has to be distinguished between the air coil located at the eGun and the others as the air coil at the eGun (from now on called eGun coil) has a slightly different core radius of 90 mm instead of 80 mm for the other air coils because it has to be able to surround the eGun parts which have a larger radius. The other coil parameters are similar. These air coils have a copper plate on both sides with a water pipe running through it and are glued with an adhesive tape that has a high temperature resistance up to 200 °C and a high thermal conductivity to dissipate the heat. With these precautions a constant current of about 35 A can be applied to the air coils.
These air coils have several tasks: Firstly, they serve to maintain the magnetic fields, especially at the cube in the middle, since the BTs are interrupted there over a length of 15.4 cm. Furthermore, the air coils can set the starting magnetic field for the generated electrons as well as the magnetic field at the detector to manipulate the angles and the cyclotron radii of the electrons.

In addition, cylindrical electrodes with a radius of 3.75 cm and a length of 0.95 m are installed within the experimental setup to form a MAC-E filter spectrometer as in the KATRIN experiment. These can be used for example to investigate the idea of time focusing time of flight techniques [43][49]. For setting the retarding potential there are high-voltage feedthroughs on both sides of the cube in the middle, one for each electrode. However, the electrodes remain unused in the experiment that are conducted in the scope of this thesis.
The cube in the middle is important for installing various vacuum components and has the option of installing items on each side. The most obvious one is the vacuum pumps to obtain a vacuum of about 10^{-7} mbar that is needed to get a sufficient free path length of the electrons and to commission the eGun as well as the detector working with high voltage to avoid flash overs. Additionally a pressure gauge is mounted.
Originally a coldhead in combination with a quantum electron tagger at the cube was thought be tested at this test setup as explained in section 4. But this idea is not yet

ready to be tested as it is still in development so it will not be discussed in more detail.

5.2 Angular-selective monoenergetic photoelectron source (eGun)

The eGun is an angular-selective and monoenergetic single electron source and the former Main Spectrometer eGun at the KATRIN experiment [50]. A photo of it can be seen at 5.2.
The emission of electrons works via the photo electric effect. Therefore the light of a UV-LED is coupled into a fiber which other end is installed at the copper coating at the back plate of the eGun as illustrated in 5.2.

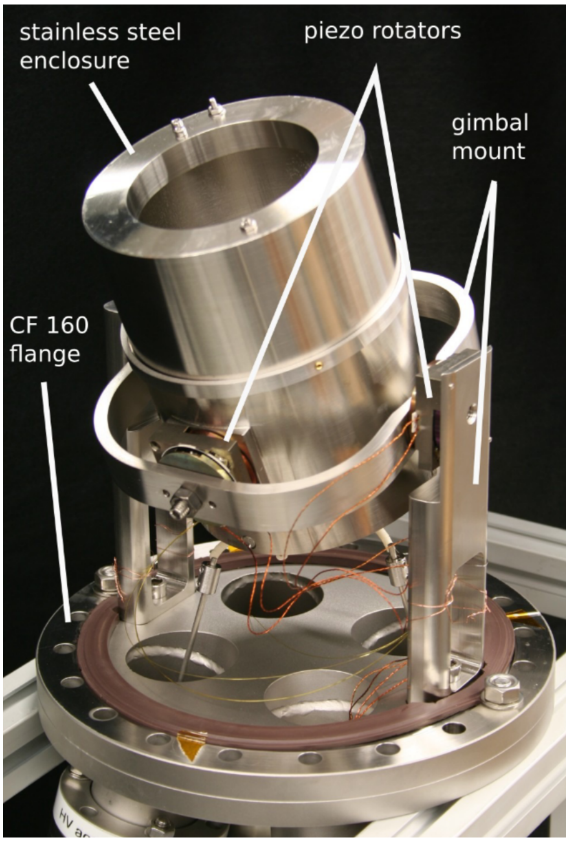

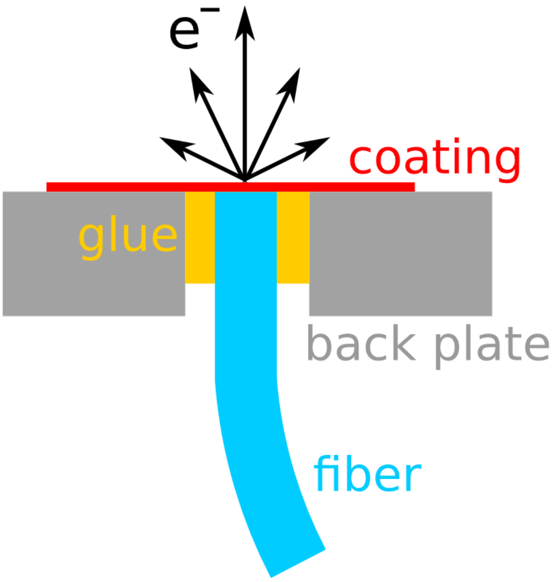

Figure 5.2: The left picture is the angular-selective and monoenergetic single electron source and the former main spectrometer eGun. The right figure describes how the fiber is glued at the coating of the back plate. UV light is guided through the fiber and produces electrons via the photoelectric effect at the coating. Taken from [51].

When the energy of a photon E_γ from the UV light is bigger or equal than the work function Φ of the coating $E_\gamma > \Phi$ then electrons be emitted from the material. These

electrons will additionally get accelerated by a potential at the back plate. The total energy received by the electron is thus determined by the potential at the back plate and the comparatively small residual energy of the photon.
The UV LED is used in combination with a pulse generator. There one can set the frequency with which the pulses are emitted as well as the duration and the amplitude of each pulse.

To not be limited to only setting the energy of the electrons also the angle of the back plate and front plate of the eGun can be varied in polar and azimuth direction. The front plate is parallel and in a distance of 8 mm to the back plate and set to 75% of the potential with respect to the back plate realized by a voltage divider. This has the effect of a homogeneous and, depending on the potential of the back plate, strong electric field. The change in angle of the plates causes that the acceleration of the electrons will get a certain angle with respect to the magnetic field lines. In combination with a strong electric field between the back plate and the front plate in this region the acceleration of the electrons happens non-adiabatically. This causes that the electrons do not follow the magnetic field lines in the region between the two plates and a polar and azimuth angle can be imprinted. A scheme of the eGun principle is illustrated in figure 5.3.

Regarding the formula for the Lorentz force 35

$$\vec{F_L} = e \cdot (\vec{E} + \vec{v} \times \vec{B}) \tag{35}$$

this principle works better the higher the electric field and the lower the magnetic field is between the plates. One can see that the kinetic energy determining the velocity v, describes the coupling to the magnetic field. Thus in the beginning when the electron has low kinetic energy the electric field component dominates the imprinting of the direction for the electrons until the kinetic energy gets large enough so that the magnetic field gets the dominant factor.

The eGun can be controlled with a LabView[3] program whose front panel is seen in the figure 5.4 and the readout is done with piezo electric motors (Attocube ANR240) for a very precise measurement. It is mounted on a gimble and can be steered with two pneumatic motors where one is rotating around an axis (x-axis) perpendicular to the z-axis and the other is rotating around an axis that is perpendicular the z-axis and to the x-axis (y-axis)[4]. On the left side of the front panel one can choose whether

[3]LabView is a graphical programming language from the company National Instruments and is used for laboratory work.
[4]Pneumatic motors are chosen for the usage in strong magnetic fields where electric motors would not work properly.

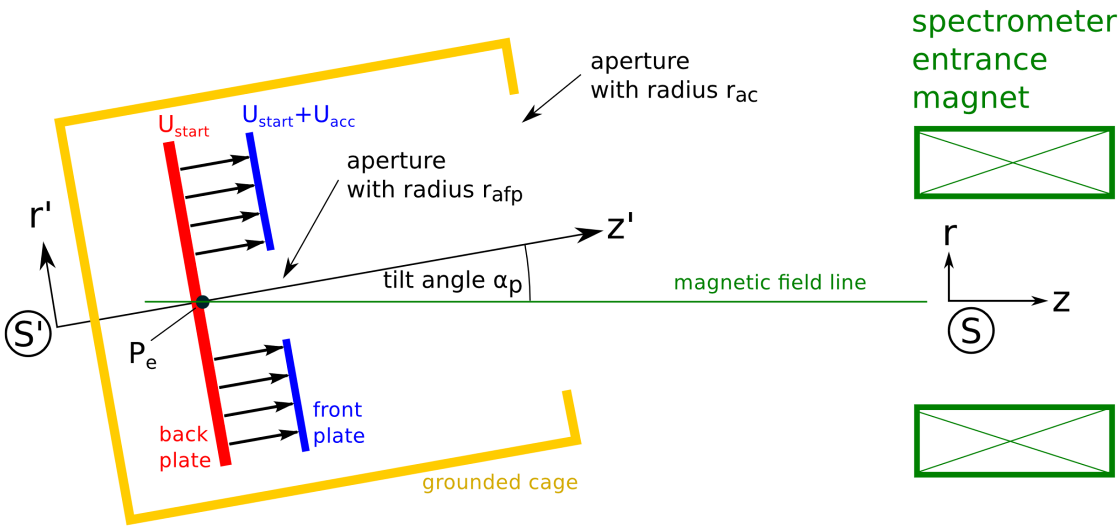

Figure 5.3: Scheme of the eGun. P_e marks on the one hand the point where the electrons are produced through the photoelectric effect but on the other hand the origin of the symmetry axis z' of the eGun which can be tilted to the z-axis defined by the central magnetic field line to create a polar angle. Additionally the eGun can be rotated around the z-axis to create an azimuth angle. The red plate (back plate) and the blue plate (front plate) are parallel to each other with a strong electric field for non-adiabatic motion of the electron in the region between. This makes it possible to set an angle to the electrons with respect to the magnetic field line. Taken from [51].

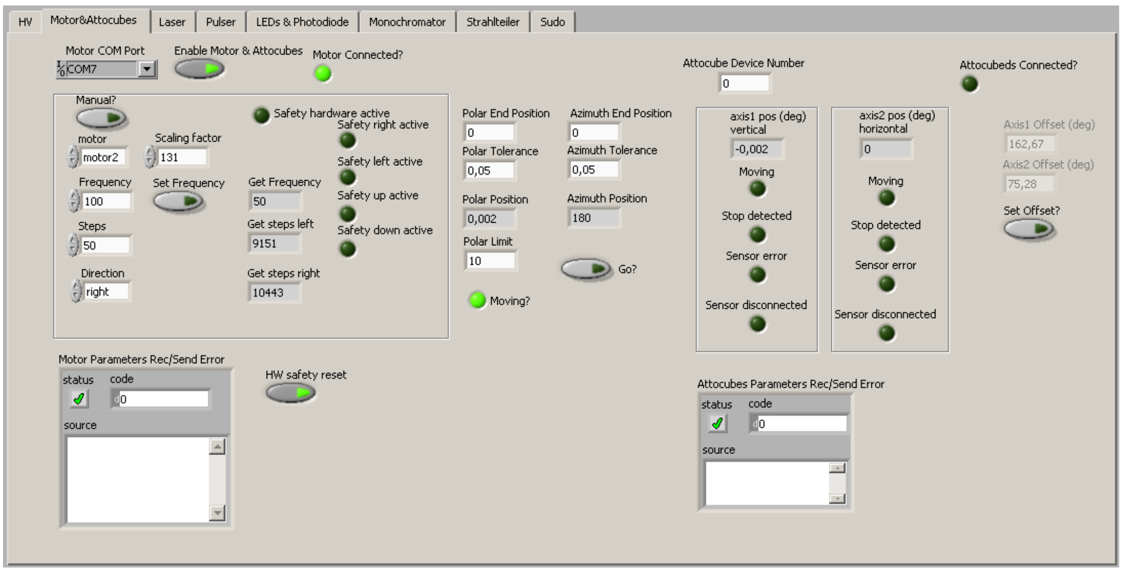

Figure 5.4: LabView control panel for the eGun and its associated hardware. Taken from [52].

changing one motor position manually by pushing the manual button or changing the angle of the eGun automatically. For the case of manual controlling, the motor can be chosen as well as the frequency of the stepper motors, the steps and the direction. These manual settings can be used for fine tuning like when the eGun needs to be aligned. For normal cases in measurements the manual operation mode should not be used. Instead in the middle part of the panel one can directly set the polar and azimuth angle. This is internally calculated by the positions of the two perpendicularly working motors. So there can be set a destination value and a tolerance with which it should be achieved. On the right side of the panel one can set the offset values. So there the offset values of *axis1* and *axis2* should be inserted when aligning the eGun and the $0\,^{\circ}$ position is found. In reference to this point the polar and azimuth angles are then calculated.

5.3 MCP Detector

For the upcoming measurements a microchannel plate (MCP) of the company Tectra is used with the detector code MCP-50-D-L-A-F. This MCP detector can be seen in figure 5.5. It has an open area ratio of $r \geq 60\,\%$ and an active diameter of $d \geq 44\,\text{mm}$.

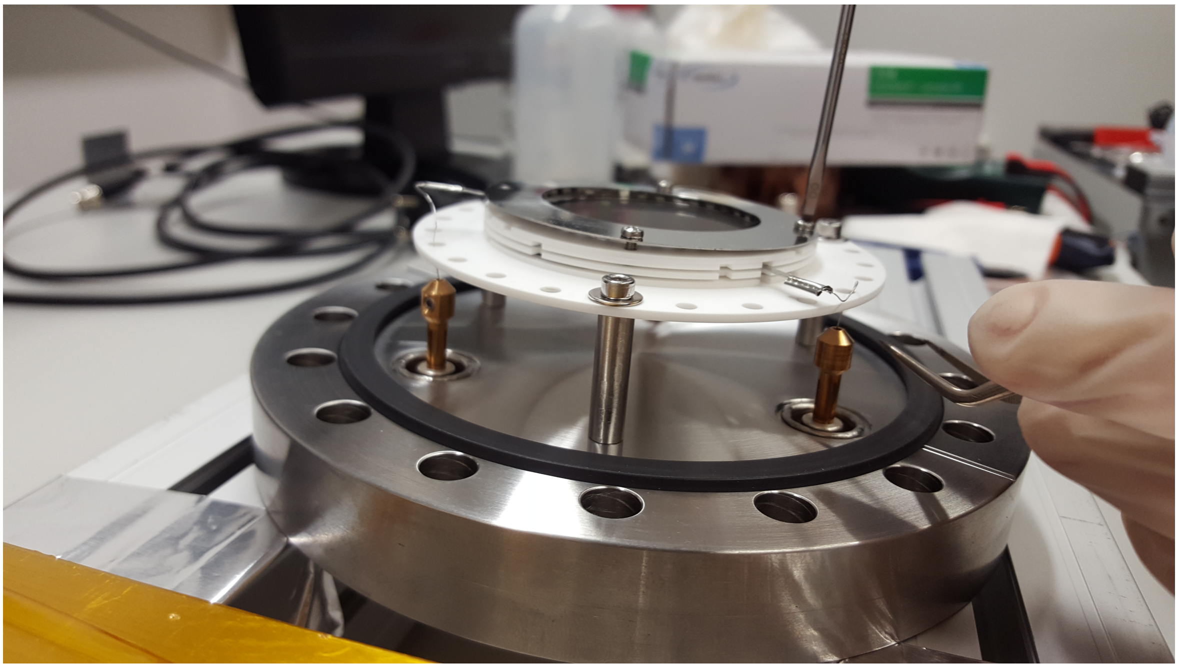

Figure 5.5: MCP detector mounted on a flange.

The channels have a length of $(480 \pm 5)\,\mu\text{m}$ and a pore diameter of $10\,\mu\text{m}$. Moreover the detector is made in chevron stack meaning that two single MCPs are behind each but rotated to $180\,^{\circ}$ against each other to achieve higher amplification factors (for further information see 4.3.1). Each single MCP can generate a gain factor g of $g \geq 2 \cdot 10^4$ depending on the bias voltage.

As described above in section 4.3.1 the electrons entering the MCP detector are causing an avalanche of electrons because of secondary electron emission in the channels. All the secondary electrons then get onto an anode leading to a voltage drop which can be read out as a signal for example by an oscilloscope like in figure 5.6. Those signals are in the time range of about 20 ns. To make automated measurements this signal

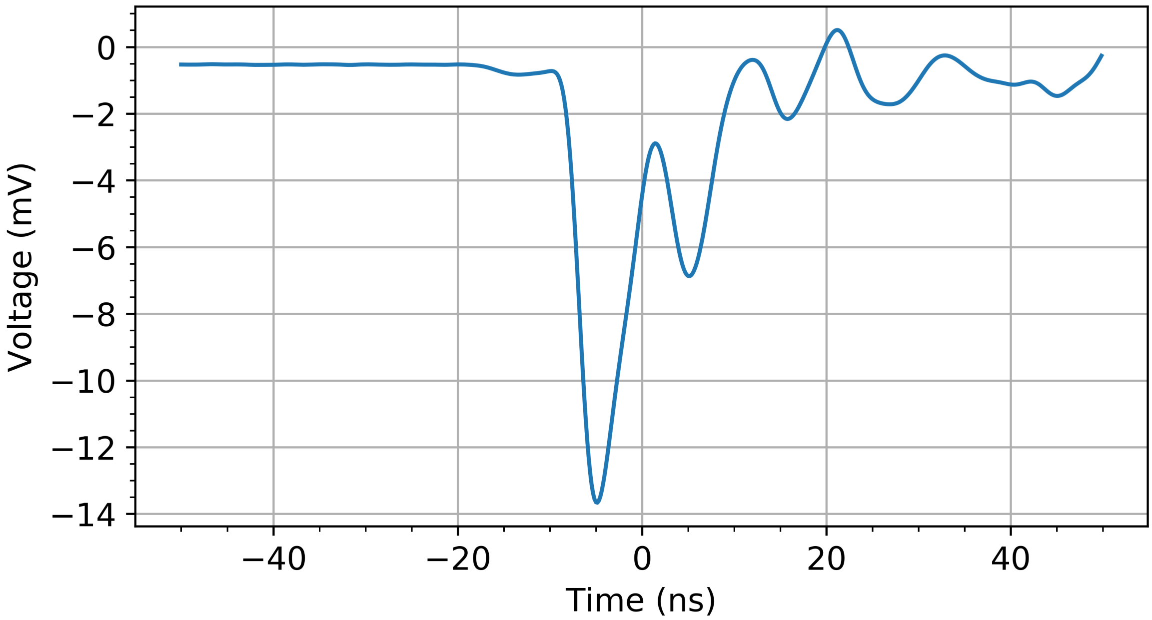

Figure 5.6: Pulse of an MCP signal recorded with an Oscilloscope. The signal shown here is averaged over 400 signals to smoothen the curve. A typical signal occurs in a time of about 20 ns.

from the anode is at first amplified by an amplifier (474 Timing Filter Amplifier by ORTEC) to a factor 20 and then put into a discriminator (Mod. N417 by CAEN) that provides a digital signal when the signal coming in is above a certain threshold that was set. The digital signal is then lead into a USB-device (NI USB-6008) which can be read out by a LabView program developed for these purposes. The chain of signals is visualized in figure 5.7.

Additional to measuring the count rates of the electrons a measurement of the am-

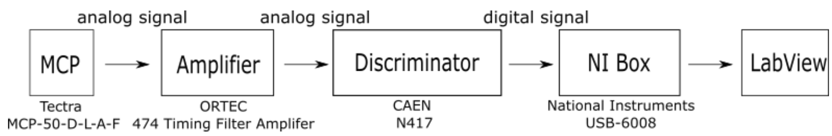

Figure 5.7: Chain of signals from electrons entering the MCP until registering of the count rate above a certain threshold at the Computer with the LabView program.

plitude spectrum can be recorded. This uses the signals of the anode too which gets amplified as well. The amplified signal is then put into a multi channel analyzer (CAEN N957 MCA) that analyzes the height of each pulse. These heights are then recorded by a PC with the program mca-recorder, written by Benedikt Bieringer [53]. A chain of signals for this kind of measurements is given in 5.8. The amplitude spectra are not giving information of the real energy of the electrons but can hint to where the first interaction of the initial electron with the inner channel walls of the MCP took place. This means that low channel numbers imply that low amplification inside the MCP detector has occurred. Vice versa this means that high channel numbers are occurred because of early interaction of the initial electrons with the inner channel walls of the MCP detector.

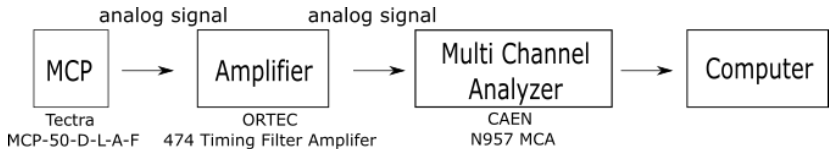

Figure 5.8: Chain of signals from electrons entering the MCP until getting the MCA amplitude spectrum.

The standard setting for measurements of count rates read with the discriminator is at a voltage of 1852 V instead of the normal setting of 2000 V to adjust the threshold. The lowered voltage causes that the electrons entering the channels of the MCP have to hit the inner channel walls in the front region which is more likely for electrons entering with a large angle. Otherwise the secondary electron emission is not high enough so that the signal at the anode would be too low to overcome the threshold at the discriminator. In principle also the threshold at the discriminator could be adjusted so that the MCP could be used at nominal voltage of 2000 V but the threshold of the discriminator is already set to the upper limit. The voltage of 1852 V is used because one can empirically measure that for this voltage under normal, not fine tuned conditions, only about half the electron rate is counted at the detector. As one knows that the secondary electron emission is exponentially rising, electrons with a small angle, meaning that they are hitting more likely in the back region of the channels, will be highly suppressed. This behavior is to be investigated.

5.4 Magnetic steering of the beam at the detector

The guidance of the electrons by the magnetic fields of the BTCs and with the air coils are already described but additionally to the standard test setup there are installed deflection coils at the detector site.

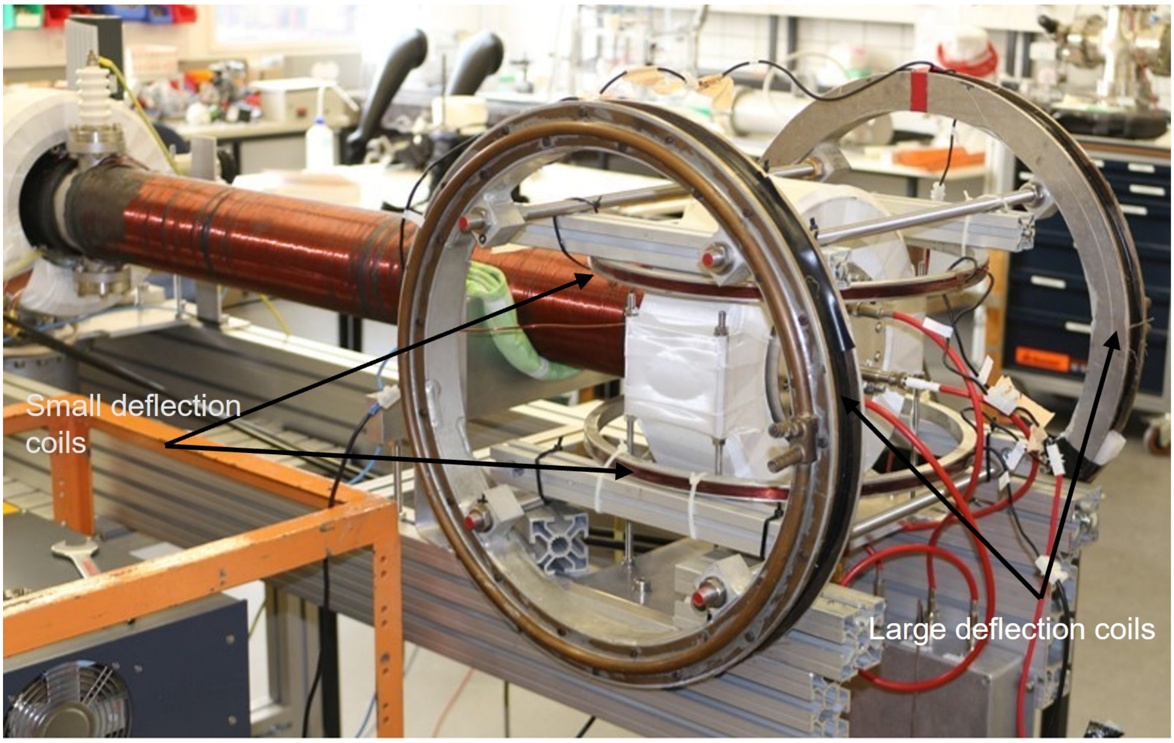

Figure 5.9: Deflection coils. The pairs of deflection coils are parallel to each other and have their center at the center position of the MCP detector. However the large deflection coils are perpendicular to the small deflection coils to be able to deflect the magnetic field line in every direction independently.

For being able to deflect the electron beam there has been installed a pair of air coils deflecting horizontally and a pair of air coils perpendicular to deflect vertically. Each deflection coil pairs are connected to each other in a series so there is the same current through them. These can be seen in figure 5.9.
The plane that is parallel to both coils in each deflection coil pair setting and cutting them in the middle is aligned with the z-axis, only the rotation symmetric axis is not exactly in the detector plane due to lack of space.

The deflection coils deflecting horizontally are not equally sized as the ones deflecting vertically. Due to their different size, windings and resistances the maximum current is different between the large deflection coils and the small deflection coils. The large deflection coils can be commissioned with up to 4 A whereas the small deflection coils can be commissioned up to about 10 A.
To deflect the magnetic field lines in every azimuth direction, so completely around the z-axis one has to change the polarity of the voltage accordingly at the power supply.
To make automated measurements the current through each deflection coils can be controlled with a LabView program.

6 Angular selective electron detection

In this section the measurements with the test setup to prove the angular filtering and detection of electrons are presented and preparatory measurements and alignments are shown.

For all the measurements the following parameters are held constant:

The amplitude spectra of the electron energies are recorded with an MCP voltage of 2 kV in combination with a multichannel analyzer whereas the other measurements of the count rate above a certain threshold are done at a lowered voltage of 1852 V. The pulse generator for emitting electrons at the eGun always generates rectangular pulses with the same frequency of $f = 50\,\text{kHz}$, a width of $t = 100\,\text{ns}$ and an amplitude of $U_{\text{pulse}} = 8\,\text{V}$. The vacuum in the test setup is constantly in a region of $p = 3\cdot 10^{-7}\,\text{mbar}$.

6.1 Angular alignment of eGun & long term stability

Before one can do reasonable investigations with the setup one has to be sure that the plate angle alignment of the eGun is calibrated correctly within the LabView program where the plate angles are shown and can be set (for further information see 5.2). The eGun plate angle is read out by attocube motors (Attocube ANR240) using piezo elements with an uncertainty of $\pm 0.01°$. However, since the attocubes do not read the absolute angle an offset has to be determined beforehand.

In order to investigate this offset an optical measurement is done. Therefore, direct sight on the eGun plates is required from the detector side so the detector was unmounted. Then, a self leveling cross line laser is placed in the BT2 axis in front of the BT2 flange and to the position where the laser would cut the BT2 in halves horizontally and vertically. It was ensured that the cross is centered in BT2 by centering both the horizontal and the vertical laser profile at the flange. After this adjustment a cross hair screen is mounted parallel to the flange between the BT2 and the laser with cross shaped profile to the position where the laser shines through the oblong holes in vertical (b) and horizontal (a) direction marked in figure 6.1.

Then the alignment of the eGun was performed by using a laser pointer shining through a hole in the cross hair onto the eGun front plate. The front plate is electrically polished so it reflects light sufficiently good. The reflected laser beam shines back on the cross hair. The distance Δr between the reflected beam spot and the hole in the

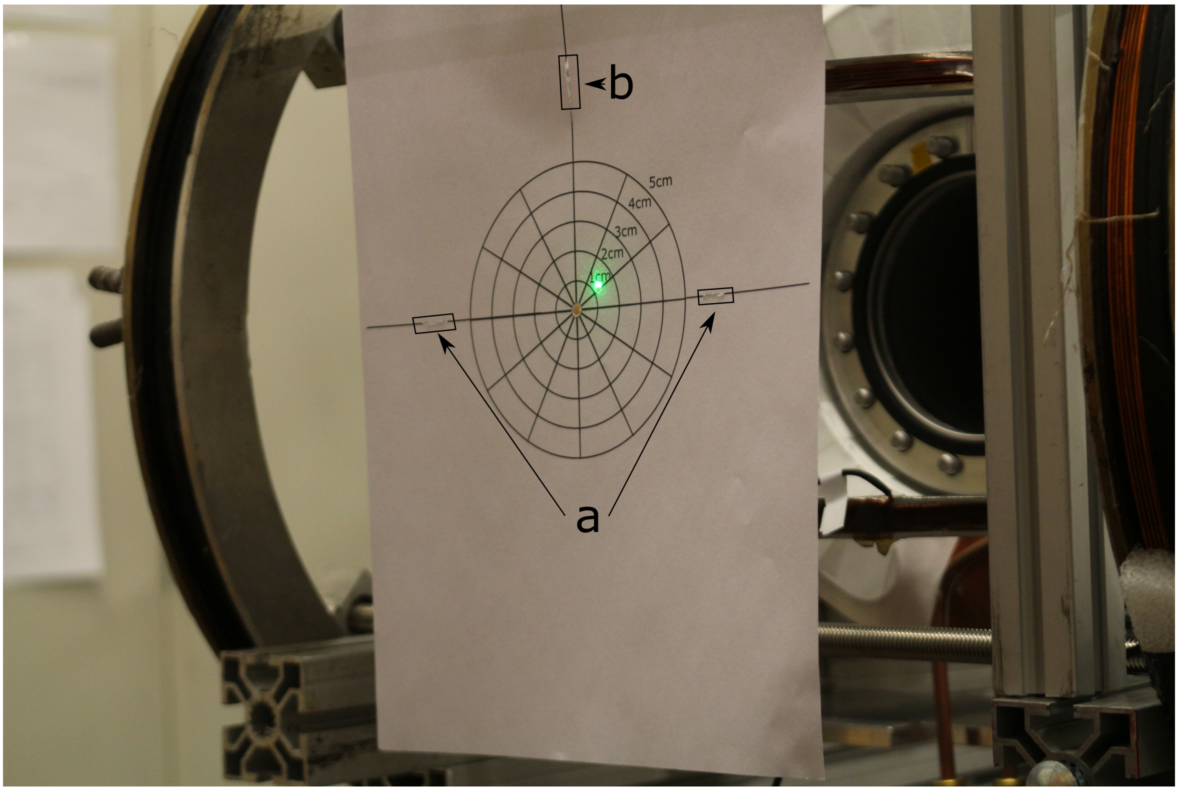

Figure 6.1: Cross hair screen in front of the flange on the detector side. This is used to align the eGun optically by considering the difference in position of the laser shining through the cross hair screen in comparison to the position of the reflected laser beam on the cross hair screen.

screen indicates an angle offset of the eGun. The measurement scheme is described in figure 6.2. The residual polar angle α_p of the eGun can be calculated by

$$\alpha_p = 0.5 \cdot \arctan\left(\frac{\Delta r}{d}\right), \tag{36}$$

where $d = 2884\,\mathrm{mm}$ is the distance between the cross hair screen and the front plate. The laser is set to shine off-center on the front plate because in the center there is the aperture where the electrons normally are guided through. The laser beam would therefore not be reflected by the electropolished surface, but by the copper coating, which does not reflect as well. Since one can orientate well at the technical drawing for the front plate the spot through which the laser shines on the cross hair screen and where it is reflected at the front plate is adapted. The hole in the cross hair where the laser shines through is applied off-center but set to the projection of the chosen spot on the front plate which is in polar coordinates at $r = 1\,\mathrm{cm}$ and $\theta = 60\,°$ being in the center between the aperture and the screw.

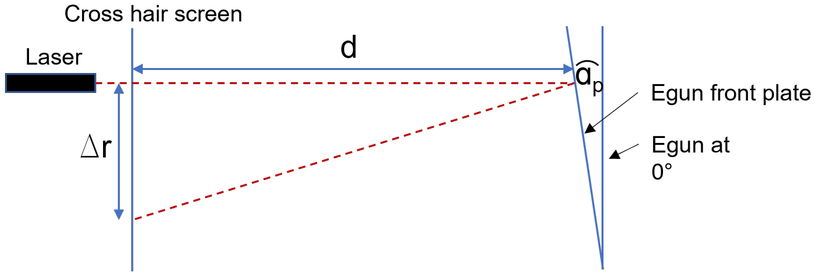

Figure 6.2: Illustration of the plate angle measurement. The distance Δr is describing the deviation from the laser beam shining through the screen to the position of the reflected laser beam on the screen. The eGun plate angle α_p can then be calculated by formula 36.

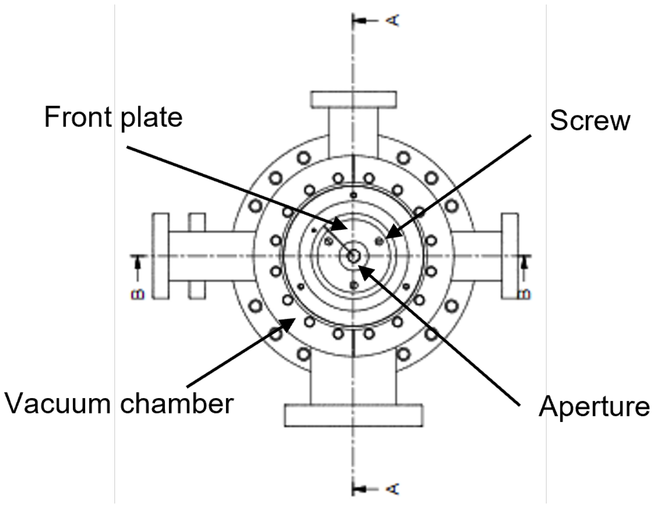

Figure 6.3: eGun scheme [51]. The front plate has a little aperture in the center and is held by three screws. The eGun is surrounded by a grounded cage which itself is surrounded by the vacuum chamber.

To achieve the 0°-setting the eGun needs to be horizontally and vertically tilted to minimize the distance Δr on the screen. The polar angle of the eGun is perfectly adjusted to $\alpha_p = 0\,°$ when $\Delta r = 0\,\mathrm{mm}$ but there is some uncertainty given for the position of the reflected laser beam on the cross hair screen of about $u_{\Delta r} = 0.5\,\mathrm{cm}$ leading to an uncertainty in angle of about $u_{\alpha_p} = 0.1\,°$. The measured attocube motor offsets are then used for the calibration of polar and azimuth angle in the LabView program. The former offset values of $axis1_{\mathrm{old}} = -163.41\,°$ and $axis2_{\mathrm{old}} = 75.14\,°$ were corrected to new offset values of $axis1_{\mathrm{new}} = -162.85\,°$ and $axis2_{\mathrm{new}} = 76.64\,°$.

In addition to the knowledge of the angle, another important characteristic is the stability of the eGun electron emission rate. Therefore a long term measurement with the eGun is done with 5 keV electron energies. This can be seen in figure 6.4.

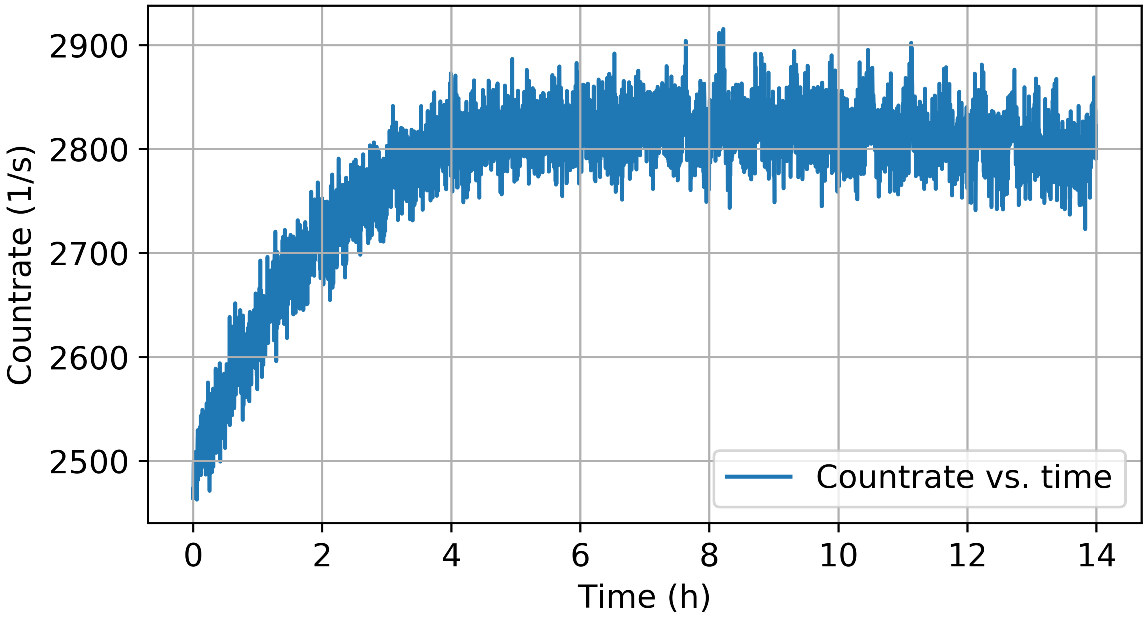

Figure 6.4: Long term measurement of the count rate of electrons when all parameters are held constant. Although the time to reach a nearly constant count rate is only given after about 5 hours the deviation in count rate is only in a range of about 10 %. Thus measurements are already reasonable before reaching the nearly constant count rate.

There one can see that the count rate is not constant over long time ranges but when considering time ranges of several hours it can be interpreted as relatively stable as the deviation is in the order of 10 % so that investigations with this setup are reasonable. For this and following measurements the standard magnetic field setting described in table 3 is used if not mentioned otherwise.

Table 3: Standard setting for currents through the coils for the measurements.

	BTC1	BTC2	eGun coil	Center 1 coil	Center 2 coil	Detector coil
Current (A)	6.7	6.7	20	20	20	19

6.2 Measurements with MCP filter

To achieve the best results for measurements, the angular spread of electrons is needed to be as small as possible. Previously done measurements to characterize the eGun showed that there is always some angular spread [52]. In order to reduce it a physical filter based on a passive (not put under voltage) MCP is installed to only let through a very narrow angular distribution of electrons. The best filtering effect by the MCP is reached when the channels of the MCP are aligned with 0° to the magnetic field lines, which is, in a homogeneous field, synonymous with being aligned with the beam axis.

To achieve this a piece of an MCP (from now on called MCP filter) has been investigated with a microscope to look for the direction the channels are facing to. This has been done by using a device which makes it possible to rotate and to tilt the MCP filter as visible in figure 6.5. The rotation point for tilting the upper plate is visible on the bottom right side of this figure made by a sphere between both plates. One micrometer screw is fixed and with the other micrometer screw one can then very precisely change the height of one edge resulting in a tilt angle. Additionally, there is in the middle of the upper plate a table for rotation.

With the help of a microscope in transmission mode the channels can be seen. For

Figure 6.5: Device for investigating the tilt angle of the MCP filter.

different tilt angles the rotation angle is varied and photographed in 10 $^\circ$ steps. The brightness is determined via the number of saturated pixels in each image. The brightest image of the measurement series determines the MCP bias angle. Further the geometric shapes also hints to the actual MCP bias angle: A circular shape of the MCP channels indicates a well alignment of the channels whereas this is not the case when the channels seem to be elliptic. The best fitting bias angle of 5.1 $^\circ$ with different rotation angles can be seen in figure 6.6. From this measurement series one can estimate that the best approximation of the channels with a circle is described by 6.6b.

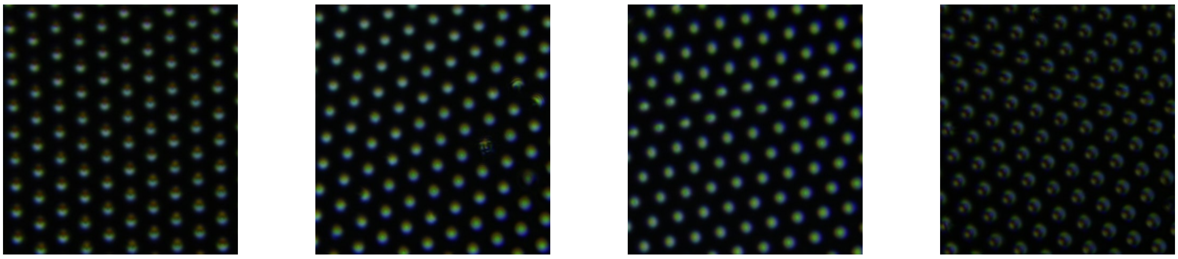

(a) 0 ° rotation. (b) 10 ° rotation. (c) 20 ° rotation. (d) 50 ° rotation.

Figure 6.6: A part of the MCP filter is investigated with the help of a microscope. The MCP filter is tilted to 5.1 ° and then rotated with the device in figure 6.5 by different angles. The angle of rotation at which the shape of the channels of the MCP filter most resembles a circle is used for installation in the test setup. Pictures and analysis by Kevin Gauda.

Then the MCP filter is mounted on a holding structure made of copper and installed with the measured bias angle of 5.1 ° that is spanned between the normal of the MCP filter and the beam-axis on a linear feed-through visible in figure 6.7 behind the cube at BT2. First measurements of the count rate with electron energies of 5 keV showed that there was no transmission through the MCP filter. Thus, it was needed to check whether an eGun plate configuration exists that allow for electrons to be transmitted through the filter. A LabView program was written to automatically vary the polar and azimuth angle to scan in a chosen parameter space the count rate determining the transmission through the MCP filter. Results of this measurement are visible in figure 6.8a. The polar angle in this case describes the angle between the z-axis and the normal of the eGun plates whereas the azimuth angle describes the rotation around the z-axis. For a good alignment of the MCP filter in combination with a homogeneous magnetic field at the position of the MCP filter the expectation would be that the azimuth angle is irrelevant so that the transmission through the MCP filter only depends on the polar angle. Whereas for a not correctly aligned MCP filter or a misalignment of the magnetic fields the azimuth angle can play an additional role as then the orientation of the channels is not parallel to the magnetic field lines. The eGun angle to achieve maximum transmission has been determined to 1.5 ° in polar angle and 300 ° in azimuth angle. The 2D plot in figure 6.8a shows that the azimuth angle has a larger effect on the transmission through the MCP filter than the polar angle. Thus it shows that either the magnetic field is not homogeneous in this place or the channels of the MCP filter were not exactly aligned with respect to the optical beam tube center and that even small deviations can cause significant effects.
Despite being in maximum transmission this still means a reduction of count rate to about 5% when comparing it to the case of no MCP filter in the beam line.

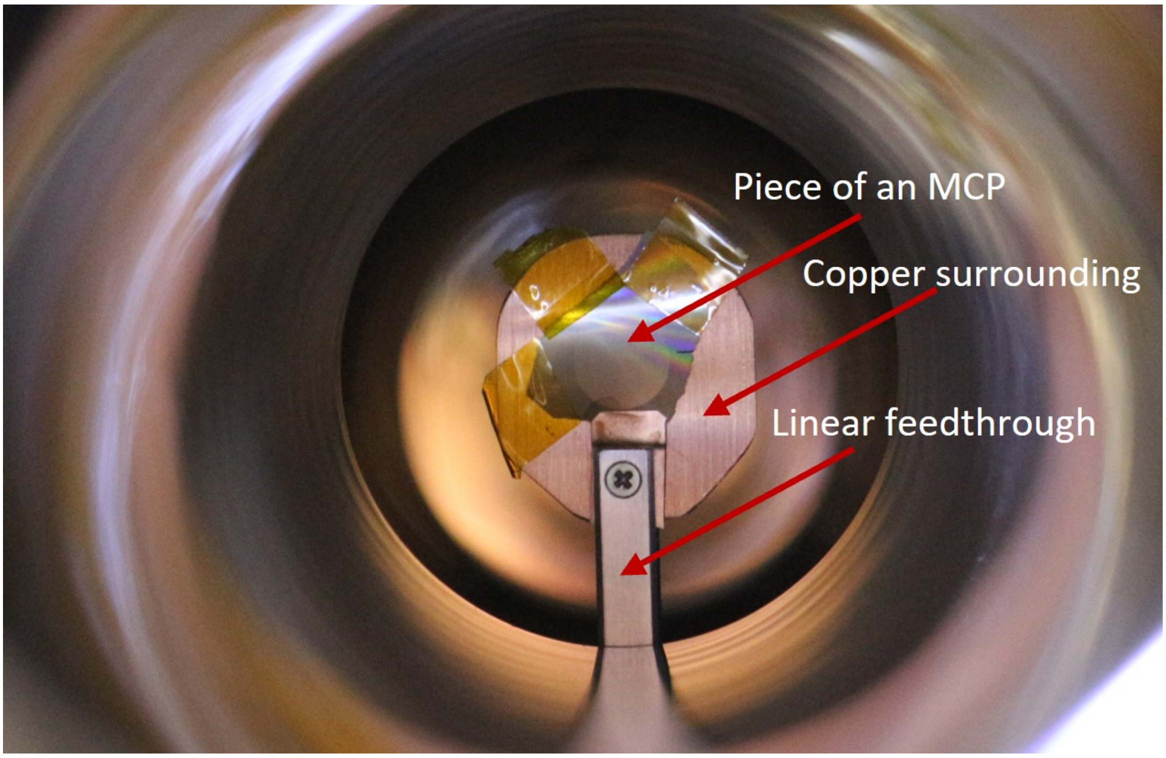

Figure 6.7: Piece of an MCP as a filter for electrons with small polar angles placed in the beamline. The piece of an MCP is attached to a copper surrounding on a linear feedthrough. One can see that the channels of the MCP are approximately parallel to the beamline as it seems to be transparent. The uncertainty can be estimated to be $\alpha = \arctan\left(\frac{d}{l}\right) \approx 1.14\,^\circ$ by inserting a channel diameter of $d = 10\,\mu$m and a channel length of $l = 500\,\mu$m

In the configuration of maximum transmission through the filter it is tested whether the electron detection shows angular dependence. The deflection coils are used to deflect the central magnetic field line at the MCP detector to $6\,^\circ$ that is defining $100\,\%$ deflection. A deflection of $6\,^\circ$ is used because this is the bias angle of the MCP detector according to the manual so for a deflection of $6\,^\circ$ the electrons should enter the channels of the MCP detector parallel to the channel orientation. If the beam is actually filtered and stripped of non-suitable electron angles then the detected count rate should be highly suppressed. The needed currents through the deflection coils have been calculated with the help of a simulation software called Bfield_3D where one can insert the coils with their parameters (positions, length, thickness, radii, windings, currents, orientations) to obtain the magnetic field lines [54]. The angle between the central magnetic field line and the z-axis at the z-position of the detector yields an estimation of the angle of deflection. To get to $6\,^\circ$ deflection the angle has been calculated for different currents at each deflection coil until the best fitting current was determined. This calculation is done by Kevin Gauda. An example of the simulation

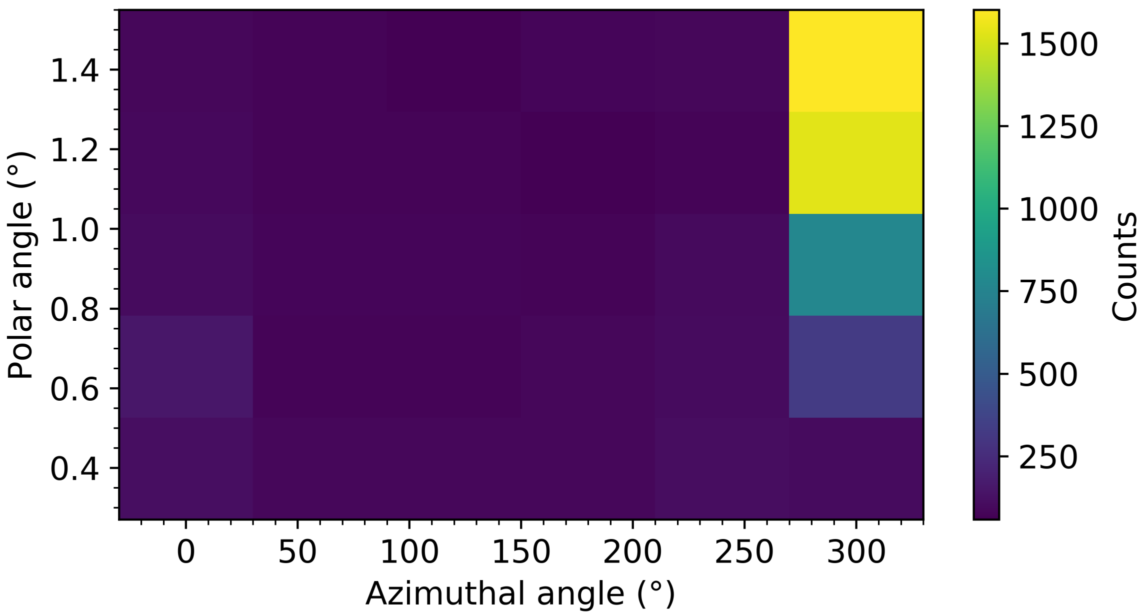

(a) Measurement of the transmission through the MCP filter by varying the polar and azimuth angle of the eGun.

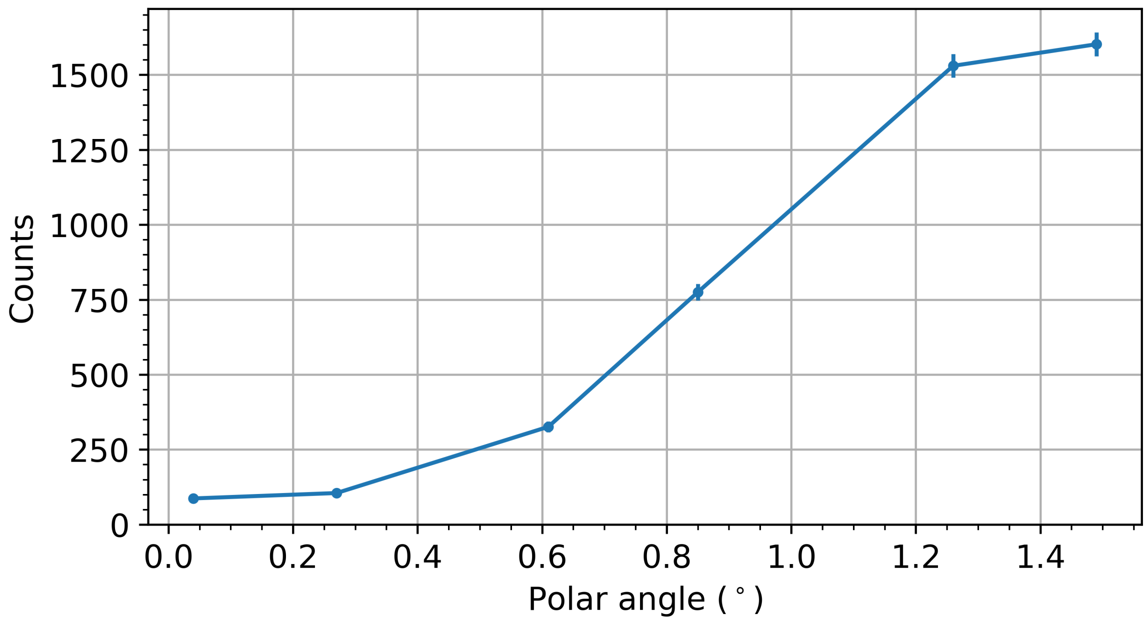

(b) Plot of the case with 300 ° azimuth angle for different polar angles. One can see that the maximum transmission is obtained in the region of nearly constant counts between 1.2 ° and 1.5 °.

Figure 6.8: Variation of the eGun in polar and azimuth angle to pass through the MCP filter. The electrons have an energies of 5 keV.

with Bfield_3D can be seen in figure 6.9.

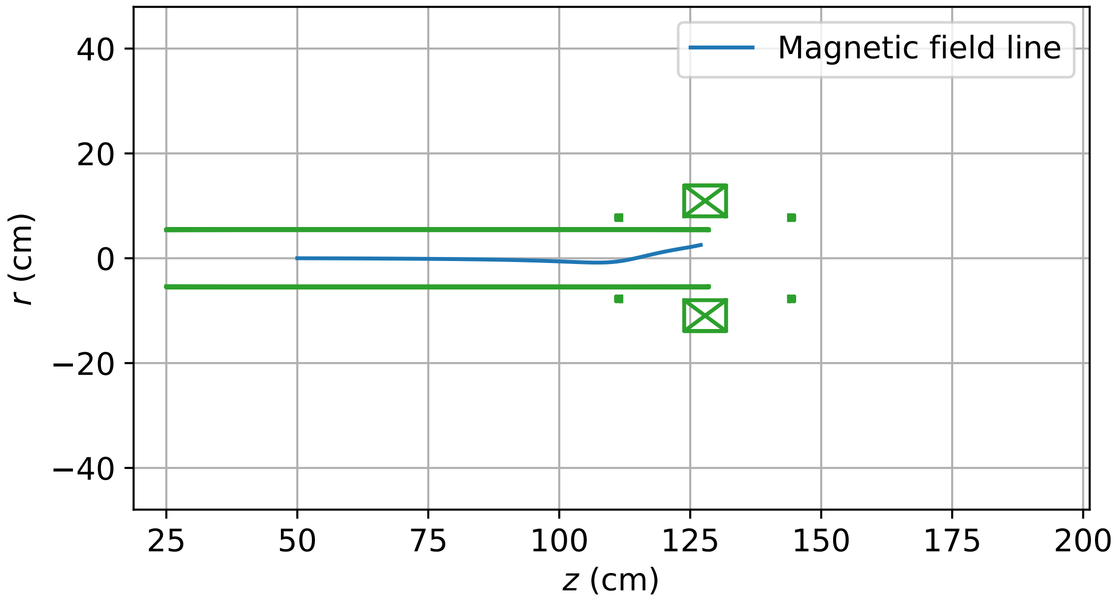

Figure 6.9: Simulation of the magnetic field line with Bfield_3D. The parallel green lines starting at 25 cm in z-position are illustrating the beam tube, the bigger rectangles the detector coil and the smaller rectangles the big deflection coils. Simulation by Kevin Gauda.

Here one has to take into account, that the magnetic field produced by the deflection coils are limited by the power supplies and that they are not actively cooled. Hence the deflection coils are heating up and can not hold a large current for a long period of time. This means that the magnetic field of the detector coil has to be rather small to be able to deflect the electron beam to 6 °.

But another important parameter for the MCP detector when examining the angular dependent electron detection is the direction in which the 6 ° polar angle is facing to. The deflection into horizontal direction is due to the larger deflection coils that are mounted laterally to the detector, while the vertical deflection is due to the smaller deflection coils that are mounted below and above the detector (see figure 5.9). This azimuth angle α can be calculated by the following relations for horizontal and vertical deflection: $I_{\text{horizontal}}(\alpha, r) = r \cdot I_{\text{horizontal},100} \cdot \cos(\alpha)$ and $I_{\text{vertical}}(\alpha, r) = r \cdot I_{\text{vertical},100} \cdot \sin(\alpha)$, where r is the percentage of the deflection to 6 ° and I_0 are the currents leading to 6 ° polar deflection when $r = 100\,\%$. Then a measurement of the count rate is done in which a quarter of a circle in azimuth angle is scanned with these relations and different r values leading to different polar angles. Only the one quarter was scanned, because only there was an angle-selective effect.

The results of this measurement are visible in figure 6.10a. There on can see that for 70 % deflection a drop in count rate is visible whereas this effect does not occur at lower or higher r values which means that this is a local effect.

This could be explained by the effect of lower amplification for electrons entering the channels of the MCP parallel so that the electrons are not causing a high amplification. Thus they would not be detected because of the too high threshold for triggering the event. This would be the principle to be exploited to suppress the Rydberg background. To verify that this is the effect the amplitude spectrum is measured with a multichannel analyzer for the deflection coil setting where the drop in rate occurred and for the deflection coil setting where the maximum rate is measured. It is expected that the amplitude spectrum would be shifted towards lower channel numbers because of smaller amplification factors when the electrons are flying parallel to the channels and do not hit the walls. This effect is clearly visible in figure 6.10b.
There are multiple possible explanations for the biggest drop in count rates at 70 % deflection instead of at 100 % deflection. It can be an additional indication that the MCP filter is not perfectly aligned so that there is some residual polar angle of the electrons left when they are passing the MCP filter and thus not the whole amount of deflection is needed. Another explanation could be that there is also some uncertainty of the channel bias angle of the MCP detector which is described as $6 \pm 1°$. If the bias angle would actually be $5\,°$ the necessary deflection angle would be reduced by 17 %. Additionally the magnetic field by the BTCs has some tilt angle to the z-axis because the copper wire is spiraling around the beam tube which can also imprint an additional deflection angle leading to a different necessary deflection angle produced by the deflection coils. This is further described in 5.1.
A reduction factor, defined by the maximum registered count rate divided by the minimum detected count rate, of 4.5 is achieved with this method. If the angular spread of the electrons is very small, the deflection coil setting that orientates the electrons parallel to the channels would reduce the measured count rate significantly. In this case all the electrons would only generate a signal in the second MCP plate of the MCP detector in chevron stack which would be too low to overcome the threshold. In contrast, if the angular spread were too large, one would not expect any reduction at all, since the angles would then be broadly distributed and at each deflection some electrons would have the right angle to pass the first MCP plate without interaction, but the vast majority of electrons would still hit the MCP plate in the front region and thus produce a signal. Obviously currently a state in between is reached. The aim of the investigations in the following chapters is to further improve the reduction

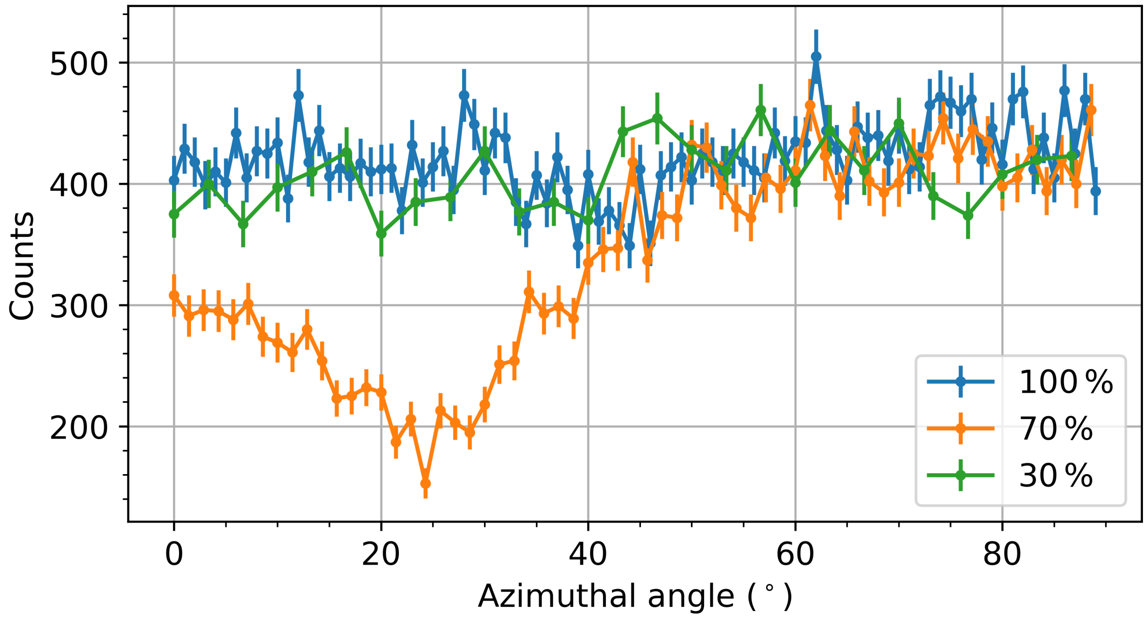

(a) Measurement of the count rate with inserted MCP filter and deflection coils used. 100 % means that the electron beam is deflected by 6 ° being the orientation of the channels of the MCP detector. A drop in count rate only occured for 70 % deflection.

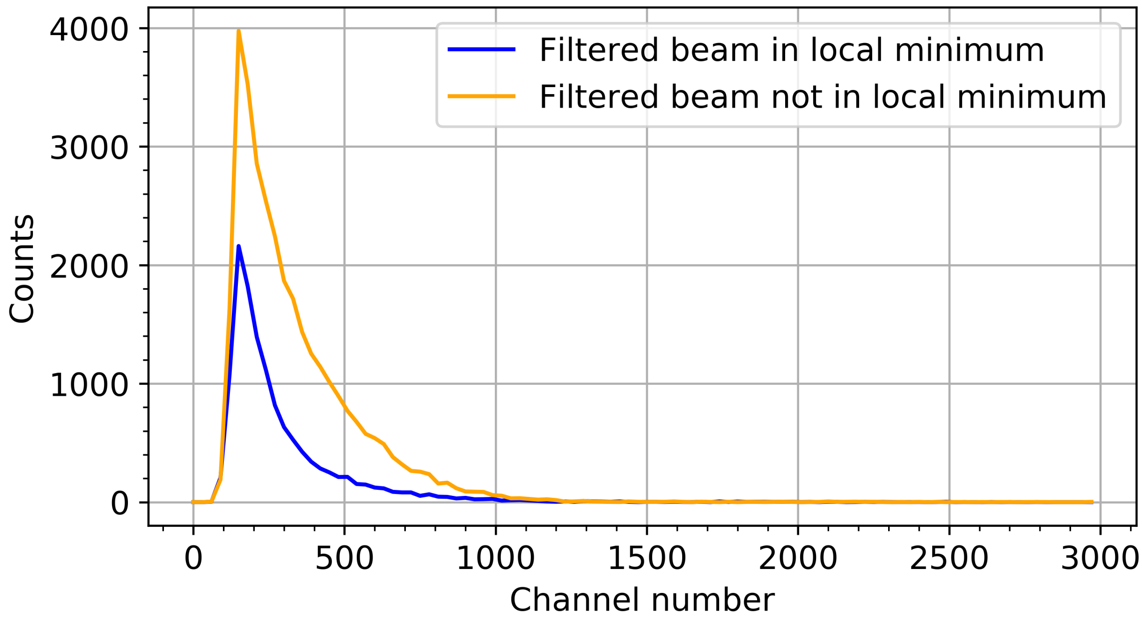

(b) MCA spectra for deflection of 70 %. One time in the minimum and one time outside of the minimum.

Figure 6.10: Measurements when the MCP filter was in the beamline and the deflection coils are used to deflect to different polar and azimuth angles.

factor to find the best-suited method to implement into KATRIN.

6.3 Cyclotron-phase dependent filtering and detection

Previous measurements showed that there is an angular dependent filtering by the MCP filter. This effect will be examined further.
A measurement where the current through the BTC1 is varied continuously while the MCP filter is inside the beamline shows that there is a strong dependence on the magnetic fields for the transmission probability through the MCP filter. So only within a small interval of currents there is a larger probability to pass the MCP filter. This can be seen in figure 6.11. The spikes are spaced in nearly equidistant intervals. This indicates that there is some periodical behavior of the electron which may be caused by the cyclotron motion. That hypothesis is confirmed by a calculation for the properties of the electrons and the magnetic field configuration: The expectation for currents

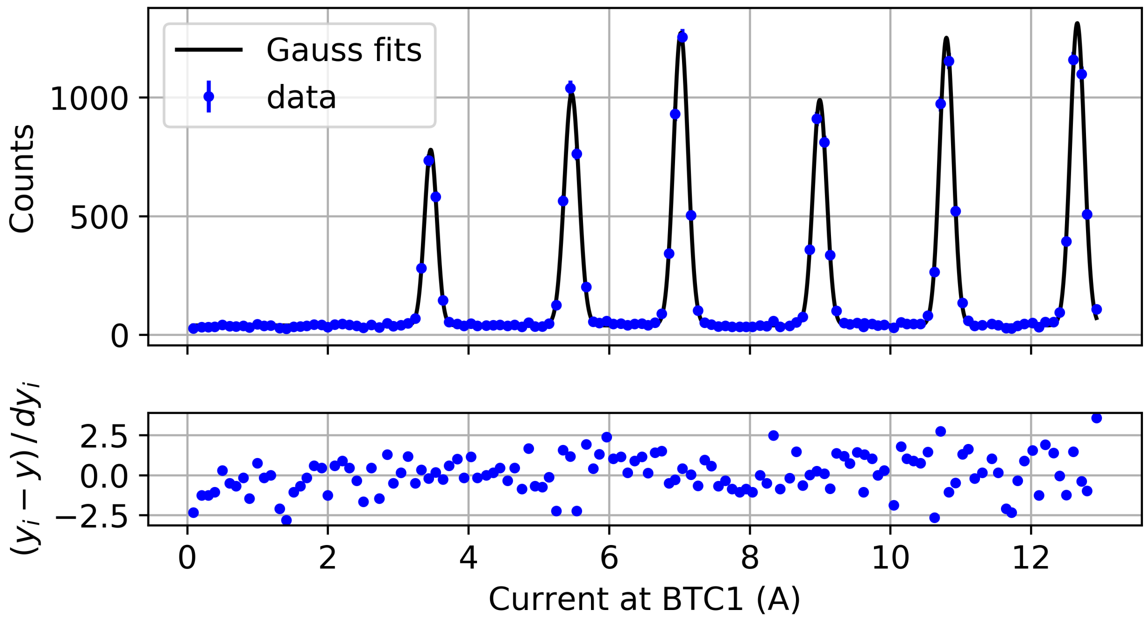

Figure 6.11: Measurement of the counts when the MCP filter is in the beamline and the BTC1 current is varied. The position of the spikes are at a current at BTC1 of ((3.4636 ± 0.0025) A, (5.4684 ± 0.0026) A, (7.0197 ± 0.0020) A, (8.9963 ± 0.0022) A, (10.7977 ± 0.0019) A, (12.6613 ± 0.0018) A).

through coils having the effect of adding one complete period of cyclotron motion can be calculated by using the frequency of cyclotron motion dependent on the magnetic field $B(I)$. A frequency can also be described as the ratio between a wavelength λ and the velocity in longitudinal direction $v_{\parallel}$.

$$f_{cyclotron} = \frac{e \cdot B(I)}{2\pi m_e} = \frac{v_{\parallel}}{\lambda} \tag{37}$$

The magnetic field of the BTCs is approximated as an infinitely long cylinder coil with the density of windings N per length l multiplied with the current I through it and the vacuum permeability μ_0:

$$B(I) \approx \mu_0 \frac{NI}{l}. \tag{38}$$

Combined one gets a current in dependency of the cyclotron wavelength

$$\Rightarrow I = \frac{2\pi m_e v_{\parallel} l}{e\mu_0 N} \cdot \frac{1}{\lambda}. \tag{39}$$

Furthermore the wavelength λ can be described as the ratio of the length l of the whole BTC and the periods n it took in the BTC:

$$l = n \cdot \lambda. \tag{40}$$

This can be inserted in equation 39 to get a dependency of the current for an amount of periods provoked by the BTC

$$\begin{aligned} \Rightarrow I &= \frac{2\pi m_e v_{\parallel}}{e\mu_0 N} \cdot n \\ \Rightarrow \Delta I &= \frac{2\pi m_e v_{\parallel}}{e\mu_0 N} \cdot \Delta n. \end{aligned} \tag{41}$$

The velocity $v_{\parallel} \approx v$ can be calculated by the total energy of the electron that is the sum of the rest energy E_0 and the energy gained by the acceleration voltage U at the eGun

$$E = e \cdot U + E_0. \tag{42}$$

For the total energy the energy-momentum equation

$$E^2 = c^2 p^2 + E_0^2 \tag{43}$$

can be used where p is the relativistic momentum. In addition there is the relation for momentum and total energy

$$cp = E \cdot \frac{v}{c} \tag{44}$$

which can be combined and rearranged to

$$v = c \cdot \sqrt{1 - \left(\frac{1}{1 + \frac{e \cdot U}{E_0}}\right)}. \tag{45}$$

The approximation of $v_{\|} \approx v$ is justified because only very small polar angles of the electrons are produced.
Since the equation 41 is linear in the amount of periods n it is always the same current between each full cyclotron period. So by setting $\Delta n = 1$ one gets $\Delta I = 2.24\,\mathrm{A}$ for $N = 532.5$ windings of the coil and an acceleration voltage $U = 5\,\mathrm{kV}$.
The difference in currents for one additional cyclotron period caused by the BTC is for 5 keV electrons, according to the measurement in figure 6.11, $\Delta I = (1.84 \pm 0.16)\,\mathrm{A}$ which is not in the range of uncertainties.
However, there is for example the magnetic field of the BTCs that is slightly tilted because of the copper wire spiraling around the BT as explained in 5.1. Moreover the longitudinal energy has been approximated to be the whole kinetic energy as well as the beam tube to be infinitely long. Additionally, there can be some other unknown systematics.
However, electrons can only have a phase in cyclotron motion when they are not emitted with $0\,^\circ$ angle to the magnetic field line. The cyclotron phase-dependency should also be present at the detector MCP. Therefore the MCP filter is removed and the effect of the cyclotron phase at the MCP detector is investigated by varying the current through the BTC1 and measuring the count rate. The measurement result of it can be seen in figure 6.12. This measurement shows similarities to the previous measurement with the spikes as there are also periodical dependencies with about the same distance in currents at the BTC1. Additionally, one can see that it needs a certain current of about 2.3 A to guide all the electrons through the beam tube without loosing the electrons on the way through the BT1. Even without using the filtering of the MCP filter there is a strict behavior that for some magnetic fields there is a much lower count rate that is also nearly periodical with the same periodicity of about 2 A in current at BTC1. One can see that the dips in figure 6.12 as well as the spikes in figure 6.11 do not always have the same height. The rather small sampling rate can partly explain that behavior. Furthermore, in plot 6.12 is shown the difference in count rate for two MCP detector settings. The blue curve describes the registered count rate when the detector is at the nominal voltage of 2000 V whereas the orange curve describes the count rate for the setting of the MCP at 1852 V. These settings are chosen for the following reason: 2000 V is the nominal setting suggested by the

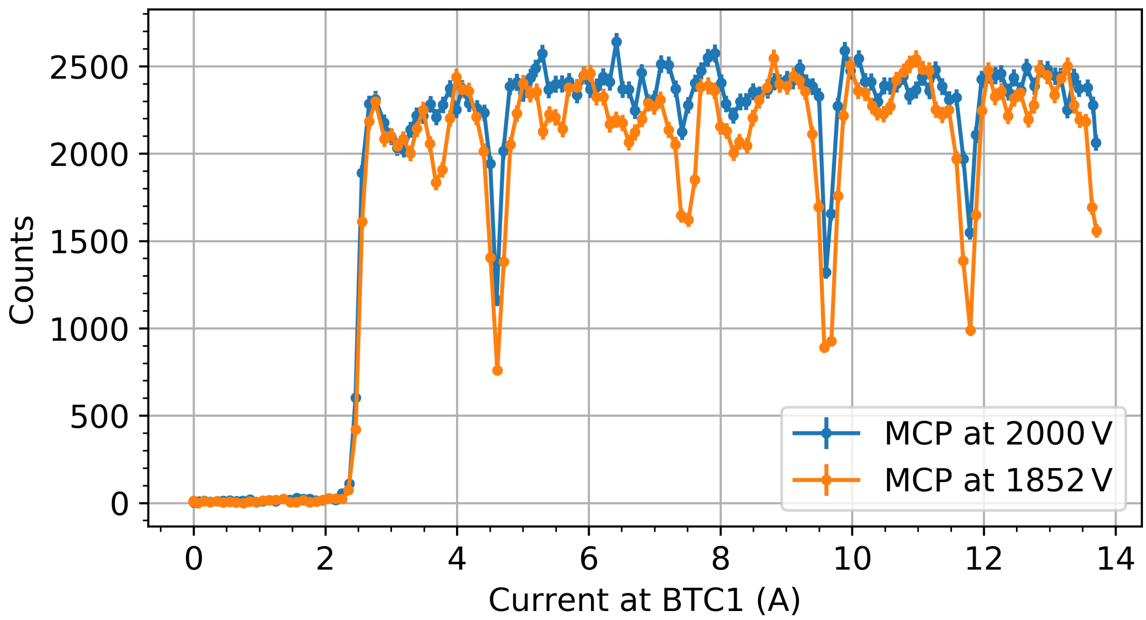

Figure 6.12: Measurement of the count rate of electrons when the MCP filter is not in the beamline and the BTC1 is varied. This is done for an MCP voltage of 2000 V and for 1852 V. One can see that the local minima are getting deeper for a lowered voltage.

manufacturer. The measured rate at 1852 V in a setting without phase dependent rate suppression (e.g. at 6 A in figure 6.12), is halved. Therefore the registered rate in the 1852 V setting is multiplied by the factor 2 to be normed. Electrons that penetrate deeper into the channels without interaction are registered less often due to the lower amplification in combination with the constant threshold. This can also be seen in figure 6.12 as the local minima are always deeper for the lowered MCP voltage whereas for the case between the local minima the normed count rate is approximately the same for both MCP voltages. So this setting makes the effect of angular selective electron detection more visible which is why this is the standard setting for later measurements for the MCP detector.

Further, the influence of the detector coil current on the count rate was examined. The larger magnetic field of the detector coil increases the electron angles, which changes the cyclotron phase similarly as before. Moreover, due to the overall increased electron angles at the detector depending on the detector coil current an effect on the count rate is expected. This investigation is done by varying independently the BTC1 current as well as the detector coil current. The count rate is shown in a color-coded 2d histogram seen in figure 6.13. The standard magnetic field setting changed for this and further measurements according to table 4 because of the longer measurement

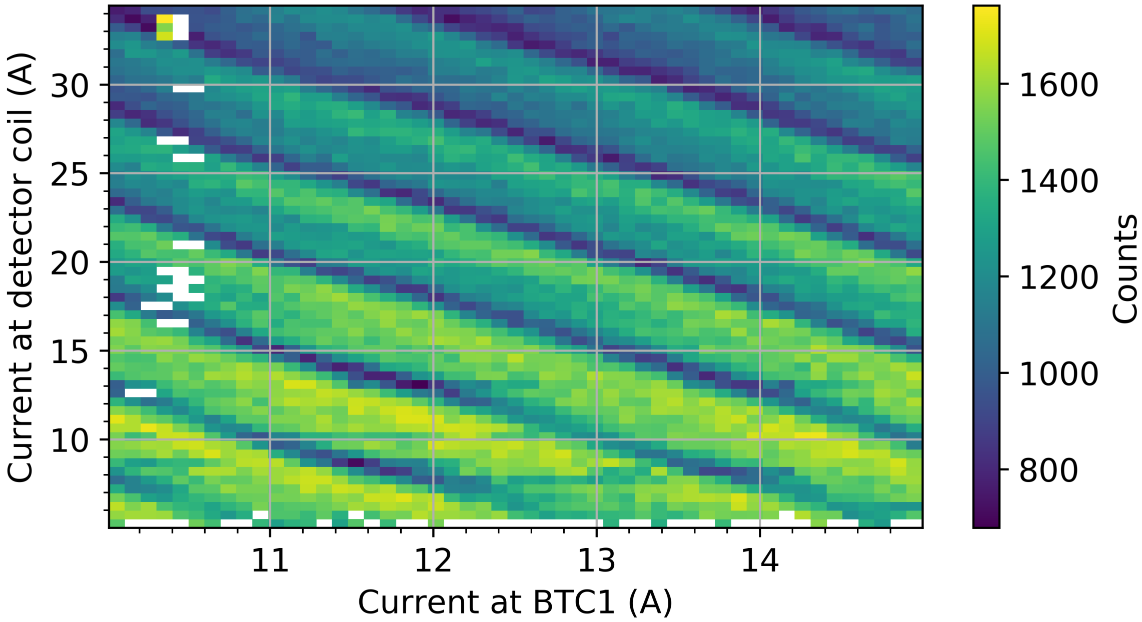

Figure 6.13: Measurement of the count rate of electrons when the current through BTC1 and independently the current through the detector coil is varied. Here one can see nearly parallel diagonal lines with lower count rate indicating a periodic behavior.

times during which the air coils are heating up significantly, although they are actively water-cooled, resulting in a larger resistance and therefore the current can not be held by the used power supplies.

Table 4: Costumized standard setting for currents through the coils exchanging the previous one declared in 3 due to longer measurements.

	BTC1	BTC2	eGun coil	Center 1 coil	Center 2 coil	Detector coil
Current (A)	8	8	19	19	19	19

The results of this measurement show that there is once more the periodic distance in horizontal direction of about 2 A between the minima corresponding to the cyclotron motion. Furthermore, one can see that also in vertical direction there is some periodical dependence in a distance of about 5 A. The periodicity caused by the detector coil in cyclotron motion can also be estimated with the equation 41 above by inserting 382 windings to about $\Delta I = 3.1\,\mathrm{A}$. Due to the fact that the electrons are only influenced by the magnetic field in front of the detector and not behind it only half of the effect on the cyclotron phase is applied. Therefore the periodicity has to be multiplied by the factor of two to $\Delta I = 6.2\,\mathrm{A}$. This estimation is also not perfect but due to their small aspect ratio the approximation as an infinitely long coil gets even worse than for the longer beam tube coils and thus it is only a rough estimation. One can also see that for higher detector coil currents there are detected less events. The expectation was the other way around because due to the increased polar angles the electrons would gain a higher probability to hit the channel walls in the front region. But for too high polar angles there is also the possibility that the electrons do not cause secondary electron emission but absorption in the walls. However, the polar angle is not the only parameter describing the probability to hit the channel walls. So a counter effect could be that the cyclotron radii get smaller for higher magnetic fields at the detector so that the electrons get a lower probability to hit the channel in the front region. Additionally, it could have some detector effects that the secondary electrons generated by the incoming electrons are not guided properly to the anode caused by strong magnetic fields.

The knowledge that there are angular effects in dependence of the phase in cyclotron motion at the detector seen in figure 6.13, 6.11 and 6.12 gave the reason to investigate it further. When comparing the spikes measurement in figure 6.11 with the measurement in figure 6.12 one can see that the spikes caused by the MCP filter and the dips at the detector do not overlap when using the same magnetic setup. Thus, a measurement is done in which both BTCs are varied separately to determine a dependence between both BTCs with which the electrons can always pass through the MCP filter. This measurement is plotted in figure 6.14. One can see that there is an approximately linear dependence between the two BTCs as expected because of the superposition principle for magnetic fields and the linear dependence of the current for the magnetic fields. The data are actually described slightly better by a cubic polynomial which might come from temperature or time dependent effects in the setup. The fit can be seen in figure 6.15 and the fitting parameters in its caption.

With the known dependency one can now vary the phase in cyclotron motion continuously while electrons are still passing the MCP filter. It was expected that the angular distribution of electrons would be more narrow than without the filter, because electrons with large angles at the MCP filter would not be transmitted. With this smaller angular distribution it should be possible to deepen the dips seen in figure 6.12. A measurement is performed to examine the expectation and the results are plotted in figure 6.16. The expectation was a plot similar to figure 6.13 but with smaller periodicity due to not only varying BTC1 but also BTC2. However, no obvious pattern is visible. This can be due to a too low resolution of the power supplies that have a

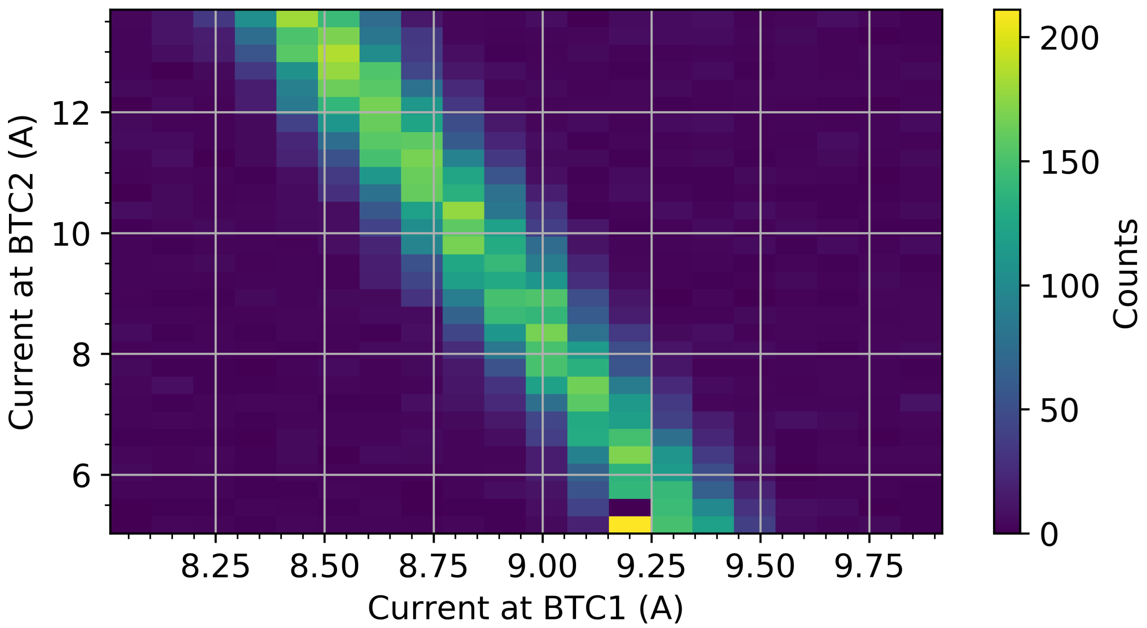

Figure 6.14: In this measurement the BTC1 and the BTC2 are varied separately and the count rate is measured to determine a dependency between the two BTCs in which the electrons can pass through the MCP filter.

standard deviation of 0.05 A, because when varying the BTC1 by 0.1 A then BTC2 is already varied by about 1 A which is rather near to a hole cyclotron period being at (1.84 ± 0.16) A. Also, the electrons that are not absorbed might be scattered within the MCP filter channels and still leave the filter. That would result in a broader than expected angular distribution. That is why this idea is not pursued further.

6.4 Angular filtering with tilted MCP detector

To eliminate the cyclotron phase dependency and to get lower polar angles of the electrons the energy of the electrons is reduced to 50 eV and the eGun coil is placed closer to the eGun. This is done because the principle of the eGun does not work properly for the combination of low electron energies and high magnetic fields because of the lower electric field between the back plate and the front plate, which leads to less non-adiabatic motion according to equation 35. So only angles with a small deviation to 0° should be produced.

Furthermore, the MCP detector is installed in combination with a tilted flange. This flange is supposed to tilt back the channels so that these channels are aligned with the beam axis. The required deflection angle therefore becomes much smaller, so that the current through the deflection coils can be reduced. On the other hand, this allows for larger current through the detector coil while still being able to scan the region where

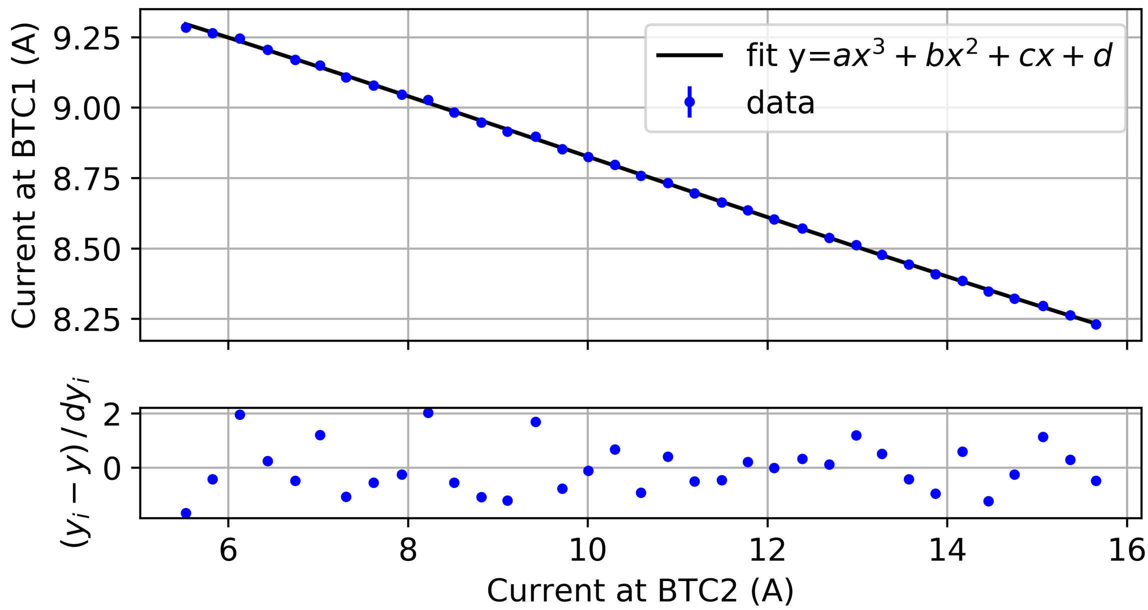

Figure 6.15: Fit with a cubic polynomial to describe the dependency between the BTC1 and BTC2 current to pass through the MCP filter according to 6.14. The data points are obtained by considering each current at the BTC1 and fitting a Gaussian distribution to the count rate in dependence of the current through BTC2. Thereby for each current at the BTC1 a current at the BTC2 can be assigned. The fit values of the cubic polynomial are $a = (0.11 \pm 0.004) \cdot 10^{-3}\,\mathrm{A}^{-2}$, $b = (-0.0034 \pm 0.0013)\,\mathrm{A}^{-1}$, $c = -0.073 \pm 0.013$, $d = (9.78 \pm 0.04)\,\mathrm{A}$. The goodness of the fit is described by $\frac{\chi^2}{\mathrm{ndf}} = \frac{29.01}{31} = 0.94 \pm 0.25$.

the incidence angle is close to the channels angles to the beam axis.

For this purpose one had to examine in which direction the channels are oriented. This has been done by disassembling the MCP detector that consists of two MCPs in chevron stack. The top MCP was removed and put into a holding structure made of PTFE. This holding structure is put on a rotatable table that allows to measure the rotation angle with an uncertainty of $0.4\,°$. As one can see at figure 6.17 on the right side of the MCP there is a light source and on the other side there is a photodiode which is connected to an oscilloscope. With the oscilloscope one can determine the light intensity as a function of the voltage displayed on the screen. By rotating the MCP one can measure a dependence between the light intensity and the rotation angle. The measurement results are described in figure 6.18. The data points can be described by a Gaussian distribution with a mean value of $\mu = (6.977 \pm 0.006)\,°$ and a standard deviation of $\sigma = (1.962 \pm 0.009)\,°$.

But the uncertainty does not only come from the rotation table but also from the rotation of the MCP in vertical direction which was not optimized. Additionally, the

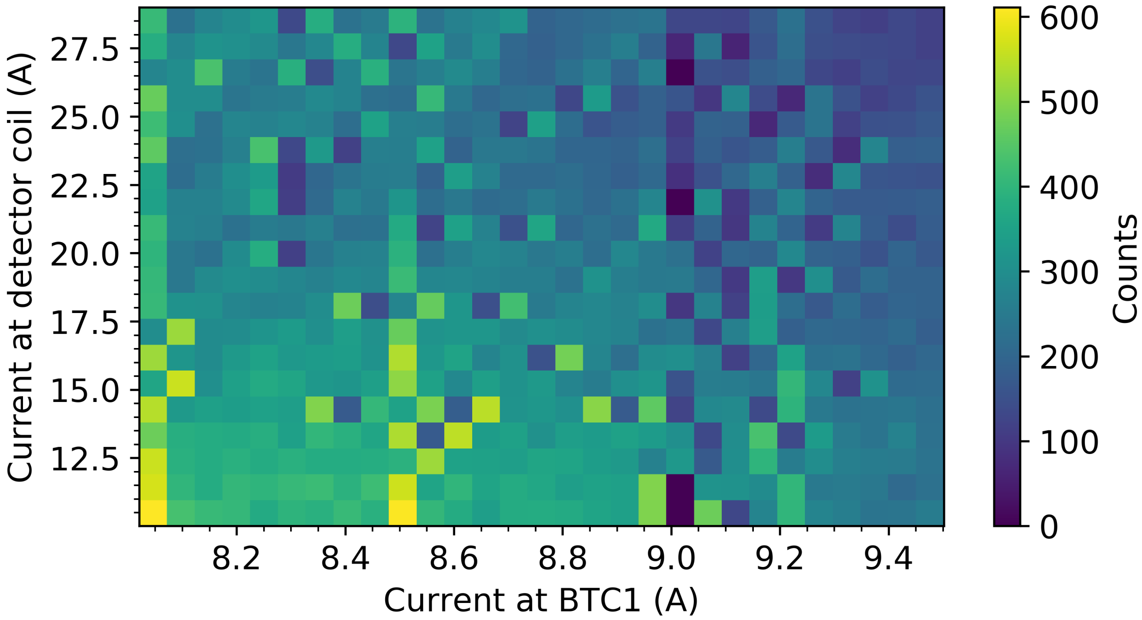

Figure 6.16: Measurement of the count rates when the detector coil is varied and additional the MCP filter is in the beamline so that the dependency between the BTC1 and BTC2 currents that was fitted in figure 6.15 is used to pass through the MCP filter.

light source for the determination of the channel angle could be not exactly orthogonal. Conclusively, there are many little unknown systematics that can have an effect on the determined orientation of the channels that is why a bias angle of $(7 \pm 2)^\circ$ is estimated. The orientation of the channel is now important to install the MCP in that way that the channels get tilted by the tilted flange so that they are as much aligned with the beam axis as possible. The tilted flange was produced with the manufacturers specification of the MCP detector in mind, i.e. 6° channel bias angle. This results in a residual channel angle of about 1° with respect to the beam axis. But in addition to the uncertainty of the orientation of the channels, the alignment of the MCP channels to the beamline axis can be affected by different aspects like the mounting and the magnetic setup. The largest share of uncertainty should be arising by the alignment of the detector coil because in the end the angle between the magnetic field line in combination with the helix of the cyclotron motion of the electron and the channel is important for entering parallel into the channels.
With the channels being aligned with the beam axis there should not be a strong deflection of the electron beam needed to achieve entering parallel to the channels. So another measurement is done where the BTC1 current and separately the detector coil current is varied. Thereby one can see in figure 6.19 once more the diagonal lines, similar to the pattern in figure 6.13, so that means the MCP detector is still not

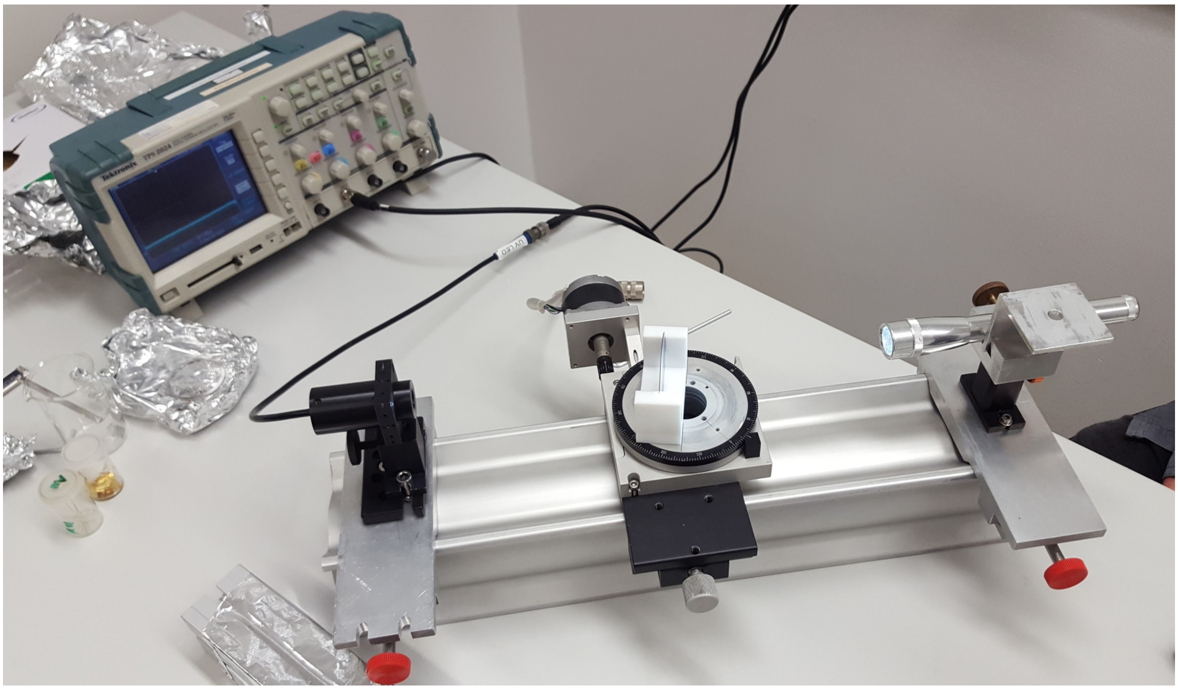

Figure 6.17: Setting to measure the orientation of the channels of the MCP detector. On the right side there is a light source, in the middle there is the single MCP of the detector lying in a holder out of teflon on a rotateable table with a degree scale. On the left side there is a photo diode connencted to an oscilloscope for measuring the intensity of the light shining through the MCP.

aligned perfectly with the magnetic field lines.

But thereafter a count rate measurement is performed with constant detector coil current while varying the deflection coils independently to scan the parameter space of deflection in a certain area around the assumed $0\,°$ spot for the electrons to enter the channels. By using low currents through the detector coil the influence of the deflection coils get stronger so that the deflection coils are able to deflect the electron beam off from the detector. This can be seen for a current of 3 A through the detector coil in combination with a current of 35 A through the eGun coil in figure 6.20, where the registered electron rate depending on the deflection coil currents is shown. These deflect the magnetic field line horizontally and vertically to the beamline axis.
The higher current of 35 A at the eGun coil in comparison to 19 A is used because the cyclotron radii as well as the angle with respect to the magnetic field line is lowered for higher magnetic fields at the creation point of the electrons as the transverse kinetic energy decreases according to equation 22.
By this measurement one can see a circular area of large count rate that resembles the

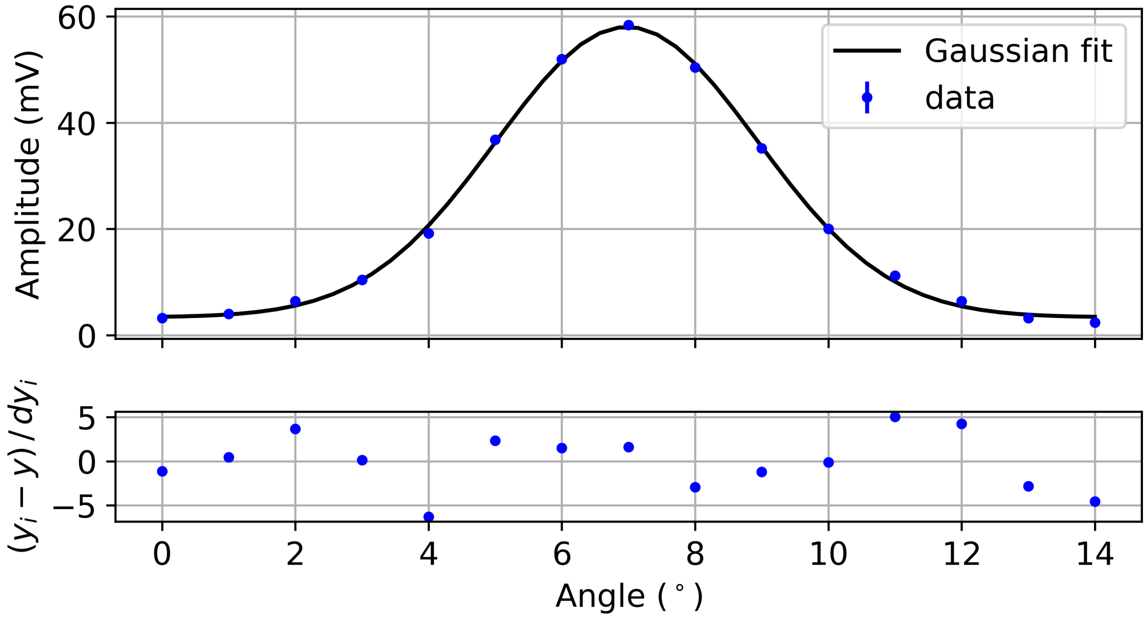

Figure 6.18: Measurement of the angular orientation of the channels by recording the light intensitiy at the photo diode after passing the MCP. The data can be well described with a gaussian of the form: $a \cdot \frac{1}{\sqrt{2 \cdot \pi \sigma^2}} \mathrm{e}^{-\frac{(x-\mu)^2}{2\sigma^2}} + bkg$. This fits the expectations as incoherent light is passing through a multislit which does not produce a sinc function but the gaussian envelope of it as intensity distribution. The fit parameters are: $a = (268.8 \pm 1.4)\,\mathrm{mV}$, $\mu = (6.977 \pm 0.006)\,^\circ$, $\sigma = (1.962 \pm 0.009)\,^\circ$ and $bkg = (3.36 \pm 0.11)\,\mathrm{mV}$. The goodness of fit is described by $\frac{\chi^2}{\mathrm{ndf}} = \frac{146.77}{11} = 13.3 \pm 0.4$.

shape of the detector. It is sampled with electrons being deflected to different positions on the MCP plane. The number of registered counts depends firstly on whether they arrived at the active area of the MCP detector which defines the clear cut to the deep blue area at the outside of the plot. Secondly, the angle with which the electrons are arriving has an impact on if they are detected efficiently or not because of the angular selectivity of the MCP detector.

Additionally, there can also be some third order effects that are not known until now. The plot does not contain a proper circle because the deflection coils deflecting horizontally are stronger than the ones deflecting vertically and the z-position of the rotational symmetry axis of the deflection coils are not exactly at the detector.

This effect can be seen in figure 6.21, where the deflection is different for each deflection coil pair although they have the same magnetic field at the detector. As an example, for 2 mT produced by the large deflection coils the magnetic field line is deflected by 2.96 cm at the detector position whereas the small deflection coils are deflecting 2.54 cm for the same magnetic field. For this simulation a current of 8 A through the BTC2

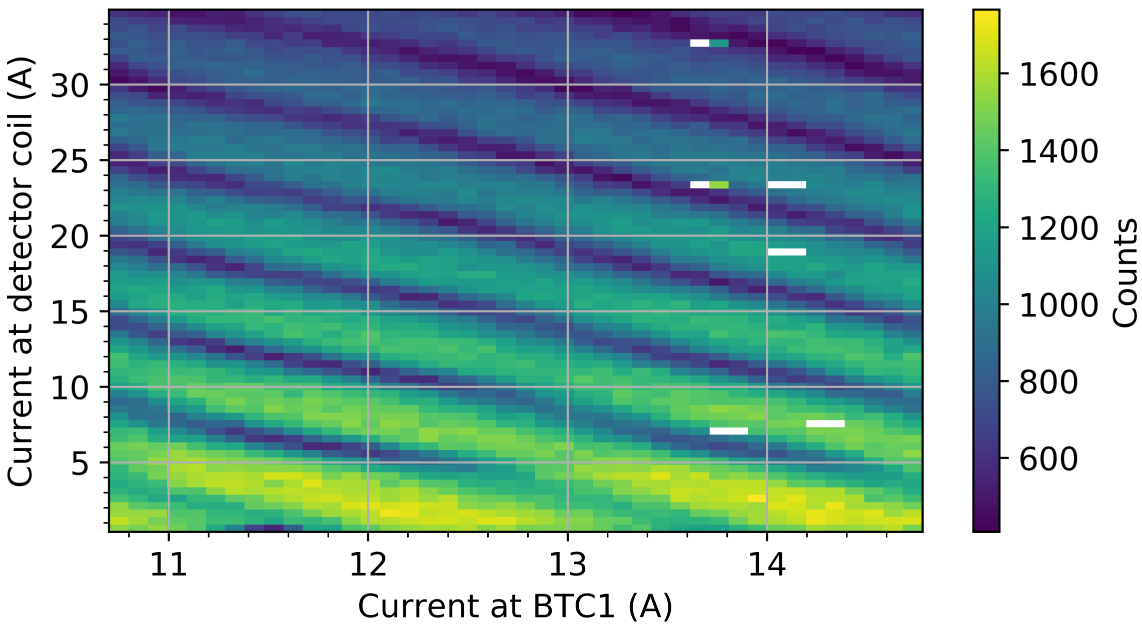

Figure 6.19: Repeated measurement of the count rate where the current at the BTC1 and independently the current at the detector coil is varied. This time the channels of the MCP detector should be approximately aligned with the beam axis. One can see again diagonal lines indicating that the channels are still not perfectly aligned at least with the magnetic field lines. For this measurement electrons with an energy of 5 keV are used. Otherwise one would not see phase effects as the cyclotron frequency is too high for electrons with an energy of 50 eV.

and a current of 3 A through the detector coil is applied to the simulation software Bfield_3D.

Most of the area where the MCP detector is hit is colored yellow; there the electrons are detected homogeneously and no angle-selective detection can be seen. Two regions are striking out from this. This is the region on the upper left side (marked with a) and the region on the right side (marked with c) with much less area. Both areas have to be compared. The area where electrons have an angle of near to 0° to the channel direction should have another spectral shape. Therefore a measurement with a multi channel analyzer is performed as described in 5.8. It is expected that there the amplification is much lower and therefore the spectrum is shifted to the left compared to the other spectra as described in section 4.3.1. So both blue areas and an arbitrary point in the yellow area (marked as b) are analyzed with the MCA. In these spectra one can see that the area b) on the right side differs from both other analyzed points as in this region only lower channel numbers of the MCA are populated. In comparison to this the area on the upper left a) is quite similar to the region b) as it has a similar

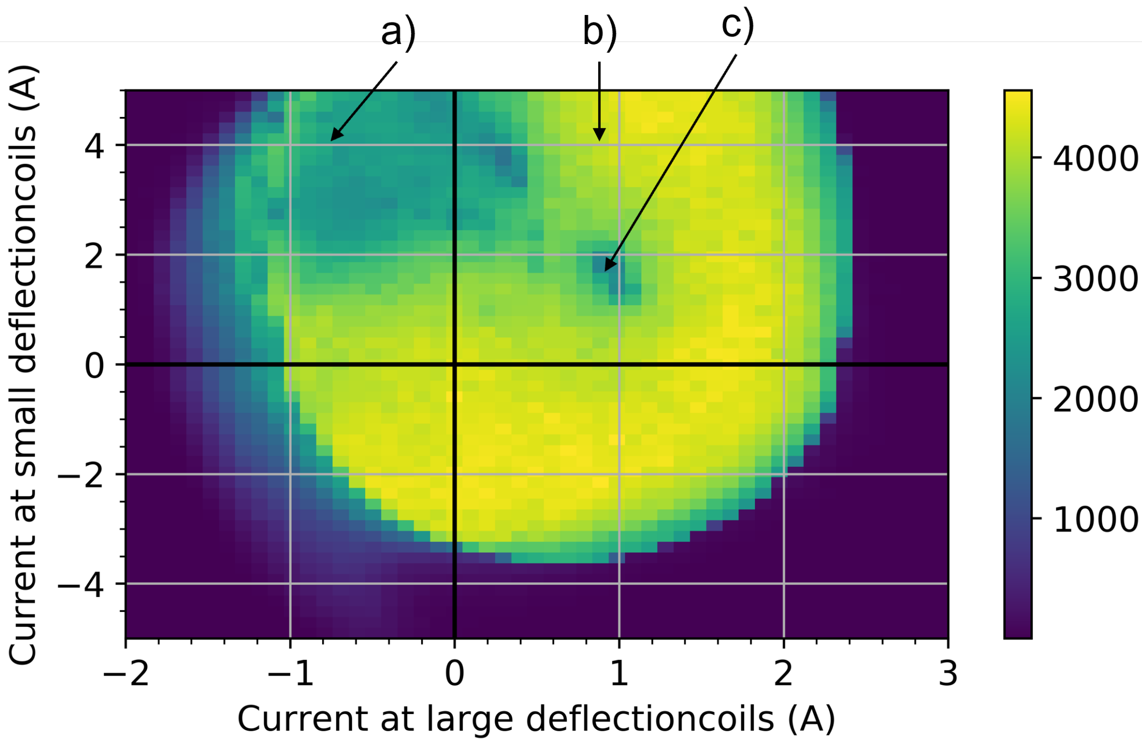

Figure 6.20: Measurement of the count rate when only the large deflection coils and the small deflection coils are varied independently from each other and electron energies of 50 eV are used. This is done at a current of 3 A through the detector coil and 35 A at the eGun coil. One can see that there is a little local minimum marked with c), a rather large light blue area marked with a) and the rest being nearly homogeneously yellow marked with b). The dark blue area is corresponding to the case when the deflection was so strong that the electrons did not hit the detector anymore.

distribution of counts for the higher channel numbers. This is a strong hint that the local minimum is corresponding to the effect that electrons enter the channels with smaller angles to the channel and thus the effect of angular selective detection.

Due to the analysis of the spectral shapes the region of interest could be determined to the region marked with c) so this needs to be examined further.

When the detector coil is set to higher magnetic fields then also the deflection coils have to be set to higher magnetic fields to achieve the same angle of deflection. Due to the constant resolution of the digital-to-analog converter there are more steps of deflection that can be investigated as the scale factor for the impact of the deflection coils is decreased. Thus, a more detailed look into the region of interest is possible. This measurement is visible in figure 6.23 where a measurement of the count rate is done when the current at the detector coil as well as at the eGun coil is set to 35 A and the deflection coils are varied independently from each other.

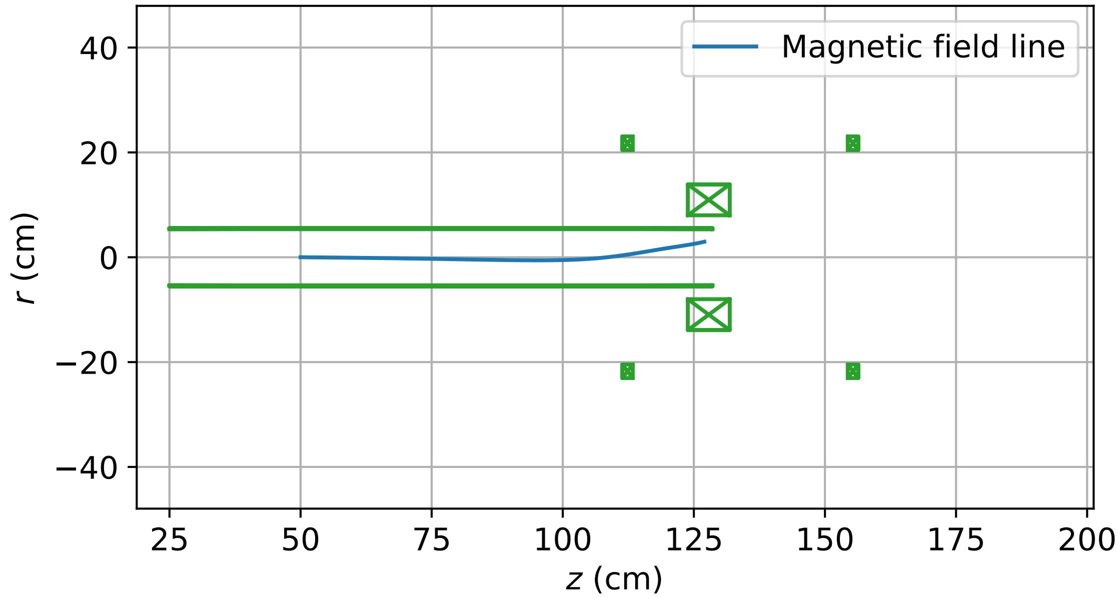

(a) large deflection coils

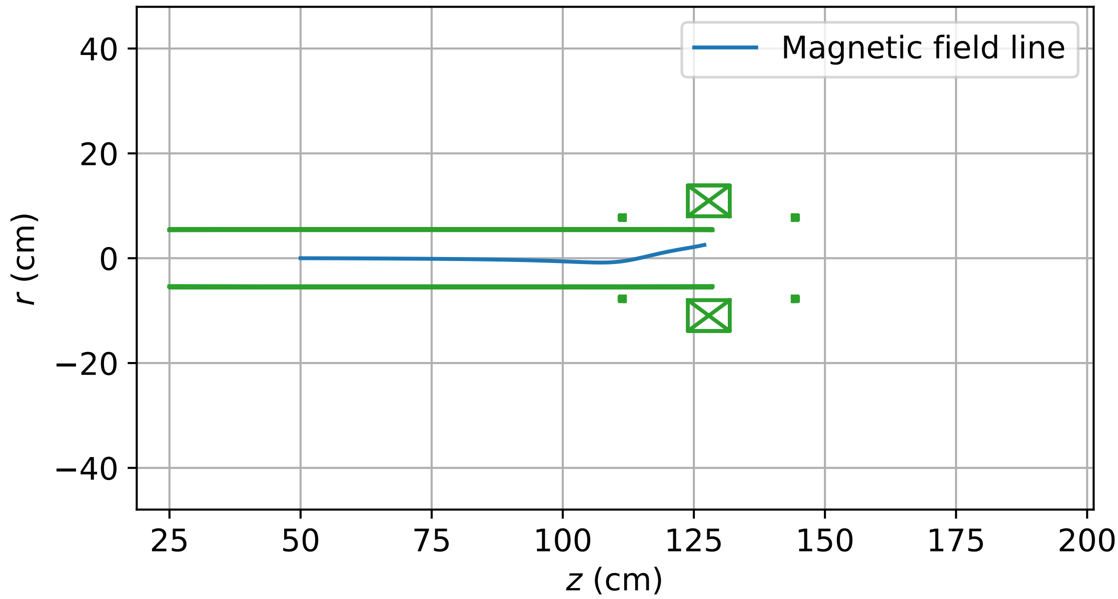

(b) small deflection coils

Figure 6.21: Simulations with the software Bfield_3D of the magnetic field line for the large deflection coils (a) and for the small deflection coils (b) for 2 mT. The thick green lines starting at a z-position of 25 cm are visualizing the beam tube, the big rectangles the detector coil and the small rectangles the deflection coil pairs.

This closer look into the region of interest is only possible because the MCP channels are nearly parallel to the magnetic field lines so that not much adjustment with the

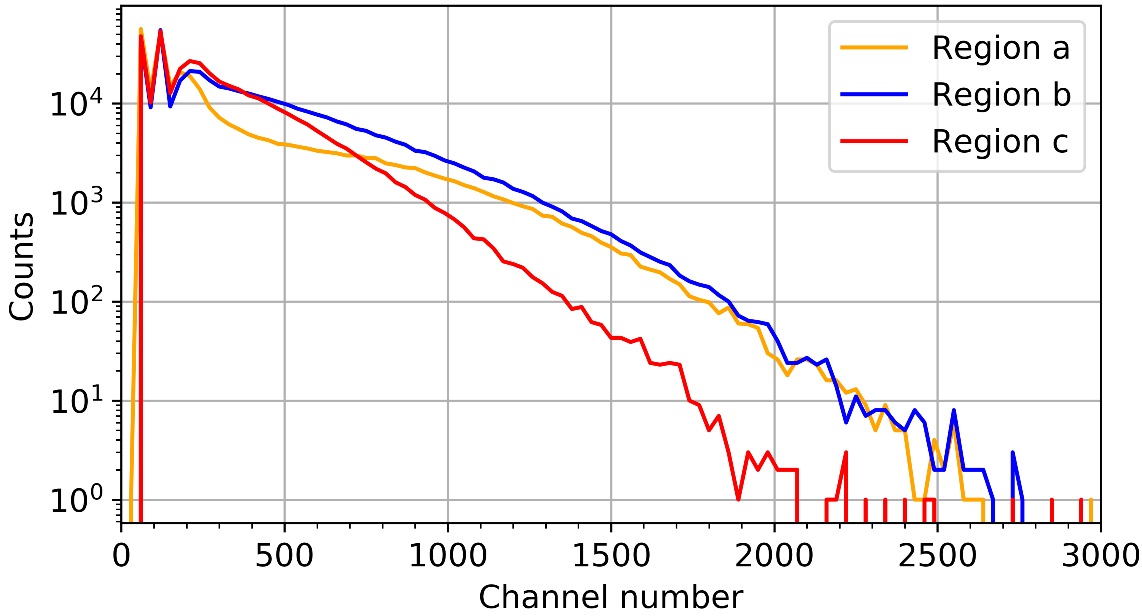

Figure 6.22: MCA spectra of the three regions marked in 6.20.

deflection coils is needed. To get a more reliable reduction factor this measurement is fitted with two two-dimensional normal distributions of the form

$$f(x,y) = \sum_{i=u,l} \left(a_i \cdot \frac{1}{\sqrt{2\pi\sigma_{x,i}^2}} \cdot \mathrm{e}^{-\frac{(x-\mu_{x,i})^2}{2\sigma_{x,i}^2}} \cdot \frac{1}{\sqrt{2\pi\sigma_{y,i}^2}} \cdot \mathrm{e}^{-\frac{(y-\mu_{y,i})^2}{2\sigma_{y,i}^2}} \right) + bkg. \tag{46}$$

This is visible in figure 6.23 with its fit parameters. The ratio of count rates between the minimum (18.5) and the background (1028) fitted in figure 6.23 is $\frac{min}{bkg} = 55.74$ which is an unprecedented suppression factor. There are two distinct minima very close to each other. This may have occurred due to substructures in the MCP that arise from the manufacturing process. MCPs are made from multiple different hexagonal sub-elements of channels as visible in figure 6.24. Although the channel orientation within the hexagons is very homogeneous it may vary between different sub-elements so that when the electron beam hits two hexagons also two different main channel angles are present.

The effect of different energies and initial polar angles at the eGun is measured to further test the hypothesis that the minimum is due to the angular selectivity of the MCP detector. Therefore, a last measurement series for crosschecking is done with energies of 5 keV. That allows to set a more defined initial polar angle to the electrons. In contrast to the customized standard setting for currents as described in table 4 the

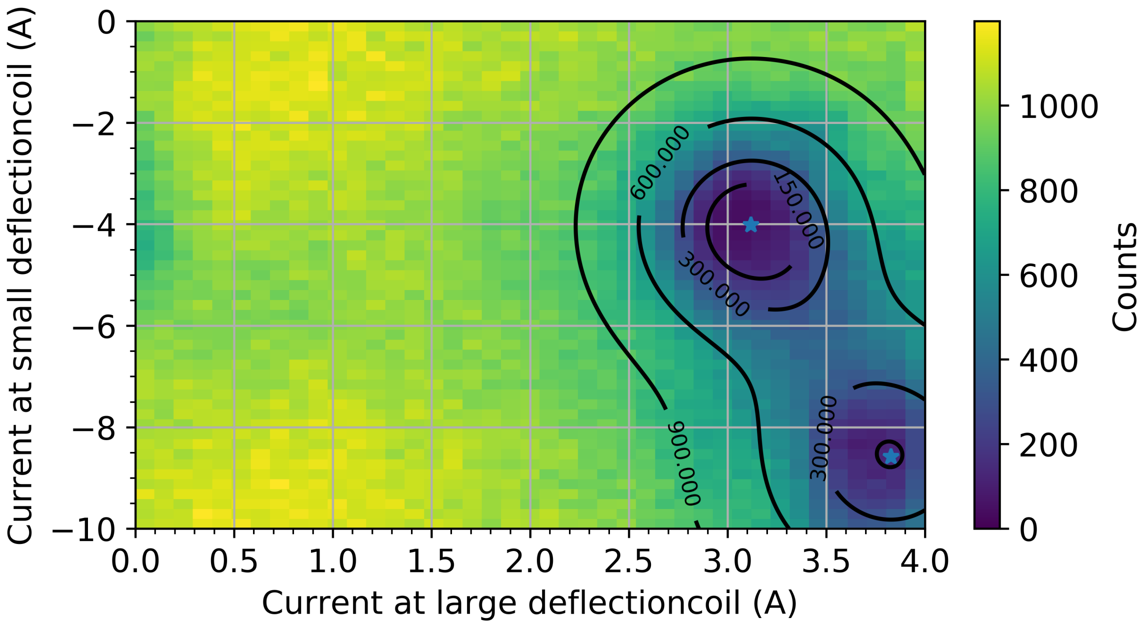

Figure 6.23: Measurement of the count rate when the small and the large deflection coils are varied independently from each other and with electron energies of 50 eV but with a detector coil current of 35 A resulting in a more detailed view on the local minium in comparison to figure 6.20. Additional to the measured count rates a fit consisting of two two-dimensional normal distributions with the function 46 is applied and the mean positions of the normal distributions are marked (∗), as well as the contour lines of it. The fit parameters are for the upper normal distribution: $a_u = (-980.2 \pm 2.0)$ counts, $\mu_{x,u} = (3.1195 \pm 0.0016)$ A, $\sigma_{x,u} = (0.6222 \pm 0.0027)$ A, $\mu_{y,u} = (-4.019 \pm 0.006)$ A, $\sigma_{y,u} = (2.301 \pm 0.009)$ A and for the lower normal distribution $a_l = (-879.3 \pm 2.2)$ counts, $\mu_{x,l} = (3.828 \pm 0.004)$ A, $\sigma_{x,l} = (0.750 \pm 0.008)$ A, $\mu_{y,l} = (-8.583 \pm 0.010)$ A, $\sigma_{y,l} = (2.851 \pm 0.024)$ A. Additionally the background is fitted to $bkg = (1028.4 \pm 0.9)$ counts.

current through the detector coil is set to 35 A to get smaller cyclotron radii. The measurements are done with several different currents through the eGun coil and at each current through the eGun coil both deflection coils are varied in the region of the local minimum which is presented in figure 6.25. Higher currents through the eGun coil have the effect that the electrons are created in a higher magnetic field so that the electrons can not be accelerated as good non-adiabatically and thus follow the magnetic field lines more accurate. Furthermore in regions of adiabatic electron motion the angle of the cyclotron motion becomes smaller as the transverse kinetic energy becomes smaller proportional to the ratio between final magnetic field to starting magnetic field (see equation 22). In combination this should lead to higher reduction factors, when the starting magnetic field is as high as possible.

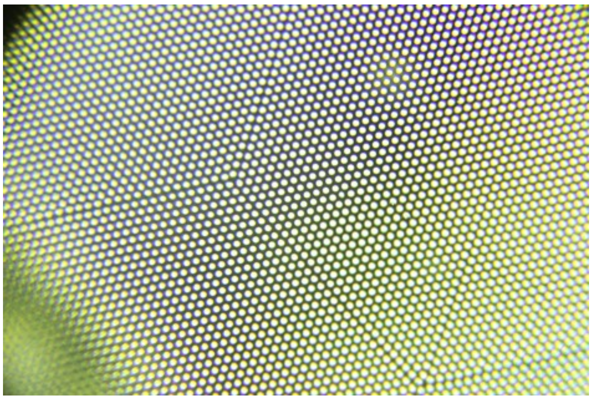

Figure 6.24: Picture of the MCP filter taken with a microscope. One can see the different channels and also the hexagonal substructure the MCP is made of. Picture taken by Kevin Gauda.

This measurement series is done with electrons that are set to start with 0° and once with 5°. For 0° electrons one can see detector effects even for 0 A at the eGun coil, but they are not very distinct. As expected this is getting more pronounced for higher magnetic fields at the eGun. One can see that the overall count rate at 2 A and 0° is lowered despite having measured with the same configuration and only changed current at the eGun coil. Eventually, this can be explained by deviations of the eGun-efficiency that may arise from UV-LED power variation with time or with temperature.
However, for the case of 5° electrons for 0 A through the eGun coil one can not see any detector effect but much less count rate. This can occur due to losses of electrons because of the relatively high polar angle in combination with low magnetic fields resulting in electrons hitting the inside of the vacuum chamber. For 2 A and 5° one can see a hint on the detector effect and this is getting more pronounced for higher currents at the eGun coil as well. The lower currents at the eGun coil let the electrons arrive with larger angles at the detector and thus the deflection coils can not achieve that the electrons will enter the channels parallel to their orientation. When comparing the measurement results for the different currents through the eGun coil between the different electron angles then one can see that for 10 A at the eGun coil both results are very similar and for 35 A one can basically not see any difference in the count rate. This is due to the fact that the non-adiabatic motion, on which the eGun bases, does not work as good. In this case the eGun does not work properly and one has no ability to set an angle to the electrons. So for 35 A at the eGun one basically always shoots electrons with near to 0° independently of what is set to the LabView program for steering the eGun.
The observed effects and cross-checks are very consistent with the explanation via angular-selective electron filtering. The next subsection will focus on simulations of

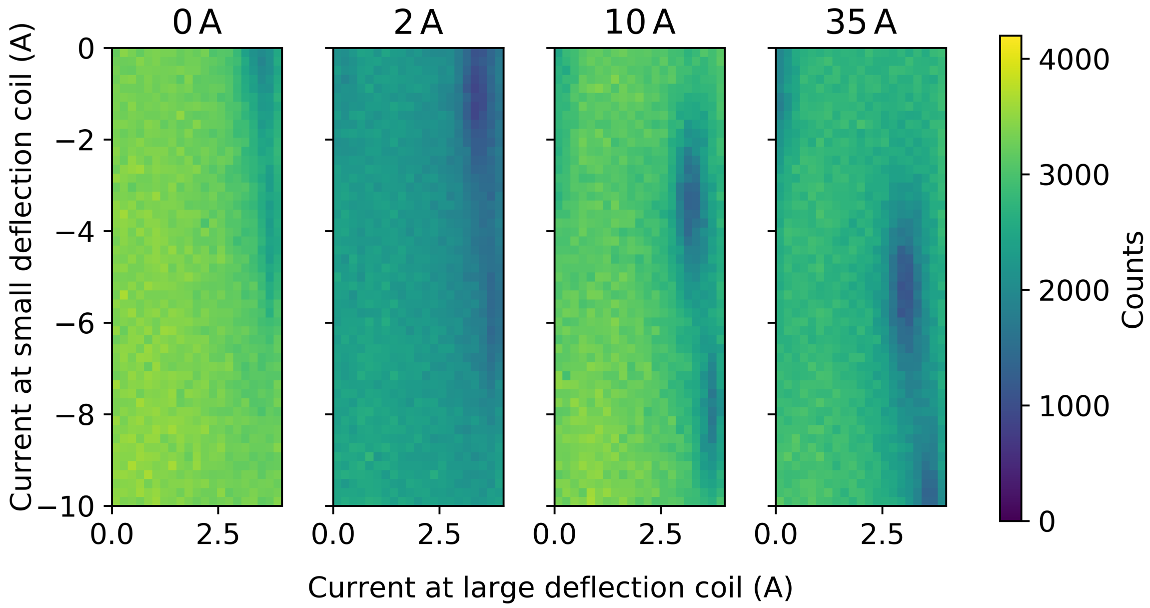

(a) Polar angle set to 0 ° at the eGun.

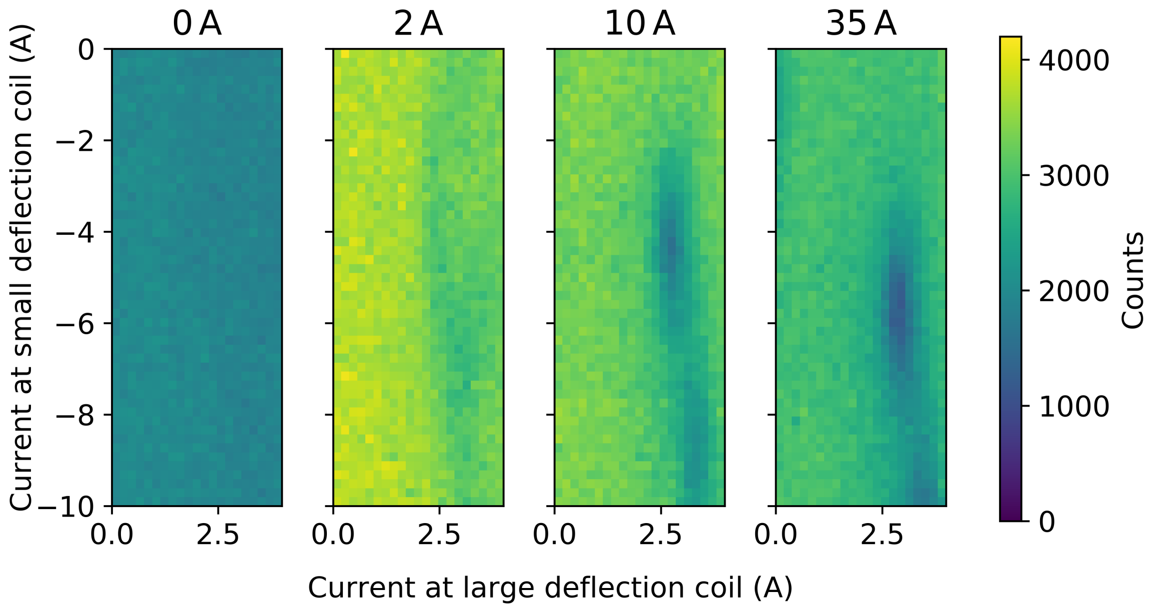

(b) Polar angle set to 5 ° at the eGun.

Figure 6.25: Graphs to compare different magnetic field settings in combination with polar angles at the eGun of 0 ° and 5 °. The current above each plot is belonging to the eGun coil.

the test setup to verify that the measurement results are also obtained with theoretical considerations to support the experimental results.

6.5 Simulations with Kassiopeia

The simulations of the test setup are realized by the particle tracking software Kassiopeia, which has been developed within the KATRIN collaboration [55].

6.5.1 Geometry, magnetic and electric fields

For Kassiopeia the geometry of the test setup has to be specified as well as the electric and magnetic fields. This is done in that way that surfaces can be set on a potential to introduce electric fields. For magnetic fields one has to introduce a volume consisting of a number of windings and a current through it.

Then the magnetic and electric fields are calculated so that the equation of motion for the simulated particle can be solved in each discretized steps on the way between start and end point. Kassiopeia then gives out for each step values like the transverse energy, longitudinal energy, positions in x, y and z direction as well as magnetic and electric fields. For a whole overview of the output values see in the phd thesis of Jan Behrens [52]. There is also the opportunity to simulate different types of particles but for this purpose only electrons were considered.

Additionally one can set an angular distribution of the starting electrons in polar and azimuth direction as well as the point of creation of the electrons.

The eGun, as it is used in the test setup, was extensively studied within a PhD thesis [52] and is not part of the simulations here. Instead the electrons are only created at the front plate with an estimated angular distribution of azimuth angles $0^\circ < \alpha_{az} < 10^\circ$ and polar angles of $0 < \alpha_p < 1$.

To stop the electrons in the setup one has to use "terminators": When an electron fulfills the condition for such a terminator then the tracking for this particle is stopped.

The geometry as well as the tracks of the particles and different output values can then be visualized by various programs for example Paraview. Further information on Kassiopeia can be found in [56] and [52].

The configuration files are mostly taken from the bachelor thesis of Richard Salomon who used it to simulate the test setup to optimize the adiabaticity of the test setup with his simulations [48]. Those files have been modified to be able to use each coil in the setup independently.

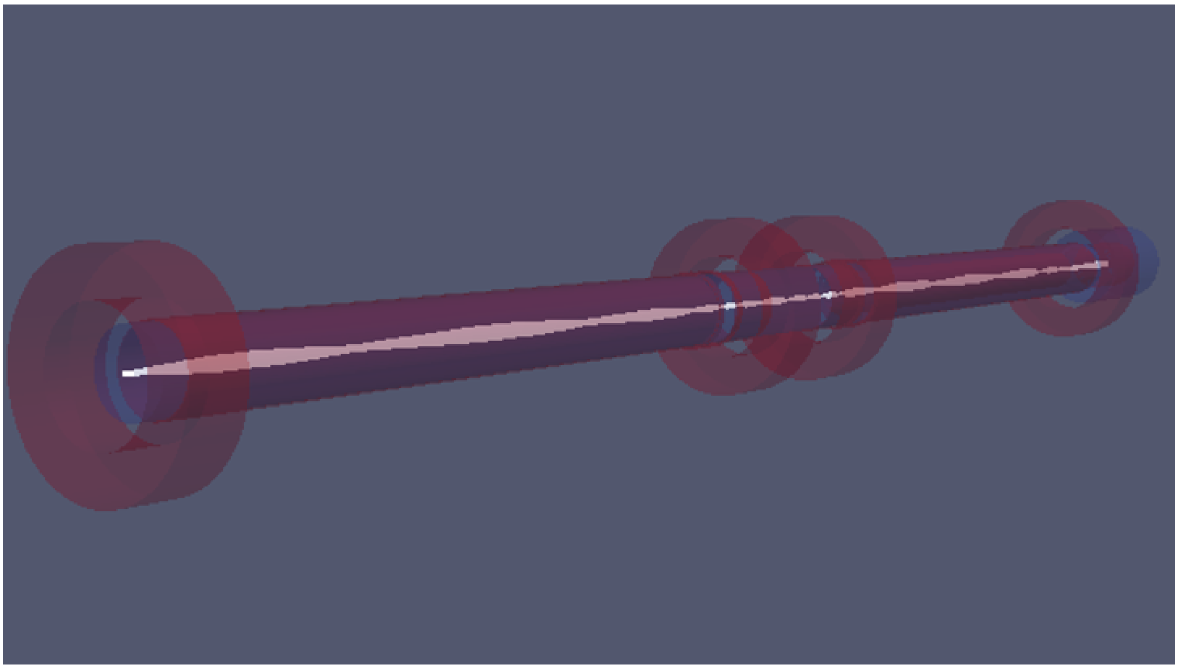

Figure 6.26: Imaging by the open-source visualization application Paraview of the simulation of electrons by the particle tracking software Kassiopeia. The red volumes are describing the cylindrical coils of the test setup generating the magnetic fields for the guidance of the electrons. The white color is visualizing the tracks of 1000 simulated electrons through the test setup. On the right side the creation of the electrons take place and on the left side they are terminated at the position of the detector.

6.5.2 Simulations of the tilted MCP detector

Simulating an actual MCP with all of its channels and the secondary electron emission properties within Kassiopeia would be a major effort. Here, instead, certain assumptions are made to the detector properties and its response. These are applied on the last two steps of the Kassiopeia simulation of the test setup at the corresponding actual detector position. The last two steps were used to calculate the final direction with respect to the z-axis. This treatment can be justified by using the equation 37 and solving it to the amount of cyclotron periods n within the MCP channel length l

$$n = \frac{l}{v_{\parallel}} \cdot \frac{e \cdot B(I)}{2\pi m_e}. \tag{47}$$

One can calculate that the distance the electron is traveling through the channels in the $500\,\mu$m thick MCP is much fewer than one cyclotron period. Hereby $B(I)$ is the magnetic field applied to an electron with the longitudinal velocity $v_{\parallel}$. As an example one can set a magnetic field of $B(I) = 70\,\mathrm{mT}$ which is the largest applied magnetic field at the detector and a length $l = 500 \cdot 10^{-6}\,\mathrm{m}$ in combination with a longitudinal

kinetic energy of 5 keV. This results in an amount of $n = 0.02$ periods within the first plate of the chevron stack MCP detector. From that one can assume that the electron is moving on a straight line through the channel. So, using the last two steps for the calculation of the direction is sufficient.
Every angle needs to be weighted with a probability to pass through the channel without interaction with the walls. Even an angle of 0.5 ° has not the probability of 100 % to pass the channel with no interaction.
To calculate the probability for each angle one has to consider the cylindrical geometry. The projection of a circle with radius r in the x-y plane that is rotated with an angle α around the x- or y-axis is an ellipse with a semi-major axis $a = r$ and a semi-minor axis $b = r \cdot \cos(\alpha)$ when still looking frontal onto the x-y plane. For the case of a rotated cylinder the circle in the entrance and the circle in the output will both look like an ellipse with the same length of the major and minor semi axis. As one can see in figure 6.27 due to the rotation the open area of the channel is reduced. This area can be calculated as the intersection between two shifted ellipses. They are shifted by the length $d = l \cdot \sin(\alpha)$, which is the projection of the length of the channel l on the x-axis.
Thus, the center of the two ellipses is at $d/2$. Now the open area can be calculated by four times the ellipse sector of the semi minor axis with the angle β minus the triangle with the height $h = y\left(\frac{d}{2}\right)$ and the base $g = \frac{d}{2}$

$$A_{\text{intersection}} = 4 \cdot A_{\text{ellipse sector}} - \frac{y(d/2) \cdot d/2}{2}. \tag{48}$$

An ellipse can be described by the formula:

$$\frac{x^2}{a^2} + \frac{y^2}{b^2} = 1 \tag{49}$$

$$\Rightarrow y(x) = \pm\sqrt{b^2 - \frac{b^2}{a^2} \cdot x^2} \tag{50}$$

with $a = r \cdot \cos(\alpha)$ and $b = r$

$$y(x) = \pm\sqrt{r^2 - \frac{x^2}{\cos(\alpha)^2}}. \tag{51}$$

The sector of an ellipse can be calculated by

$$A_{\text{ellipse sector}}(\phi) = \frac{a \cdot b}{2} \left(\phi - \sin(\phi)\cos(\phi)\right), \tag{52}$$

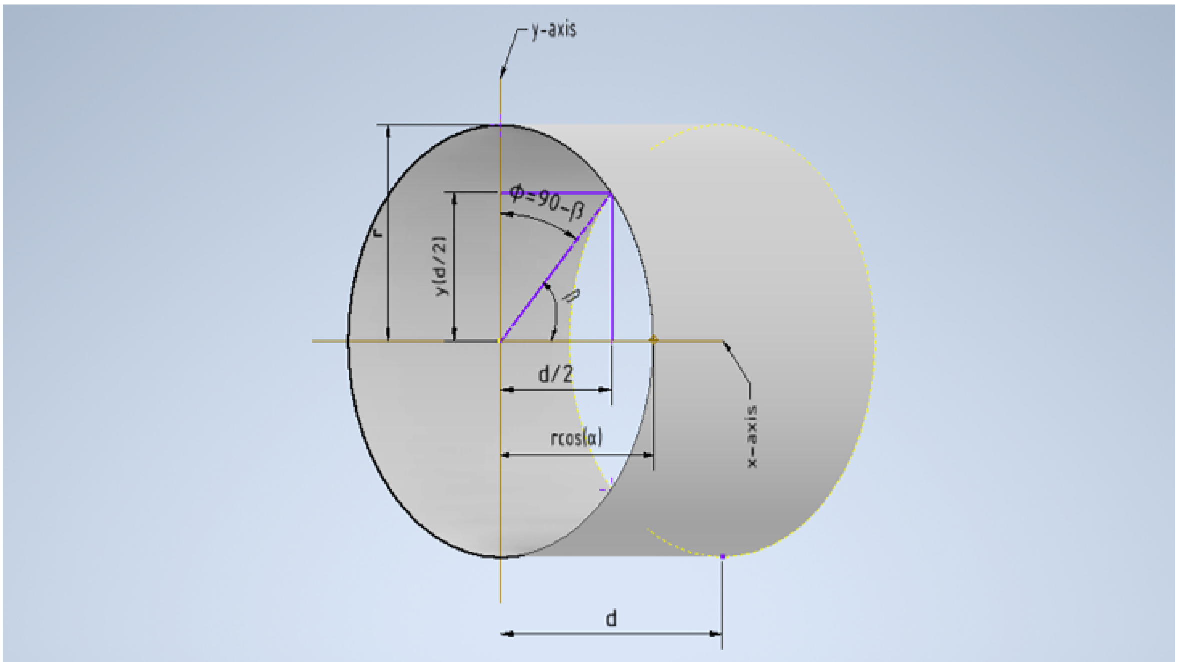

Figure 6.27: Cylindrical channel that is rotated around the y-axis to describe a tilted MCP channel.

where ϕ is the angle starting from the semi major axis so in this case at the y-axis and the angles are given in radiant.
The sector of the semi minor axis with the angle β is needed so this can be calculated via:

$$\begin{aligned} A_{\text{ellipse sector}}(\beta) &= \frac{A_{\text{ellipse}}}{4} - A_{\text{ellipse sector}}(\phi) \\ \Leftrightarrow &= \frac{a \cdot b \cdot \pi}{4} - \frac{a \cdot b}{2} (\phi - \sin(\phi)\cos(\phi)) \\ \Leftrightarrow &= \frac{a \cdot b}{2} \left(\frac{\pi}{2} - \phi + \sin(\phi)\cos(\phi) \right) \end{aligned} \tag{53}$$

with $\beta = \frac{\pi}{2} - \phi$, $\cos(\gamma) = \sin(\frac{\pi}{2} - \gamma)$ and $\sin(\gamma) = \cos(\frac{\pi}{2} - \gamma)$

$$A_{\text{ellipse sector}}(\beta) = \frac{a \cdot b}{2} (\beta + \cos(\beta)\sin(\beta)) \,. \tag{54}$$

For this case $a = r \cdot \cos(\alpha)$ and $b = r$. So the area is:

$$A_{\text{ellipse sector}}(\beta) = \frac{r^2 \cdot \cos(\alpha)}{2} (\beta + \cos(\beta)\sin(\beta)) \,. \tag{55}$$

β can be calculated as:

$$\beta = \arctan\left(\frac{y\left(\frac{d}{2}\right)}{\frac{d}{2}}\right) \tag{56}$$

The probability to pass the channel without interaction is now calculated as the ratio between the open area $A_{\text{intersection}}$ and the total area of the entry ellipse A_{ellipse}:

$$P(\alpha) = \frac{A_{\text{intersection}}(\alpha)}{A_{\text{ellipse}}} \tag{57}$$

Consideration of tilted channels in the Test setup To perform realistic simulations a tilt angle of the channels with respect to the z-axis is introduced that mimics a misalignment of the original setup. As mentioned above the direction of the electron is calculated with the last two steps of the track. The tilted channels can be described without loss of generality by a normalized vector $\vec{n} = (0,0,1)^T$ rotated around the y-axis.

This can be done by applying a rotational matrix $R_y(\alpha)$:

$$\begin{aligned}\vec{n'} =& R_y(\alpha)\vec{n} \qquad (58)\\ =& \begin{pmatrix} \cos(\alpha) & 0 & \sin(\alpha) \\ 0 & 1 & 0 \\ -\sin(\alpha) & 0 & \cos(\alpha) \end{pmatrix} \cdot \begin{pmatrix} 0 \\ 0 \\ 1 \end{pmatrix} \\ =& \begin{pmatrix} \sin(\alpha) \\ 0 \\ \cos(\alpha) \end{pmatrix}\end{aligned}$$

Now the angle δ between the tilted channels $\vec{n'}$ and the direction of the electrons $\vec{v}$ can be calculated via:

$$\delta = \arccos\left(\frac{\vec{n'} \cdot \vec{v}}{|\vec{n'}| \cdot |\vec{v}|}\right) \tag{59}$$

This angle δ can then be inserted in the probability function 57. Now a simulation of the measurement in figure 6.3 is performed. The simulations have been done by using 1000 electrons for every magnetic field configuration with previously set starting parameters. The properties of the electrons were an energy of 5 keV and a random

azimuth angle of $0^\circ < \alpha_{az} < 10^\circ$ and a polar angle of $0^\circ < \alpha_p < 1^\circ$. Then for every electron in every magnetic field configuration the probability to pass the channels without interaction is calculated.
An example for this is given in figure 6.28a. There a tilt angle of the channels of 1° is considered as well as a length of the channels of $60\,\mu m$.
The length of the channel can not be chosen from the specifications of the MCP detector because the considered length of the channel is only the effective length of the channel. That means that electrons are not counted if they enter the channel behind the threshold length. In reality, this effective length will certainly not be a single threshold, but an energy- and incident angle-dependent probability. For simplicity, only the single threshold is considered here, but further refinements to the simulation are possible.
One can see that there are diagonal lines as previously seen in 6.3. The periodicity in horizontal and vertical direction is also very similar. However the gradient of the count rate from both figures is the other way around. But this can be due to unknown detector effects because of the large differences in magnetic fields. These unknown effects are not considered in the simulations.
It can be concluded that, although not all of the measured effects are described by the simulation, the angular-selective electron detection can be qualitatively described with the applied assumptions.

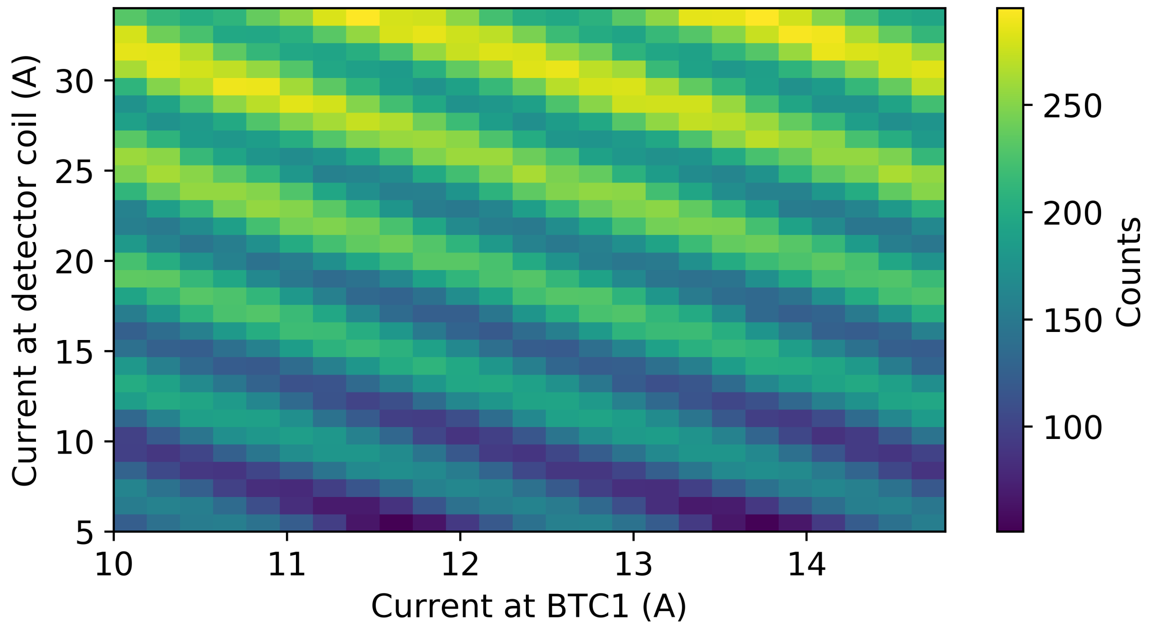

(a) simulated

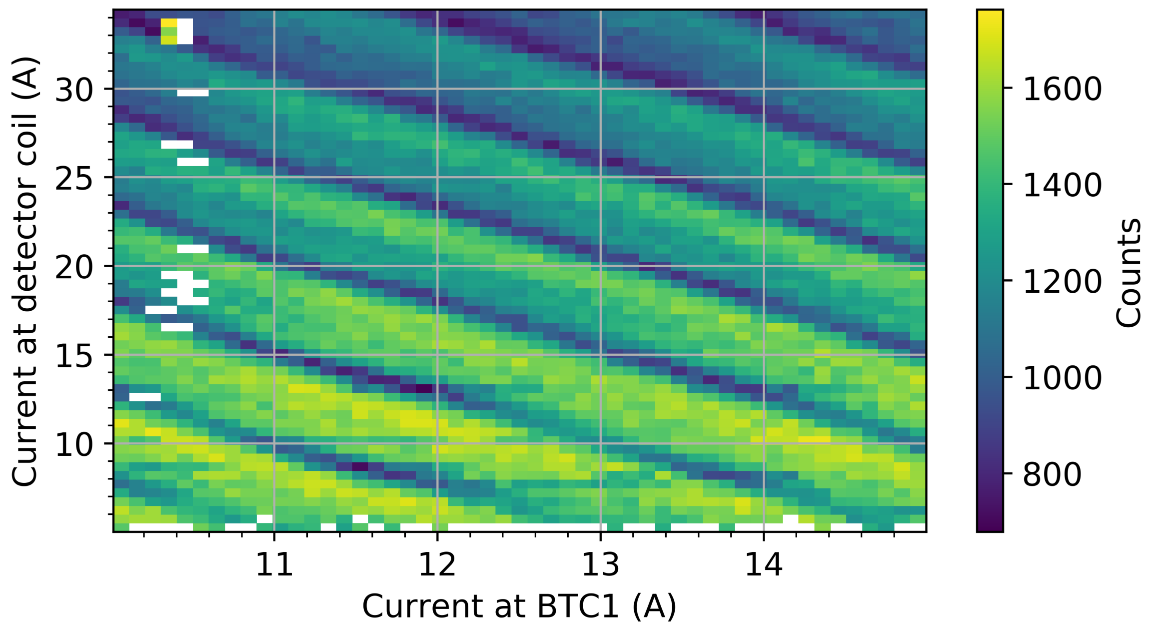

(b) measured

Figure 6.28: Graphs to compare the simulated results with the measured results. One can see that the periodicity in horizontal and in vertical direction is very similar whereas the gradient of count rate is exactly different in vertical direction. Only the form is slightly different which can be seen at the thickness of the diagonal blue lines.

7 Conclusion & outlook

Within this master thesis the approach of using an active transverse energy filter (aTEF) for the suppression of the detection of electrons with a narrow angular distribution is investigated with several measurements and simulations. This active transverse energy filter was realized by using an MCP detector that generated different output signals in dependence of the electron movement. Hence, a lot of fine-tuning in the electron energy, the starting angles at the eGun, the magnetic fields and the angle of the MCP channels had to be done. Therefore the channel bias angle of the MCP detector needed to be examined and has been determined to $(7 \pm 2)\,^{\circ}$. In order to align the channels of the MCP detector with the magnetic field lines a flange that is tilted to $6\,^{\circ}$ is manufactured and installed between the BT2 and the MCP detector. Additionally, for the purpose of aligning the channels with the magnetic field lines there are installed two pairs of deflection coils perpendicular to each other for making a deflection of the magnetic field lines at the detector position possible. With these measures it could be shown that electrons with very small cyclotron radii in combination with a trajectory that has a small angle to the channels of the MCP generate a very much reduced signal. In a specific fine-tuned setup a ratio between the minimum count rate and the maximum count rate has been determined to 55 where the only difference was the deflection of the magnetic field lines at the detector while the electron beam still hit the active area of the detector.

The simulation has also verified the measurement data when applying an angular dependent model to the calculated trajectories of the electrons.This proves the concept of the angular dependent electron filtering with an aTEF.

There are strong indications that the major remaining background in the KATRIN experiment stems from Rydberg-ionization electrons within the Main Spectrometer and, therefore, has very low transverse energy and thus small cyclotron radii and small angles to the magnetic field line. The approach of angular dependent filtering is tested for a possible application in front of the detector or to substitute the detector directly.

From the start point of the results of this thesis there are two main possibilities to implement such a filter into KATRIN: An MCP-based aTEF for KATRIN would be exploiting the secondary electron emission principle of commercially available MCPs. On the other hand, it would be made of custom-made hexagonal structures that are low in radioactivity. These would require intense research and development on the secondary electron emission material. The MCP-based aTEF could be placed in front of the post acceleration electrode. For high transverse energies, corresponding to those of the signal electrons, the secondary electron emission would be significantly higher than

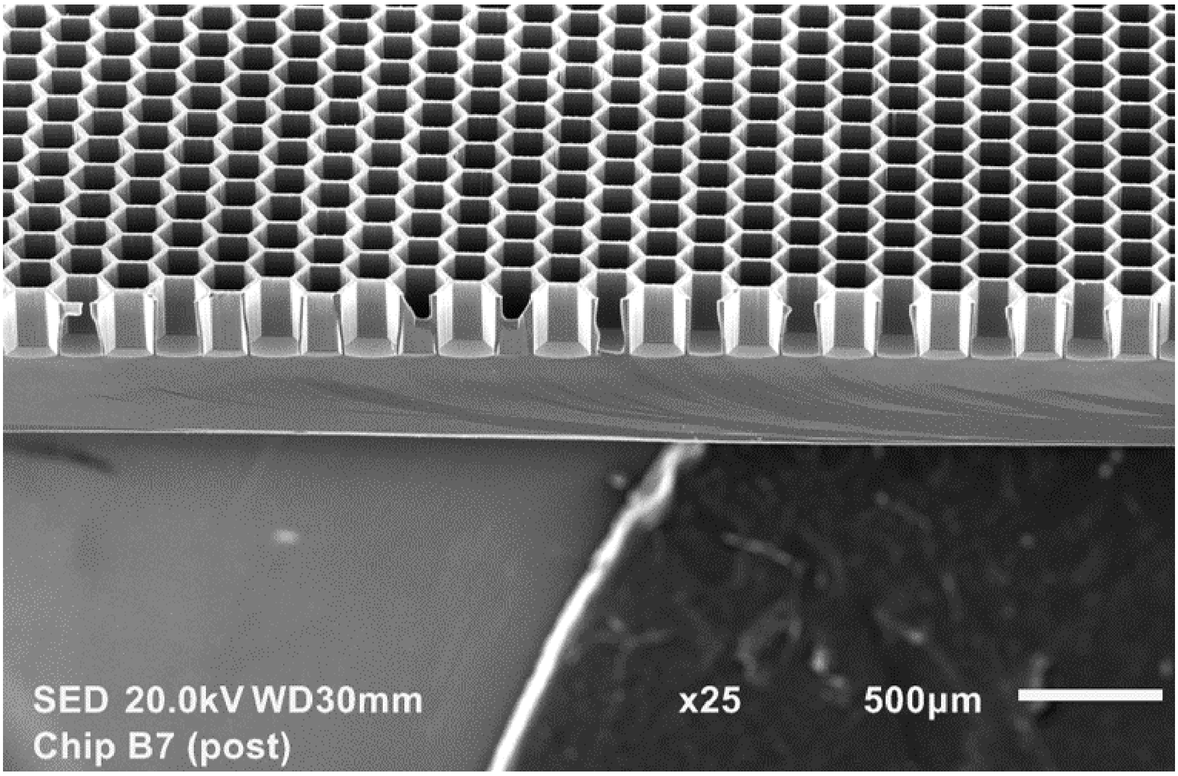

Figure 7.1: Scanning electron microscope picture that shows a micro structured silicon chip. This is an important step towards nanofabrication of either custom MCPs or structurization of the KATRIN FPD. Image by Kevin Gauda.

for low transverse energies, corresponding to those of the suspected major background electrons from Rydberg-atoms. By applying a certain threshold the transverse energies should then be distinguishable.
Another idea is to directly imprint such hexagonal microstructures into the KATRIN Focal Plane Detector, which is a pixelized silicon PIN-diode. The walls that are collinear to the z-axis of the spectrometer of such a diode-based aTEF should be electron detecting, while the floor of these structures would be blind.
Both approaches share the need to nanofabrication of silicon. The research project is therefore conducted in cooperation with Prof. Dr. Pernice of the Institute of Physics, WWU Münster.
Some attempts have already been made to create a hexagonal microstructure in silicon and silicon PIN-diodes, which is an important first step towards an aTEF. A promising example of a structured silicon chip is shown in figure 7.1.

References

[1] Wolfgang Pauli. “Pauli letter collection: letter to Lise Meitner”. Typed copy. URL: https://cds.cern.ch/record/83282.

[2] “The Nobel Prize in Physics 1995 - Press Release”. In: (1995). URL: http://www.nobelprize.org/nobel_prizes/physics/laureates/1995/press.html?.

[3] C. L. Cowan et al. “Detection of the Free Neutrino: a Confirmation”. In: *Science* 124.3212 (1956), pp. 103–104. ISSN: 0036-8075. DOI: 10.1126/science.124.3212.103.

[4] Bruce T Cleveland et al. “Measurement of the solar electron neutrino flux with the Homestake chlorine detector”. In: *The Astrophysical Journal* 496.1 (1998), p. 505.

[5] Q. R. Ahmad et al. “Measurement of the Rate of $\nu_e + d \rightarrow p + p + e^-$ Interactions Produced by ^8B Solar Neutrinos at the Sudbury Neutrino Observatory”. In: *Phys. Rev. Lett.* 87 (7 July 2001), p. 071301. DOI: 10.1103/PhysRevLett.87.071301.

[6] Q. R. Ahmad et al. “Direct Evidence for Neutrino Flavor Transformation from Neutral-Current Interactions in the Sudbury Neutrino Observatory”. In: *Phys. Rev. Lett.* 89 (1 June 2002), p. 011301. DOI: 10.1103/PhysRevLett.89.011301.

[7] B. Aharmim et al. “Electron energy spectra, fluxes, and day-night asymmetries of ^{8}B solar neutrinos from measurements with NaCl dissolved in the heavy-water detector at the Sudbury Neutrino Observatory”. In: *Phys. Rev. C* 72 (5 Nov. 2005), p. 055502. DOI: 10.1103/PhysRevC.72.055502.

[8] Y. Fukuda et al. “Evidence for Oscillation of Atmospheric Neutrinos”. In: *Phys. Rev. Lett.* 81 (8 Aug. 1998), pp. 1562–1567. DOI: 10.1103/PhysRevLett.81.1562.

[9] “The Nobel Prize in Physics 2015 - Press Release”. In: (2015). URL: http://www.nobelprize.org/nobel_prizes/physics/laureates/2015/press.html?.

[10] KATRIN Collaboration and KATRIN Collaboration. *KATRIN design report 2004*. Tech. rep. 51.54.01; LK 01. Forschungszentrum Jülich, 2005. 245 pp. DOI: 10.5445/IR/270060419.

[11] M. Aker et al. *First direct neutrino-mass measurement with sub-eV sensitivity*. 2021. arXiv: 2105.08533 [hep-ex].

[12] Gianpaolo Bellini et al. “Neutrinos from the primary proton-proton fusion process in the Sun”. In: *Nature* 512.7515 (2014), p. 383.

[13] Davide D'Angelo et al. "Recent Borexino results and prospects for the near future". In: *EPJ Web of Conferences* 126 (May 2014). DOI: 10.1051/epjconf/201612602008.

[14] W. Hampel et al. "GALLEX solar neutrino observations: results for GALLEX IV". In: *Physics Letters B* 447.1 (1999), pp. 127–133. ISSN: 0370-2693. DOI: https://doi.org/10.1016/S0370-2693(98)01579-2.

[15] Ziro Maki, Masami Nakagawa, and Shoichi Sakata. "Remarks on the Unified Model of Elementary Particles". In: *Progress of Theoretical Physics* 28.5 (Nov. 1962), pp. 870–880. ISSN: 0033-068X. DOI: 10.1143/PTP.28.870.

[16] Richard A Dunlap. "Kamiokande and Super-Kamiokande". In: *Particle Physics*. 2053-2571. Morgan & Claypool Publishers, 2018, 9-1 to 9–13. ISBN: 978-1-64327-362-4. DOI: 10.1088/2053-2571/aae6d3ch9.

[17] Andrea Giuliani and Alfredo Poves. "Neutrinoless Double-Beta Decay". In: *Advances in High Energy Physics* 2012 (Dec. 2012). DOI: 10.1155/2012/857016.

[18] University of Zurich, Website. *Neutrinoless double beta decay*. [Online; accessed August 12, 2021]. URL: https://www.physik.uzh.ch/en/groups/baudis/Research/GERDA.html.

[19] M. Agostini et al. "Final Results of GERDA on the Search for Neutrinoless Double-β Decay". In: *Phys. Rev. Lett.* 125 (25 Dec. 2020), p. 252502. DOI: 10.1103/PhysRevLett.125.252502.

[20] M. Kleesiek et al. "Beta-Decay spectrum, response function and statistical model for neutrino mass measurements with the KATRIN experiment". In: *The European Physical Journal C* 79.3 (Mar. 2019). ISSN: 1434-6052. DOI: 10.1140/epjc/s10052-019-6686-7.

[21] Ch Kraus et al. "Final results from phase II of the Mainz neutrino mass search in tritium beta decay". In: *The European Physical Journal C-Particles and Fields* 40.4 (2005), pp. 447–468.

[22] VN Aseev et al. "Upper limit on the electron antineutrino mass from the Troitsk experiment". In: *Physical Review D* 84.11 (2011), p. 112003.

[23] M. Aker et al. *The Design, Construction, and Commissioning of the KATRIN Experiment*. 2021. arXiv: 2103.04755 [physics.ins-det].

[24] Katrin Collaboration et al. "KATRIN design report 2004". In: (2005).

[25] Joseph A. Formaggio, André Luiz C. de Gouvêa, and R.G. Hamish Robertson. "Direct measurements of neutrino mass". In: *Physics Reports* 914 (June 2021), pp. 1–54. ISSN: 0370-1573. DOI: 10.1016/j.physrep.2021.02.002.

[26] JA Formaggio and J Barrett. "Resolving the reactor neutrino anomaly with the KATRIN neutrino experiment". In: *Physics Letters B* 706.1 (2011), pp. 68–71.

[27] S Grohmann et al. "The thermal behaviour of the tritium source in KATRIN". In: *Cryogenics* 55 (2013), pp. 5–11.

[28] Max Aker et al. "Quantitative Long-Term Monitoring of the Circulating Gases in the KATRIN Experiment Using Raman Spectroscopy". In: *Sensors* 20.17 (2020). ISSN: 1424-8220. DOI: 10.3390/s20174827.

[29] A. Marsteller et al. "Neutral tritium gas reduction in the KATRIN differential pumping sections". In: *Vacuum* 184 (2021), p. 109979. ISSN: 0042-207X. DOI: https://doi.org/10.1016/j.vacuum.2020.109979.

[30] Woosik Gil et al. "The Cryogenic Pumping Section of the KATRIN Experiment". In: *IEEE Transactions on Applied Superconductivity* 20.3 (2010), pp. 316–319. DOI: 10.1109/TASC.2009.2038581.

[31] Alexander Jansen. "The cryogenic pumping section of the KATRIN experiment-design studies and experiments for the commissioning". In: (2015).

[32] F. Friedel et al. "Time-dependent simulation of the flow reduction of D2 and T2 in the KATRIN experiment". In: *Vacuum* 159 (2019), pp. 161–172. ISSN: 0042-207X. DOI: https://doi.org/10.1016/j.vacuum.2018.10.002.

[33] Nancy Wandkowsky. "Study of background and transmission properties of the KATRIN spectrometers". PhD thesis. 2013. DOI: 10.5445/IR/1000036631.

[34] Karlsruhe Institute of Technology, Website. *Focal plane detector*. [Online; accessed August 15, 2021]. URL: https://www.katrin.kit.edu/84.php.

[35] J.F. Amsbaugh et al. "Focal-plane detector system for the KATRIN experiment". In: *Nuclear Instruments and Methods in Physics Research Section A: Accelerators, Spectrometers, Detectors and Associated Equipment* 778 (Apr. 2015), pp. 40–60. ISSN: 0168-9002. DOI: 10.1016/j.nima.2014.12.116.

[36] Florian M. Fränkle. "Background Investigations of the KATRIN Pre-Spectrometer". PhD thesis. 2010. DOI: 10.5445/IR/1000019392.

[37] Fabian Thomas Harms. "Characterization and minimization of background processes in the KATRIN main spectrometer". In: (2015).

[38] KATRIN Collaboration and S. Groh. *Untersuchung von UV-Laser induziertem Untergrund am KATRIN Vorspektrometer*. German. Frühjahrstagung DPG, Fachverband Teilchenphysik, Karlsruhe, 28.März - 1.April 2011 Verhandlungen der Deutschen Physikalischen Gesellschaft, R.6, B.46(2011) T 107.5. 51.54.01; LK 02. 2011.

[39] F. M. Fränkle et al. *KATRIN background due to surface radioimpurities*. 2020. arXiv: `2011.05107 [physics.ins-det]`.

[40] Nikolaus Rainer-Maria Trost. "Modeling and measurement of Rydberg-State mediated Background at the KATRIN Main Spectrometer". 51.03.01; LK 01. PhD thesis. Karlsruher Institut für Technologie (KIT), 2019. 178 pp. DOI: `10.5445/IR/1000090450`.

[41] R.G.H. Robertson. "Transverse Energy Filter". In: *KATRIN internal Report* (2019).

[42] Benedikt Bieringer. "Shifted Analyzing Plane: Field optimization for background reduction of the KATRIN experiment". Master's thesis. Westfälische Wilhelms-Universität Münster (WWU).

[43] A. Fulst et al. "Time-focusing time-of-flight, a new method to turn a MAC-E-filter into a quasi-differential spectrometer". In: *The European Physical Journal C* 80.10 (Oct. 2020). ISSN: 1434-6052. DOI: `10.1140/epjc/s10052-020-08484-9`.

[44] Nicholas Steinbrink et al. "Neutrino mass sensitivity by MAC-E-Filter based time-of-flight spectroscopy with the example of KATRIN". In: *New Journal of Physics* 15.11 (2013), p. 113020.

[45] Enrico Ellinger. "Simulation of background reduction in KATRIN via induced de-excitation of Rydberg atoms with terahertz radiation". In: DPG. Dortmund, Mar. 2021.

[46] Jordan Miles. "Detection of Chiral Organic Compounds with Femtosecond Lasers". PhD thesis. Nov. 2016. DOI: `10.13140/RG.2.2.33544.67842`.

[47] Till Cremer et al. "Recent developments on next-generation microchannel plates for particle identification applications". In: Sept. 2019, p. 21. DOI: `10.1117/12.2530037`.

[48] Richard WJ Salomon. "Development of a Setup to test Time-Of-Flight Methods for the KATRIN Experiment". Bachelor's thesis. Westfälische Wilhelms-Universität Münster (WWU).

[49] Alexander Fulst. “A Novel Quasi-Differential Method for MAC-E Filters and Determination and Control of the Electric Potentials of the KATRIN Experiment with a Stabilized Condensed Krypton Source and a UV Illumination System”. PhD thesis. Westfälische Wilhelms-Universität Münster (WWU), 2020.

[50] M Beck et al. “An angular-selective electron source for the KATRIN experiment”. In: *Journal of Instrumentation* 9.11 (2014), P11020.

[51] Michael Zacher. “High Field Electrodes Design and an Angular Selective Photoelectron Source for the KATRIN Spectrometers”. PhD thesis. Westfälische Wilhelms-Universität Münster (WWU), 2015.

[52] Jan Behrens. “Design and commissioning of a monoenergetic photoelectron source and active background reduction by magnetic pulse at the KATRIN experiment”. PhD thesis. Westfälische Wilhelms-Universität Münster (WWU), 2017.

[53] Benedikt Bieringer. *mca-recorder software*. 2020. URL: `https://zivgitlab.uni-muenster.de/b_bier05/mca-recorder`.

[54] Ferenc Glück et al. *BField_3D - Magnetic field calculation for cylincdrical coils*. 2021. URL: `https://nuserv.uni-muenster.de:8443/bbieringer/bfield_3d`.

[55] Daniel Furse et al. “Kassiopeia: a modern, extensible C++ particle tracking package”. In: *New Journal of Physics* 19.5 (May 2017), p. 053012. DOI: `10.1088/1367-2630/aa6950`.

[56] Stefan Groh. “Modeling of the response function and measurement of transmission properties of the KATRIN experiment”. PhD thesis. 2015. DOI: `10.5445/IR/1000046546`.

Danksagung

Hiermit möchte ich mich bei all jenen bedanken, die mich bei meiner Masterarbeit unterstützt haben und zum gelingen dieser auch unter den besonderen Bedingungen durch die Corona Krise beigetragen haben.
Dazu zählen im besonderen Kevin Gauda, der mit mir häufig im Labor stand und bei verschiedensten Problemen, sei es mit dem experimentellen Setup, dem theoretischen Verständnis, oder programmierschwierigkeiten gewesen, geduldig beraten hat. Irgendwie konnten wir das zugrunde liegende Problem immer feststellen und beseitigen.
Des Weiteren danke ich Volker Hannen für die professionelle Hilfeleistung im Labor, wenn es um Datenakquisition und Planung ging.
Nicht vergessen werden darf auch Alexey Lokhov, der teils bis spät in den Abend ein offenes Ohr für allerhand Fragen hatte. Darüber hinaus war die stets kompetente Hilfe von Hans-Werner Orthjohann ein ständiger Begleiter, ohne die das Projekt sicherlich längere Zeit in Anspruch genommen hätte.
Wichtig waren jedoch nicht nur die Leistungen jedes einzelnen für sich genommen, sondern auch die vielen konstruktiven Diskussiongespräche in denen die teilweise schwer interpretierbaren Ergebnisse besprochen und weitere Vorgehensweisen geplant wurden.
In dem Sinne geht ein besonderer Dank an Herrn Prof. Dr. Weinheimer für das Thema, die vielen Anregungen und die Nerven aufreibende, aber spannende und wichtige Aufgabe der winkelselektiven Elektronenmessung. Hoffentlich kann diese Arbeit ihren Teil zum erreichen des Ziels der Messung der Neutrinomasse beitragen.